UNIVERSITY OF COPENHAGEN
FACULTY OF SCIENCE

PhD Thesis

Studies on the Action Potential From a Thermodynamic Perspective

Tian Wang

Academic Advisor: Thomas Heimburg

This thesis has been submitted to the PhD School of Faculty of Science, University of Copenhagen

Niels Bohr Institute
University of Copenhagen
Denmark
April 2017

Acknowledgements

First of all, I would like to express my sincere gratitude to my advisor Prof. Thomas Heimburg for introducing me into this interesting world of biophysics and exciting topics for my PhD project, for supervision, discussions and for always encouraging me.

I would like to thank all colleagues from the Membrane Biophysics group for creating such a nice and friendly working environment, especially Dr. Rima Budvytyte for closely collaboration; Dr. Alfredo Gonzalez-Perez and Dr. Edgar Villagran Vargas for supervision at the beginning of my project; Karis Zecchi for detailed proofreading of the thesis, many useful discussions and suggestions along the way.

Thank all our collaborators on the Magnetic field measurements from the QUANTOP group in the Niels Bohr Institute (NBI) and Panum Institute, University of Copenhagen, our collaborators on fluorescence measurements from University of Southern Denmark, Lingling Zhang from Aarhus University for electrochemical measurements and Dr. Martin Jägle from Fraunhofer Institute for Physical Measurement Techniques for kindly providing us thermopiles.

Great thanks go to our electronic engineer Axel Boisen for helping with purchasing and building up the electronic setups for almost all my projects, all the discussions, ideas on different aspects of projects, and all the jokes during talks.

I would also like to extend my thanks to Chengzhe Tian and Dapeng Ding for helping me out with programming problems, Hans C. Stærkind for kindly sharing the Matlab scripts for analyzing the magnetic data.

Last but not least, I would like to thank my family for their supports and understanding; my boyfriend Min Wu for the company, helping with programming and proofreading.

Abstract

Nerve impulse, also called action potential, has mostly been considered as a pure electrical phenomenon. However, changes in dimensions, e.g. thickness and length, and in temperature along with action potentials have been observed, which indicates that the nerve is a thermodynamic system.

The work presented in this thesis focuses on the study of the following features of nerve impulses, and interpretations from a thermodynamic view are provided. (1) Two impulses propagating toward each other are found to penetrate through each other upon collision. The penetration is found in both bundles of axons and nerves with ganglia. (2) Attempts have been made to measure the temperature change associated with an action potential as well as an oscillation reaction (Briggs-Rauscher reaction) that shares the adiabatic feature. It turns out that some practical issues need to be solved for the temperature measurement of the nerve impulses, while the measured temperature change during the oscillation reaction suggests that there are a reversible adiabatic process and a dissipative process. (3) Local anesthetic effect on nerves is studied. Local anesthetic lidocaine causes a significant stimulus threshold shift of the action potential, and a slight decrease in the conduction velocity. (4) The conduction velocity of nerve impulses as a function of the diameter of the nerve is investigated with stretched ventral cords from earthworms. The velocity is found to be constant with a decrease of the diameter, indicating that the conduction velocity is independent of the diameter of the nerve. All the above results can be explained by a thermodynamic theory for nerve impulses, i.e. the Soliton theory, which considers the nerve impulses as electromechanical solitons traveling without dissipation.

Finally, the magnetic field generated by a nerve impulse is measured with a sensitive atomic magnetometer developed by our collaborators from the Quantum Optics (QUANTOP) group in our institute. The magnetometer can be operated at room or body temperatures, and magnetic field from nerve impulses can be measured several millimeters away. This provides a promising technique for medical applications.

Contents

Acknowledgements **i**

Abstract **iii**

List of Abbreviations **ix**

1 Introduction **1**
1.1 Introduction to Nerve Cells 1
1.2 Membranes 2
1.2.1 Lipids 2
1.2.2 Proteins 6
1.2.3 Structure of Biological Membranes 6
1.3 Resting Potential 7
1.4 Action Potential 8
1.5 Scope and Outline 9

2 Nerve Models **11**
2.1 Hodgkin-Huxley Model (HH Model) 11
2.1.1 Equivalent Circuit of Nerve Membranes 11
2.1.2 Membrane Current 12
2.1.3 Propagating Action Potentials 13
2.1.4 Shaping of Action Potentials by Ion Channels 15
2.1.5 Noble's Model for Nerve Excitation 17
2.2 Thermodynamic View of HH Model 19
2.2.1 Mechanical Changes 19
2.2.2 Optical Changes 20
2.2.3 Heat Changes 20
2.2.4 Lipid Channels 23
2.3 Soliton Model 23
2.3.1 Elastic Constants 25
2.3.2 Solitons in Nerves 27
2.3.3 Nerve Impulses in Soliton Model 29
2.3.4 Anesthesia in Soliton model 31

3 Materials and Methods **33**
3.1 Materials 33
3.2 Sample Preparation 34
3.2.1 Nerve Samples 34
3.2.2 Lipid Samples 36
3.3 Methods 36
3.3.1 Electrophysiology 36
3.3.2 Differential Scanning Calorimetry (DSC) 37
3.3.3 Thermocouple and Thermopiles 38
3.3.4 Voltammetry 40

4 Collision of Action Potentials **43**
4.1 Background 43
4.2 Abdominal Ventral Cord of Lobsters in Liquid Chamber 46
4.2.1 Liquid Chamber 46
4.2.2 Results and Discussions 47
4.3 Axon Bundle From Lobster Walking Legs 48
4.4 Perturbation Tests on Nerves 51
4.5 Summary 54

5 Heat Change During Adiabatic Processes **57**
5.1 Background 57
5.1.1 Theory 58
5.2 Temperature Change of Nerve Impulses 61
5.2.1 Experimental 61
5.2.2 Results and Discussions 62
5.3 Temperature Change of Briggs-Rauscher Reaction 64
5.3.1 Experimental 64
5.3.2 Results and Discussions 66
5.4 Summary 69

6 Anesthetic Effect **71**
6.1 Background 71
6.2 Materials and Methods 72
6.2.1 Nerves 72
6.2.2 Chamber 73
6.2.3 Lidocaine 74
6.3 Results and Discussions 75
6.3.1 Results 75
6.3.2 Discussions 78
6.4 Summary 80

7 Effect of Stretching **83**
7.1 Background . . . 83
7.2 Materials and Methods . . . 85
7.3 Results and Discussions . . . 86
7.4 Summary . . . 88

8 Magnetic Field of Nerve Impulses **91**
8.1 Backgroud . . . 91
8.2 Materials and Methods . . . 93
8.2.1 Magnetometer . . . 93
8.2.2 Principles of Measurements . . . 95
8.2.3 Nerve and Electrical Measurement . . . 97
8.2.4 Operation of Magnetometer . . . 99
8.3 Results and Discussions . . . 100
8.3.1 Electrical Recording . . . 100
8.3.2 Pulsed Mode . . . 101
8.3.3 Continuous Mode . . . 103
8.4 Summary . . . 104

9 Conclusions and Outlook **107**
9.1 Conclusions . . . 107
9.2 Outlook . . . 108

Bibliography **111**

Appendices **121**
A Heat Capacity and Compressibility . . . 121
B Dispersion in Soliton Model . . . 122
C Temperature Measurement . . . 123
D Bidirectional Propagation . . . 124

List of Abbreviations

List of Abbreviation

ANS	8-anilinonaphthalene-1-sulfonic acid
AP	action potential
BR	Briggs-Rauscher (reaction)
CAP	compound action potential
DAQ	data acquisition
DLPC	1,2-dilauroyl-*sn*-glycero-3-phosphocholine
DMPC	1,2-dimyristoyl-*sn*-glycero-3-phosphocholine
DPPC	dipalmitoylphosphatidylcholine
DSC	differential scanning calorimetry
EDTA	(ethylenedinitrilo)tetraacetic acid
ED_{50}	effective dose
EP_{50}	effective pressure
HEPES	4-(2-hydroxyethyl)piperazine-1-ethanesulfonic acid
HH	Hodgkin-Huxley
LUVs	large unilamellar vesicles
MLVs	multilamellar vesicles
NBI	Niels Bohr Institute
PC	phosphocholine
PVDF	polyvinylidene fluoride
QUANTOP	Quantum Optics group
SQUID	Superconducting Quantum Interference Device

Chapter 1

Introduction

1.1 Introduction to Nerve Cells

A nerve cell, also called neuron, is the basic unit of the nervous system and one of the basic components in the brain. Neurons have various shapes and sizes. Typically a neuron consists of a cell body (soma), dendrites, an axon, and axon terminals, as schematically shown in Fig. 1.1.

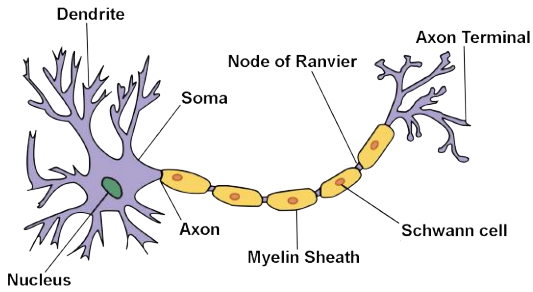

Figure 1.1: Schematic illustration of a typical neuron, figure adapted from Wikipedia.

Soma is the metabolic center of the neuron which is essential for any neurons. It consists of nucleus containing genes of the cell and organelles, e.g. Nissl granules (composed of rough endoplasmic reticulum), mitochondria and free polyribosomes providing sites for protein synthesis etc. Dendrites branch off the soma forming a tree-like shape and receive the electrochemical stimulation from other nerve cells. The cell bodies of neurons in the peripheral nervous system are clustered in masses, which are called ganglia.

Axons arise from the soma and extend from less than a millimeter up to more than two meters long. The electrical nerve signal, which is called action potential (also called "nerve impulse"or "spike"), is usually initiated at the initial segment near the origin of the axon from soma and propagates down the axon without distortion at a speed of up to 120 m/s. At the distal end of the axon, it divides into branches (axon terminals) that contact other neurons and transmit impulses

to the next neuron. The transmission is through a small gap forming synapse together with the two nerve terminals [1, 2, 3].

In large groups of vertebrate nerve cells, a layer of myelin surrounds the axon. Such nerves are therefore called myelinated nerves. The myelin sheath is mainly made of lipids forming an electrically insulating layer around the axon. The myelin sheath is interrupted at regular intervals by gaps called Nodes of Ranvier, which are short unmyelinated segments. The action potential jumps from node to node [4, 5], moving significantly faster than in unmyelinated neurons. The axons in myelinated neurons are known as nerve fibers.

The inside of neurons is, like other cells, separated from the environment by plasma membrane. The cell membrane of neurons is believed to play a key role for nerve impulse generation and propagation. It is crucial to understand the structure and function of membranes in order to understand how nerves function.

1.2 Membranes

Membranes are not only important components of neurons, but also of all kinds of cells. Cells are surrounded by plasma membranes, and many organelles in cells, such as nucleus, mitochondria, endoplasmatic reticulum, Golgi-complex, lysosomes, peroxisomes and chloroplasts, are all surrounded by membranes. Biological membranes consist mainly of lipids and proteins.

1.2.1 Lipids

Lipid Structure

Lipids are small amphiphilic molecules with a hydrophilic head group and hydrophobic hydrocarbon chains. There exists a large variety of different lipids, e.g. phospholipids, fatty acids, cholesterol etc. The hydrocarbon chains can vary in number of chains, chain length and degree of chain saturation. The head groups can vary in charge, polarity, and size. The structures of some lipid molecules are shown in Fig. 1.2.

Due to their amphiphilic nature, when exposed to water lipid molecules tend to self-assemble orienting the hydrophilic head groups towards water and the hydrocarbon chains away from it. As a consequence, they display a variety of phases with different geometry depending on the chemical structure, temperature, pressure, water content etc. Several phases of lipid-water system are shown in Fig. 1.3. The driving force of forming different structures is the optimization of the hydrophobic effect with intra- and intermolecular interactions, in combination with geometric packing constraints [6].

The most widely used nomenclature for lyotropic phases was proposed by Luzzati [8]. The lattice type is denoted by a capital letter, e.g. L for lammellar,

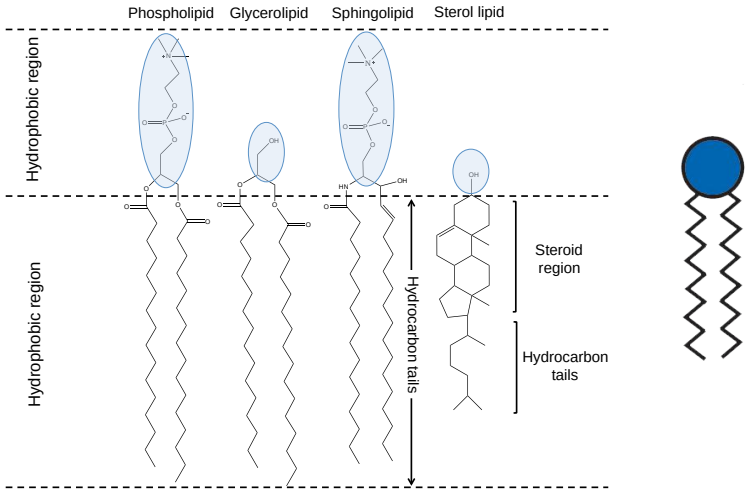

Figure 1.2: Chemical structure of several lipid species. The names at the top are the names of lipid species instead of specific lipid. The cartoon on the right is generally used to illustrate a lipid molecule with a hydrophilic head and a hydrophobic tail. The chemical structures of lipid molecules are generated with ChemDraw Professional.

P for two-dimensional oblique, H for hexagonal and Q for cubic. Subscripts I and II are used to denote normal (oil in water) or reversed (water in oil) topology phases. A greek subscript is used to denote the chain conformation, e.g. c for crystalline, β for ordered gel-like, α for liquid-like (disordered).

In cell membranes, the majority of lipids are phospholipids. They have a hydrophilic head group and two hydrophobic hydrocarbon chains that can have various conformations generated by the rotation around the C-C bonds. Phospholipids mainly form a bilayer structure in cell membranes. The arrangement of the head group and the conformation of the hydrocarbon chains may vary upon changes in thermodynamic variables, resulting in different phases of the lipid bilayer. One generally finds four phases of bilayer membranes [9]:

• L_c: crystalline phase. The lipids are ordered in three dimensions (Fig. 1.3 A);

• $L_{\beta'}$: solid-ordered phase, also called "gel phase". The lipids are arranged on a triangular lattice [10]. Hydrocarbon chains are mostly in "all-trans" conformation, ordered and tilted (Fig. 1.3 D);

• $P_{\beta'}$: the "ripple" phase. The membrane is partially solid and partially fluid organized with periodic one-dimensional ripples on the membrane surface. (Fig. 1.3 E);

• L_α: the liquid-disordered phase, usually called the "fluid phase". The lattice order of lipids is lost, the hydrocarbon chains are disordered with trans-, gauche$^-$ and gauche$^+$ conformations (Fig. 1.3 F).

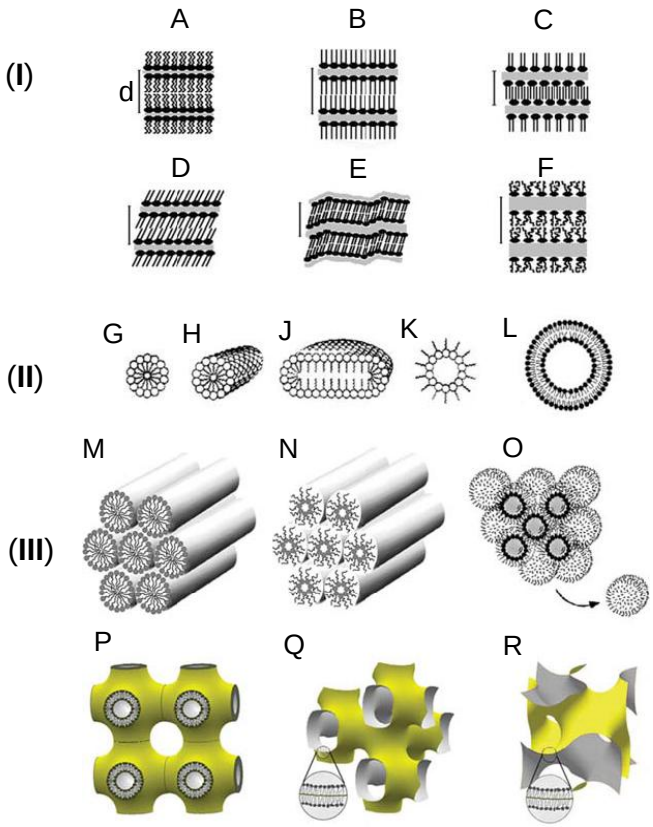

Figure 1.3: Structures of lipid phases. I. Lamellar phases: (A) subgel, L_c; (B) gel, L_β; (C) interdigitated gel, $L_\beta{}^{int}$; (D) gel, tilted chains, $L_\beta{}'$; (E) rippled gel, $P_\beta{}'$; (F) liquid crystalline, L_α. II. Micellar aggregates; (G) spherical micelles, M_I; (H) cylindrical micelles (tubules); (J) disks; (K) inverted micelles, M_{II}; (L) liposome, III. Non-lamellar liquid-crystalline phases of various topology; (M) hexagonal phase H_I; (N) inverted hexagonal phase H_{II}; (O) inverted micellar cubic phase $Q_{II}{}^M$; (P) bilayer cubic (Q_{II}) phase Im3m; (Q) bilayer cubic phase Pn3m; (R) bilayer cubic phase Ia3d. Figure taken from [7].

Lipid Melting

When external thermodynamic variables are changed, e.g. when the temperature is increased, lipid bilayers may go through a transition from one phase to another. For phospholipids, the main transition is between the gel phase and the fluid phase as illustrated in Fig. 1.4. In the phase transition region, the addition of heat does not change the temperature of the membranes, instead the energy is used to induce the conformational changes. Therefore, if one plots the heat capacity profile as a function of temperature, it will display a peak in the phase transition region. The heat capacity profile can be obtained from calorimetry measurements. Fig. 1.5 shows the heat capacity profile of 1,2-dimyristoyl-*sn*-glycero-3-phosphocholine (DMPC) multilamellar vesicles measured with a differential scanning calorimeter (DSC). The predominant peak at around 23.9 ℃ is

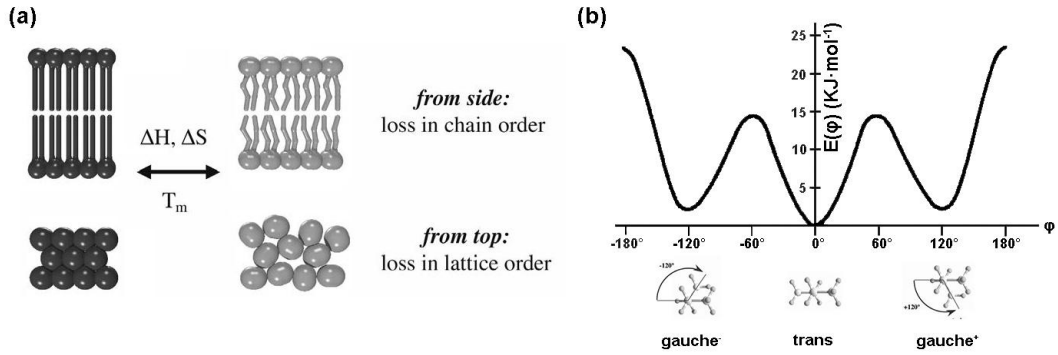

Figure 1.4: (a) Schematic illustration of lipid melting from a solid-ordered to a liquid-disordered phase. Top: The order within the lipid chains is lost upon melting. Bottom: The crystalline order of the lipid head groups is lost and the matrix undergoes a solid-liquid transition. (b) Conformation of lipid chains. There are three energy minima at -120°, 0°, 120° respectively. The state with lowest energy is at 0°, with the lipid hydrocarbon chains at a all-trans conformation. Figures adapted from [9].

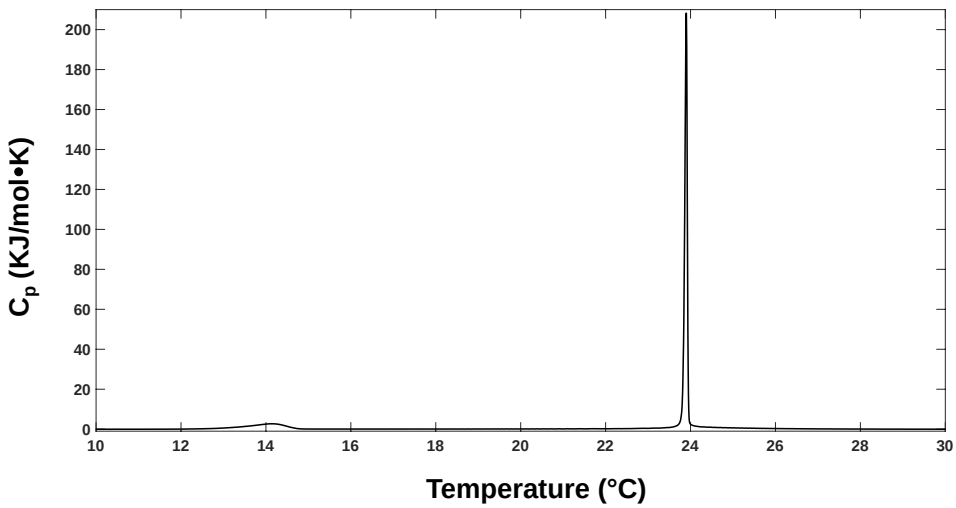

Figure 1.5: Heat capacity profile of 1,2-dimyristoyl-*sn*-glycero-3-phosphocholine (DMPC) multilamellar vesicle solution measured with DSC (upscan). The concentration of DMPC is 10 mM. The composition of buffer solution is: 150 mM KCl, 1 mM EDTA, 1 mM HEPES, pH adjusted to $\sim$ 7.4. Measured in the lab of Membrane Biophysics group, Niels Bohr Institute.

the main transition. The smaller peak around 10 ℃ is the pretransition from the gel phase to the ripple phase [11], which happens in some species of phospholipid bilayers. The work in this thesis considers mainly the main transition of lipid membranes between the gel phase and the fluid phase. The phase transition from the gel phase to the fluid phase is also usually called lipid melting. The melting temperature (T_m) is defined as the temperature at which half of the lipids are in the fluid phase and the other half is in the gel phase. At this temperature, the

free energy difference between the two states, ΔG is zero,

$$\Delta G = G_f - G_g = 0 \tag{1.1}$$

$$\Delta G = \Delta H - T_m \Delta S = 0 \tag{1.2}$$

where ΔH is the melting enthalpy and ΔS is the melting entropy, G_f is the free energy in the fluid phase, and G_g is the free energy in the gel phase. Thus the melting temperature T_m is defined as:

$$T_m = \frac{\Delta H}{\Delta S} \tag{1.3}$$

It corresponds to the peak temperature of the transition in the heat capacity profile. Membrane phase transitions are influenced by various thermodynamic variables, e.g. pressure [12], pH [13], calcium concentration [14], and small drugs such as anesthetics [15].

Phosphatidylcholines (PC) are a group of phospholipids composed of a choline head group, a glycerophosphoric acid backbone and a variety of hydrocarbon chains. They are major components of biological membranes. A neutral, saturated (hydrocarbon chains) phosphatidylcholine Dipalmitoylphosphatidylcholine (DPPC) unilamellar vesicles are used as model system for biological membranes in the thesis.

1.2.2 Proteins

Another important membrane component is protein. Proteins are biomacromolucules with three-dimensional arrangement of atoms. They generally fold into one or more structural conformations driven by non-covalent interactions, e.g. hydrogen bonding, hydrophobic effect, electrostatic interactions and Van der Waals forces.

Proteins are carriers of function in life, e.g. enzymes that catalyze biochemical reactions, important components of structural building blocks which may have mechanical functions, antibodies that are involved in immune protection, ion pumps that are responsible for active transport of ions across membranes, ion channels that are responsible for passive transport of ions across membranes etc. Among a wide range of proteins, ion channel proteins are generally believed to play a key role in ion movements across the membrane during a nerve impulse and in shaping the action potential.

1.2.3 Structure of Biological Membranes

A famous model for membrane structure is the “fluid mosaic model” proposed by Singer and Nicolson [16]. According to the model, phospholipids form a discontinuous fluid bilayer matrix. Proteins can be either held to the membrane by weak

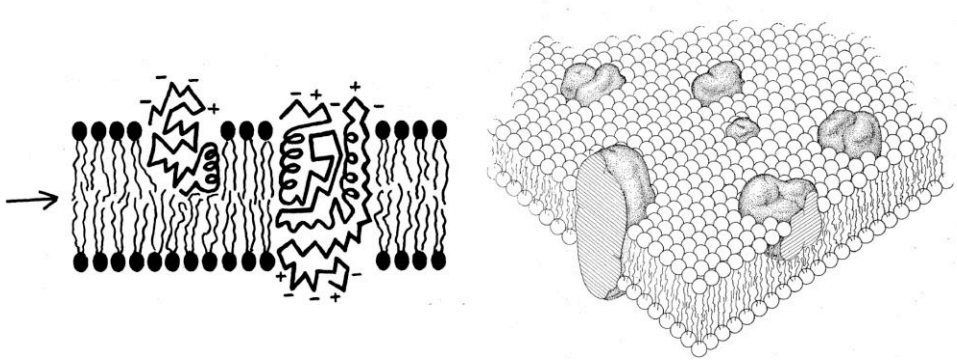

Figure 1.6: Fluid-mosaic model of membrane structure. Left: lipids form a fluid bilayer matrix, with proteins attached or penetrated. The hydrophobic part of the protein structure inserts into the area of hydrophobic hydrocarbon chains, with the charged part facing water. Right: 3D structure of a biological membranes. Figures adapted from [16].

non-covalent interactions and thus not strongly associated with lipids (peripheral proteins), or embedded in/span the lipid bilayer with strong interactions and cannot be dissociated easily (integral proteins). Integral proteins are important components for membrane integrity. They are heterogeneous globular molecules with ionic and highly polar groups exposed to the aqueous environment, and the non-polar groups buried in the hydrophobic interior of the membrane. The entire membrane is a dynamic system constantly in flux.

Refinements have been proposed to the fluid mosaic model considering inhomogeneous distribution of lipids and proteins and domain formation in the membrane [17]. Nevertheless, the fluid mosaic model is still widely accepted.

1.3 Resting Potential

The cytoplasmic and extracellular mediums are both fluids containing various solutes including ions. Ions are not uniformly distributed across the membrane. Large gradients of ions across the membrane are established, e.g. the concentration of K^+ is higher in the cytoplasmic, while the concentration of Na^+ is higher in the extracellular solution. An example of ion concentrations inside and outside of the plasma membrane of a squid axon is shown in Table. 1.1.

The membrane is selectively permeable to ions, meaning that it is more permeable to some ion species, and less permeable to other ions. For simplicity, we first assume that the membrane is only permeable to K^+, but not to other ions. The concentration gradient drives the diffusion of K^+ outwardly along the gradient. Since other ions cannot pass through the membrane, it results in a charge imbalance on the two sides of the membrane. As a consequence, an electric field is generated in the opposite direction of the K^+ diffusion. This in turn drives the movement of K^+ in the resulting electric field, which has an inward direction.

	Inside $[C_{in}]$ (mM)	Outside $[C_{out}]$ (mM)	Equilibrium Potential $E_i = \frac{RT}{zF} ln \frac{[C_{out}]}{[C_{in}]}$
K^+	400	20	$25.2 \ln \frac{20}{400} = -75mV$
Na^+	50	440	$25.2 \ln \frac{440}{50} = 55mV$
Cl^-	40–150	560	$-25.2 \ln \frac{560}{40} = -66mV$
Ca^{2+}	0.4	10	$12.6 \ln \frac{10}{10^{-4}} = 145mV$

Table 1.1: Ion concentrations inside and outside of a squid axon and the calculated Nernst potential for each ion. The table is adapted from [18].

After some time, the rate of diffusion and that of the movement in the electrical field become equal, and thus it reaches an equilibrium with no net flux. A difference of electrical potential, or voltage, across the membrane is generated, which is called the membrane potential (V_m). The equilibrium potential of ion i is defined as E_i. The membrane potential in this case is equal to the equilibrium potential of K^+, which can be described by Nernst equation (by taking the potential of the outside medium as a reference):

$$V_m = E_K = -\frac{RT}{zF} \ln \frac{[C_{in}]}{[C_{out}]} \tag{1.4}$$

where R is the gas constant, z is the charge of the ion, F is the Faraday constant, $[C_{in}]$ and $[C_{out}]$ are the concentrations of K^+ inside and outside the cell.

The actual biological membranes are of course not only permeable to K^+, but also to other ions like Na^+, Cl^-. However, the permeability of different ions may vary. If P_i represents the membrane permeability for each individual ion species (cm/s), the membrane resting potential is then given by the Goldman-Hodgkin-Katz voltage equation [19, 20]:

$$V_{rest} = \frac{RT}{F} \ln \left(\frac{P_K[K^+]_{out} + P_{Na}[Na^+]_{out} + P_{Cl}[Cl^-]_{in}}{P_K[K^+]_{in} + P_{Na}[Na^+]_{in} + P_{Cl}[Cl^-]_{out}} \right) \tag{1.5}$$

This equation implies that the ion species that has a larger concentration and membrane permeability would contribute more in determining the membrane potential. In most neurons, the resting potential has a value of approximately -70 mV.

1.4 Action Potential

Upon appropriate stimulus, the membrane of excitable cells, like neurons, will display a transient (milliseconds) change in the membrane potential, which is called action potential, also known as 'nerve impulse' or 'spike'. A typical action potential trace is schematically shown in Fig. 1.7. The membrane at rest has a potential of -70 mV with the potential of the extracellular medium as zero, which

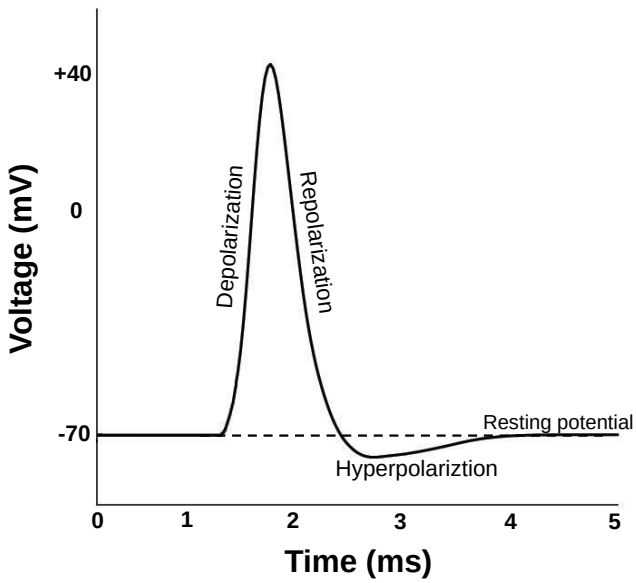

Figure 1.7: Schematic of an typical action potential. The membrane potential at rest is -70 mV, which is first reversed and then restored with an overshoot.

is a polarized state. During an action potential, the membrane potential is first increased and reversed to a positive value, which is the so-called depolarization process. It subsequently goes back to the resting state, with a possible undershoot in some neurons. This process is called repolarization. The undershoot is called hyperpolarization, which makes the nerve membrane more negative than the resting potential.

The action potential propagates along neurons, which is responsible for information carrying and transmission in the nervous system and in the brain. Thus it is meaningful to understand the principles and physical mechanisms underlying the excitation and propagation of action potentials.

1.5 Scope and Outline

Different theories and models have been proposed to describe nerve impulses. The most famous and widely accepted one is the Hodgkin-Huxley model (HH model) based on an equivalent circuit consisting of a membrane capacitor with constant capacitance and individual resistors in parallel. Upon stimulus, the resistors can change their conductances, allowing for the passage of ions. The shape of an action potential is related to the currents due to the movement of ions across the membrane. The HH model is later challenged by some researchers based on experimental findings that contradict the model. In 2005, Heimburg and Jackson proposed that nerve impulses are electromechanical pulses like solitons, which treats the action potential from a thermodynamic viewpoint. This model will be

called the Soliton model hereafter. In the context of Soliton model, the nerve membrane goes through a phase transition during an impulse, which gives the possibility for generation of a solitary density wave that propagates at a constant velocity longitudinally without distortion in its shape. The aim of the thesis is to further understand the nerve impulse from a thermodynamic view.

In Chapter 2, the HH model and the Soliton model will be introduced in a detailed manner, including the assumptions, mathematical descriptions, and intuitive explanations of the nerve impulse.

In Chapter 3, the main materials and methods are described.

The work presented in chapters 4-7 is based on several discrepancies between the HH model and the Soliton model. Experiments are designed with the aim of getting a better insight of related issues, more specifically:

In Chapter 4, the collision of two nerve impulses traveling in opposite directions are studied. According to HH model, collision leads to mutual annihilation of the two impulses; while in Soliton model, impulses can penetrate each other and continue propagating.

In Chapter 5, attempts are made to measure the temperature change during an action potential and an oscillation reaction. HH model describes a dissipating process due to currents flowing through resistors; while in the Soliton model, the nerve impulse is an adiabatic process with no net heat change, which shares the same reversible adiabatic property with oscillation reactions.

In Chapter 6, effects of local anesthetic lidocaine on invertebrate nerves are studied. HH model predicts a shift of stimulation threshold up to ~ 2.5 folds, and a significant drop in the peak amplitude; while Soliton model predicts a wider range of threshold shift upon exposure to anesthetics and no significant change in the peak amplitude.

In Chapter 7, the effect of axon diameter on the conduction velocity is studied with the nerve stretched. In accordance with the HH model, the conduction velocity is proportional to the square root of the diameter of the nerve; while in Soliton model, the initiation and propagation of action potentials depend on the composition of the axon and the properties of local medium, independent of the nerve size.

The last chapter (Chapter 8) deals with another thermodynamic property of a nerve impulse, magnetic field. The magnetic field generated by a propagating nerve impulse was measured with a sensitive atomic magnetometer constructed by our collaborator from the QUANTOP group in NBI.

Chapter 2

Nerve Models

2.1 Hodgkin-Huxley Model (HH Model)[1]

2.1.1 Equivalent Circuit of Nerve Membranes

Based on a series of studies on the membrane potential and current relations, Alan Lloyd Hodgkin and Andrew Huxley proposed a model for action potential generation and propagation in 1952. It will, together with the developments after the original model, be referred to as the Hodgkin-Huxley model (HH model) hereafter. Several basic observations from their experiments are summarized as follows:

• Upon changes of the membrane potential, the membrane permeability for different ion species could change.

• Different phases of the action potential are related to the movements of different ion species across the membrane. Depolarization is associated with the movement of sodium ions from the outside to the inside of the membrane; and repolarization is associated to the movement of potassium ions from the inside to the outside.

• When the membrane potential undergoes a sudden change and is held at a constant value, a current across the membrane can be detected which consists of an instantaneous capacitive current and time-dependent ionic currents due to the movement of ions.

They suggested that the electrical behavior of the membrane can be described by an equivalent circuit like the one shown in Fig. 2.1. It is composed of a membrane capacitor and several resistors that allow ions to selectively go across the membrane in parallel. Currents can be carried 'through' the membrane by charging the membrane capacitor and by the movement of ions through the resistors. The permeability to ions is represented by a coefficient with the dimension of conductance (g_i), which will be referred to as conductance hereafter. The ionic current consists of a sodium current (I_{Na}), a potassium current (I_K) and a leak

[1]Section 2.1.1, 2.1.2, 2.1.3 are a summary of a series of references [21, 22, 23, 24, 25].

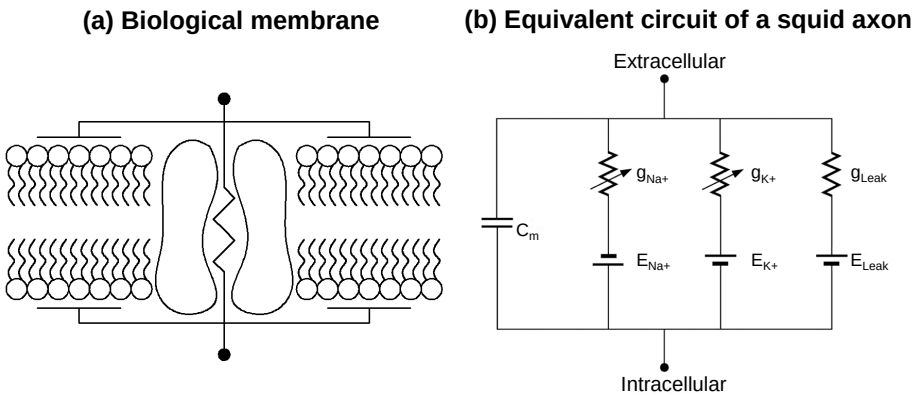

Figure 2.1: (a) Schematic drawing of nerve membrane consisting of lipid membrane and an example of ion channel proteins. (b) Equivalent circuit of a squid axon proposed by Hodgkin&Huxley. Figure adapted from [25].

current of chloride and other ions (I_L),

$$I_i = g_i(V - E_i) \tag{2.1}$$

where I_i is the current for each ion species, V is the voltage applied across the membrane, E_i is the resting potential for each ion species. Since each individual resistor and the membrane capacitor are in parallel, the overall current is

$$I = g_{Na}(V - E_{Na}) + g_K(V - E_K) + g_L(V - E_L) + C_m \frac{dV}{dt} \tag{2.2}$$

The permeability coefficients (conductance) g_i for Na^+ and K^+ are functions of time and the membrane potential, while E_{Na}, E_K, E_L, C_m (the membrane capacitance per unit area) and g_L are taken as constant. Thus the conductance of potassium and sodium can be expressed by the conductances at rest ($g_{K,0}, g_{Na,0}$) and a function of voltage and time ($Y_K(V,t), Y_{Na}(V,t)$):

$$g_K(V,t) = g_{K,0} \cdot Y_K(V,t) \qquad g_{Na}(V,t) = g_{Na,0} \cdot Y_{Na}(V,t) \tag{2.3}$$

The depolarization results in a transient increase in the sodium conductance, but a slower increase in the potassium conductance. This can be reversed upon repolarizing the membrane.

2.1.2 Membrane Current

Hodgkin and Huxley assumed that the ion movements are gated by charged particles that allow sodium and potassium ions to pass through the membrane separately. The particles can be found either on the outside or the inside of the membrane, with a negligible low concentration elsewhere. Assumption for potassium ions is that they can only pass through the membrane when four gating particles are found on a certain site of the membrane, with n being the fraction

of the gating particles found on this side. Thus $(1-n)$ represents the fraction of gating particles on the other side. α_n and β_n describes the first order kinetics of the transfer of the gating particles in two opposite directions. The potassium conductance is then controlled in the following manner

$$g_K = g_{K,0} \cdot n^4, \quad n = n(V,t) \tag{2.4}$$

$$\frac{dn}{dt} = \alpha_n(1-n) - \beta_n n \tag{2.5}$$

where $g_{K,0}$ (S/cm^2) is a constant, α_n and β_n (s^{-1}) are rate constants which vary with voltage, but not with time, n is a dimensionless variable which can vary between 0 and 1.

Similar description can be applied to sodium conductance. The assumptions are that sodium conductance is proportional to the number of sites on the inside of the membrane which are occupied simultaneously by three activating particles but are blocked by an inactivating molecule, and that it is determined by two variables which obey the first order kinetics. m represents the fraction of activating molecules on the inside and $(1-m)$ the fraction on the outside. h is the fraction of inactivating molecules on the outside and $(1-h)$ the proportion on the inside. α_m or β_h and β_m or α_h represent the transfer rate constants in the two directions.

$$g_{Na} = m^3 h g_{Na,0}, \qquad m = m(V,t), \;\; h = h(V,t) \tag{2.6}$$

$$\frac{dm}{dt} = \alpha_m(1-m) - \beta_m m, \qquad \frac{dh}{dt} = \alpha_h(1-h) - \beta_h h \tag{2.7}$$

where $g_{Na,0}$ (S/cm^2) is a constant, α_m, β_m, α_h, β_h are rate constants which vary with voltage, but not with time.

The parameters α_n, β_n, α_m, β_m, α_h and β_h were determined by fitting from experimental data. Details can be found in [21] and will not be described here. The total membrane current can then be expressed as

$$\begin{aligned} I_m = I_c + I_i &= C_m \frac{dV}{dt} + g_{Na}(V - E_{Na}) + g_K(V - E_K) + g_L(V - E_L) \\ &= C_m \frac{dV}{dt} + g_{Na,0} \cdot m^3 h(V - E_{Na}) + g_{K,0} \cdot n^4 (V - E_K) + g_L(V - E_L) \end{aligned} \tag{2.8}$$

2.1.3 Propagating Action Potentials

Consider an axon as a cylinder with homogeneous properties, but inhomogeneous potential as shown in Fig. 2.2. Several electrical properties are given below: the radius of the cylinder a, the specific resistance across the membrane $R_m(\Omega \cdot cm^2)$, the specific resistance along the membrane $R_i(\Omega \cdot cm)$, specific capacitance $C_m(F/cm^2)$. The cable-specific parameters are then given as: $r_m = R_m/2\pi a(\Omega \cdot cm)$, $r_i = R_i/\pi a^2(\Omega/cm)$, $c_m = C_m \cdot 2\pi a(F/cm)$, r_0 is the specific resistance

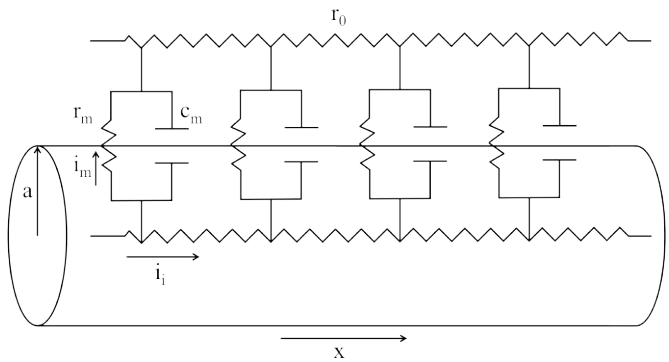

Figure 2.2: Circuit diagram of current in a uniform cylinder e.g. an axon or segment of dendrite. Figure adapted from [18].

outside the axon. If a constant current I_0 is injected at position $x = 0$, the voltage across the membrane is dependent on the distance of the membrane segment from this point and time, $V = V(x, t)$. The decay of voltage along the cylinder is

$$\frac{\partial V}{\partial x} = -r_i \cdot i_i \tag{2.9}$$

At each position of the nerve, a change of the current along the nerve must be compensated by a current across the membrane (Kirchhoff's law):

$$\frac{\partial i_i}{\partial x} = -i_m \tag{2.10}$$

Combining Eq. 2.9 and Eq. 2.10

$$\frac{\partial^2 V}{\partial x^2} = -r_i \frac{\partial i_i}{\partial x} = r_i \cdot i_m \tag{2.11}$$

thus,

$$i_m = \frac{1}{r_i}\frac{\partial^2 V}{\partial x^2} \Rightarrow \quad I_m = \frac{a}{2R_i}\frac{\partial^2 V}{\partial x^2} \tag{2.12}$$

Combining with Eq. 2.8

$$\frac{a}{2R_i}\frac{\partial^2 V}{\partial x^2} = C_m \frac{\partial V}{\partial t} + g_{Na}(V - E_{Na}) + g_K(V - E_K) + g_L(V - E_L) \tag{2.13}$$

If one assumes that the action potential propagates, during steady propagation, it follows the wave equation

$$\frac{\partial^2 V}{\partial x^2} = \frac{1}{\theta^2}\frac{\partial^2 V}{\partial t^2} \tag{2.14}$$

where θ is the velocity of conduction. Thus,

$$\frac{a}{2R_i\theta^2}\frac{\partial^2 V}{\partial t^2} = C_m \frac{\partial V}{\partial t} + g_{Na}(V - E_{Na}) + g_K(V - E_K) + g_L(V - E_L) \tag{2.15}$$

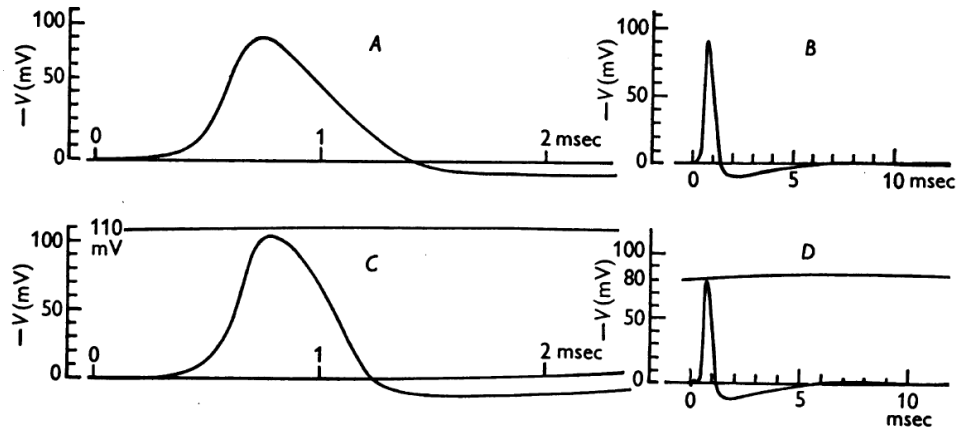

Figure 2.3: A comparison between the calculated and the measured action potential. (A) solution of Eq. 2.15; (B) same solution as in A but plotted on a slower time scale; (C) measured propagated action potential with the same scales as A; (D) measured propagated action potential from another axon with similar scales as B. Figure taken from [21].

Inserting the gating variables terms for g_{Na} and g_K into Eq. 2.15, the final equation for propagating action potential is

$$\frac{a}{2R_i\theta^2}\frac{\partial^2 V}{\partial t^2} = C_m\frac{\partial V}{\partial t} + g_{Na,0}\cdot m^3 h(V-E_{Na}) + g_{K,0}\cdot n^4(V-E_K) + g_L(V-E_L) \quad (2.16)$$

This differential equation can be solved numerically. One finds a good fit between the numerical solution of HH equation and the measured action potential on squid giant axon, as shown in Fig. 2.3. Whereas, the model involves quite many parameters that need to be obtained by fitting from experimental data, such that it has a weak prediction power before experimental data are available.

2.1.4 Shaping of Action Potentials by Ion Channels

The gating particles are later found to be a class of proteins that change their conformations upon stimuli, allowing specific ions to go across the membrane [26]. They are called ion channel proteins. The sodium and potassium ion channel proteins are voltage gated. When the membrane potential near the channels changes, channel proteins can change their conformation from a "closed" state to an "open" state, allowing the passage of ions. By this means, ion channels shape action potentials as schematically shown in Fig. 2.4 for a human nerve cell.

Intuitively, the resting potential of the nerve membrane is -70 mV. There is a threshold value of stimulus above which an action potential can be initiated. Initiations are failed when the stimulus is less than the threshold value. When it reaches the threshold, the sodium channels will open. Sodium ions then travel from the outside to the inside of the nerve membrane, resulting in a reverse of membrane polarity so that the inside of the membrane is more positive than the

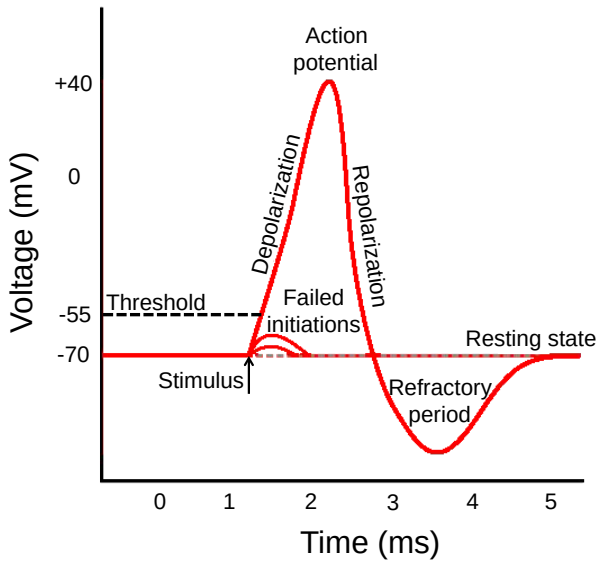

Figure 2.4: Typical action potential from a human nerve cell with schematic illustration of the shaping of channel proteins. The drawing is adapted from Wikimedia Commons.

outside (Depolarization). The sodium channels are subsequently closed and the potassium channels will be open as it is much slower for them to open. Potassium ions then travel from the insideto the outside of the membrane, restoring the membrane potential to a negative resting value (Repolarization). The repolarization sometimes overshoots the resting potential (Hyperpolarization). Hyperpolarization prevents the nerve from responding to a new stimulus during this time, or at least raises the threshold. The period in which the nerve becomes inexcitable after an action potential is called refractory period. After hyperpolariztion, the ion pumps will bring the ions back to the resting state, bringing the nerve membrane back to its resting potential.

Once an action potential is initiated, it will propagate along the axon. The propagation process is schematically shown in Fig. 2.5. When the sodium channels open at the initiation section, sodium ions move from the outside to the inside of the membrane, which depolarizes the membrane. Inside the axon, there will be longitudinal flow of sodium ions from the depolarized region to the adjacent sections by local current flow. For the proximal part of the axon , sodium channels are closed and potassium channels open, resulting in the depolarization of the membrane followed by the refractory period. Therefore, the proximal part is prevented from another depolarization. For the distal part, local current flow from the active region causes new sections of the membrane to be depolarized. In this way, the action potential propagates down the axon.

In myelinated nerves, the myelin layer insulates the axon in a discontinuous way. It is believed that the density of sodium channels are higher at the Nodes of Ranvier where the insulation is interrupted, so that the current jumps from one node to another. This results in a much higher conduction velocity than in

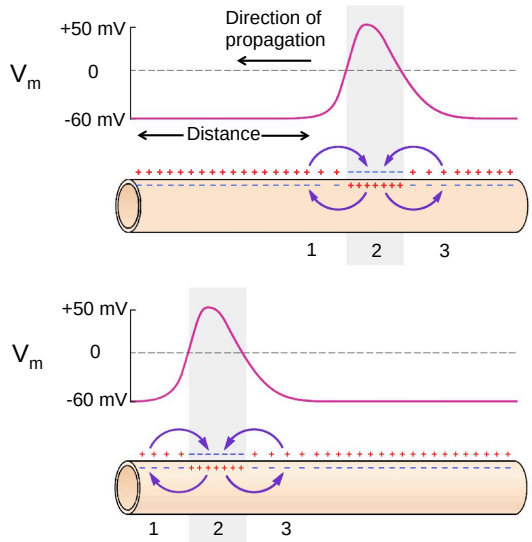

Figure 2.5: Schematic illustration showing how a depolarization wave propagates down the axon after initiation. Upper: an action potential propagating from the right to the left creating a local change in the membrane potential, which drives a local current with directions of the arrows. Lower: After some time, the action potential arrives at a new spot of the axon as it propagates. Figure taken from [3].

unmyelinated nerves. A typical conduction velocity in unmyelinated nerves is below 10 m/s, while in myelinated nerves, it can reach even over 100 m/s.

2.1.5 Noble's Model for Nerve Excitation

A simplification of HH model for nerve excitation is the Noble's model [27], which illustrates the characteristics of nerve excitation without going too much into mathematical details. It is based on the following assumptions:
1) m particle moves significantly faster than n and h, so that it will reach the value at steady-state almost instantaneously.
2) The instantaneous $I - V$ curve for K^+ is linear, which is true in squid axon. The instantaneous $I - V$ curve for Na^+ is voltage dependent.
The membrane current is a sum of sodium current and potassium current, $I_i = I_{Na} + I_K$. The $I - V$ relation of excitable membranes is then like shown in Fig. 2.6 (a). The membrane is only permeable to K^+ at rest, and thus the membrane resting potential V_r is very close to the resting potential for K^+. There are three intersection points of the membrane current and the voltage axis: the membrane resting potential V_r, a critical voltage V_{th}, and V_{peak}. Below the critical point V_{th}, an increase in membrane potential gives rise to a positive outward current, which hyperpolarizes the membrane and brings the membrane potential V_m back to V_r. When the membrane potential reaches V_{th}, an increase of the potential leads to a negative inward current, which depolarizes the membrane and further

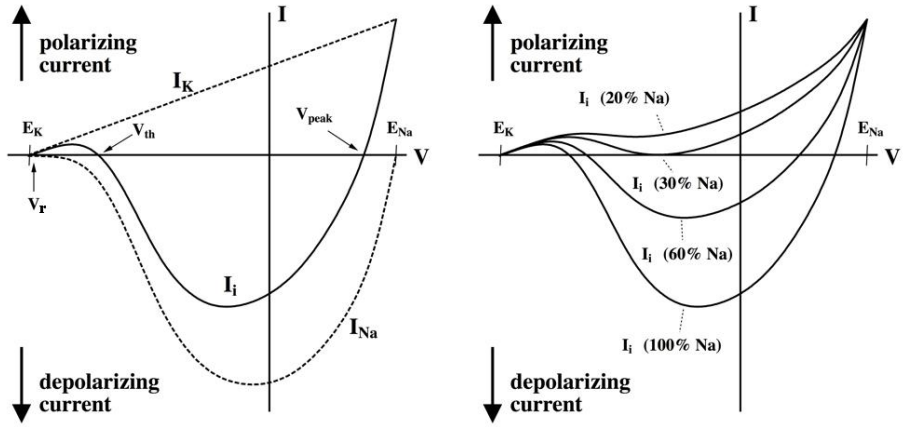

(a) (b)

Figure 2.6: (a) Characteristic voltage-current relations of potassium channel and sodium channel are shown in solid lines; the sum of both currents ($I = I_K + I_{Na}$) is shown in dashed line. Figure adapted from [27]. (b) The membrane current when different percentage of sodium current is blocked. The number of percentage in the figure is for the sodium channels that are still functioning, meaning not blocked by anesthetics. The calculation is done by Thomas Heimburg and the figures are kindly provided by him.

increases the membrane potential. This brings the V_m to V_{peak} which is the peak value of an action potential. The current changes the sign afterwards, so that the membrane is then hyperpolarized again. This means that it is only possible to initiate an action potential when the voltage pulse has a value above a threshold value V_{th}.

With the Noble's model, the local anesthetic effect can be intuitively understood. Anesthetics are drugs that cause a loss of sensation, usually used in surgeries to prevent the patients from pain. They can be categorized into two classes, i.e. local anesthetics that works in a limited local area, and general anesthetics that cause unconsciousness. Local anesthetics are generally believed to block the sodium channels. Fig. 2.6 (b) shows the membrane $I-V$ relations with different percentage of sodium channels blocked. With an increasing percentage of sodium channels blocked, the membrane $I - V$ curve moves close to the abscissa axis. The threshold V_{th} increases, meaning one needs to apply a stimulation pulse with a higher amplitude to excite the nerve; and the V_{peak} shifts to a lower value, meaning that the amplitude of the action potential decreases. Eventually, when only 30% sodium channels are left functioning, there is only one intersection point. This means that the membrane cannot be depolarized any more. As a result, the nerve cannot be excited any more. At this point, the intersection point is about 2.6 times of the initial value of V_{th}, meaning that the threshold of stimulation can be shifted to a maximum degree of 2.6 times. This contradicts with experimental findings which will be discussed in Chapter 5. As for general

anesthetics, there are large variations in structures. They are found to interact with different receptors. However, there is not a common explanation from HH theory.

2.2 Thermodynamic View of HH Model

The first law of thermodynamics is the conservation of energy for a thermodynamic system. The internal energy of a system is given by:

$$\begin{aligned} dE &= dQ + dW \\ &= dQ - pdV(-fdl - \Pi dA + HdM + \Psi dq + \sum_i \mu_i dn_i + \ldots) \end{aligned} \tag{2.17}$$

where dQ is the heat absorbed by the system; dW is work performed on the system, which can take the form of the work on volume (pdV), work on lines (fdl), work on area (ΠdA), magnetic polarization (HdM), electrical work (Ψdq) and chemical work ($\sum_i \mu_i dn_i$).

Only the electrical work term in this equation is covered by HH model. Therefore, from a thermodynamic point of view, HH model does not consider the total energy change, but only describes the action potential in the sense of electrical energy. However, it has been reported that during an action potential, there are also change of other properties, e.g. temperature and heat change, change in optical properties and mechanical properties including thickness and length. Besides, the nerve can be excited not only by an electrical pulse, but also by mechanical force [28] and local cooling [29, 30], among others. All these properties are not covered by HH model.

2.2.1 Mechanical Changes

It was first reported by Hill et al. in 1977 that the action potential is accompanied by a small rapid change in the diameter of the axon which has a period of about 1 millisecond and a typical amplitude 1.8 nm [31]. Later, Tasaki and colleagues did extensive study on the mechanical changes along with a nerve impulse. They found that the nerve fibers would swell during action potentials with a shortening effect in the length [32, 33, 34].

Recently, Gonzalez-Perez et al. studied the thickness change of lobster axons during an action potential with Atomic Force Microscope (AFM) [35]. The height profile of the nerve was measured by the AFM simultaneously with extracellular electrical recording. The experiment is schematically shown in Fig. 2.7 (a) and the results are shown in Fig. 2.7 (b). The results show that the action potential is accompanied by a thickness change in the nerve cylinder with two phases, an increase of the nerve thickness of about 1 nm, followed by a decrease phase back to the resting value. The change in thickness is in phase with the action potential.

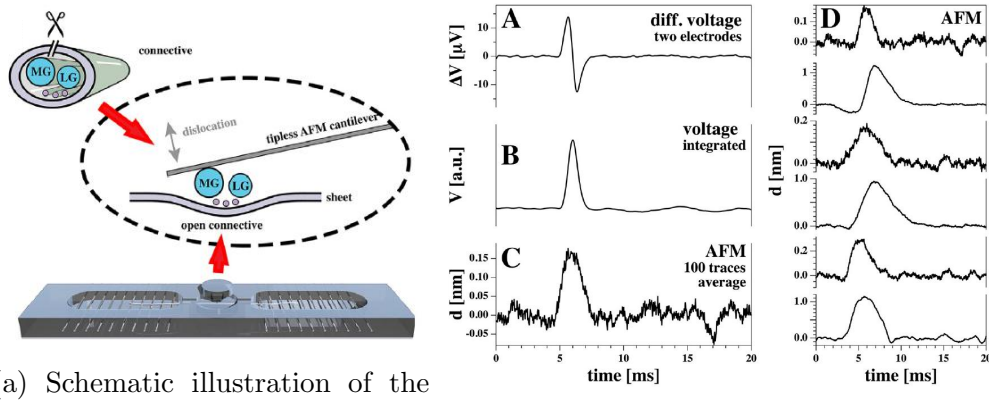

(a) Schematic illustration of the setup.

(b) Results from measurements.

Figure 2.7: (a) Schematic illustration of the setup. The sheath of a lobster circumesophageal connective was cut open and the giant axon was exposed. A tipless cantilever was kept at a certain height above the giant axon in the middle of the nerve. The nerve was placed on a chamber with electrodes below the nerve at each end. The height change was recorded along with extracellular electrical recording. (b) A. Extracellular recording of action potentials; B. the real shape of action potential from an integral of A; C. an example from mechanical measurements with 100 averages; D. results of mechanical measurements from several nerve species. Figures taken from [35].

2.2.2 Optical Changes

A number of studies have shown optical changes in nerves associated with an action potential since the 1960s. These measurements include fluorescence [36], light scattering [37, 36, 38], birefringence [36, 37, 39], absorbance [40], and optical rotation [41] etc. As an example, Fig. 2.8 shows the results from electrical and optical measurements on nerves from a spider crab.

The nerves from a spider crab were stained with a fluorescence marker 8-anilinonaphthalene-1-sulfonic acid (ANS) which is extremely sensitive to conformational changes of various molecules. The changes of fluorescence intensity in fluorescence measurement and light intensity in light scattering during a nerve impulse were shown to have similar shapes and time scales with those of an action potential.

2.2.3 Heat Changes

The measurement of the heat produced during a nerve impulse dates back to the 19th century. Several attempts [42] were made, however no appreciable heat change was measured. Until the early 20th, with the development of a thermoelectric system based on thermopiles and galvanometers in Hill's group, it became possible to measure the temperature change from the activity of excitable cells. The measurement system was first applied to measure the temperature changes in muscles [43], which led A. V. Hill to a Nobel prize in 1922 for his work in

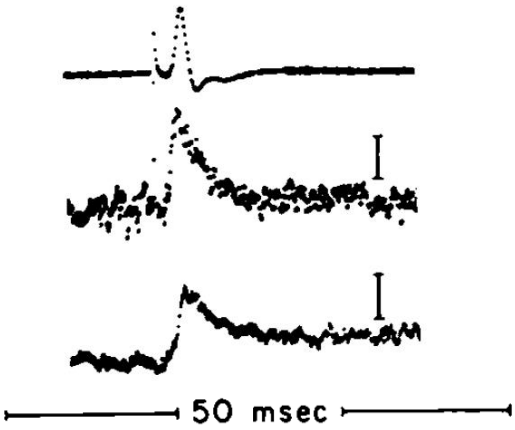

Figure 2.8: Electrical and optical measurement on nerves from spider crabs. The upper trace is from the extracellular recorded action potential with an amplitude of approximately 2 mV. The middle trace is the optical signal from fluorescence measurement, with the vertical bar representing a 2×10^{-5} times increase in fluorescence intensity. The lower trace is the time course of change in light scattering at 90° observed a stained nerve. The vertical bar represents a 4×10^{-6} times increase in light intensity. Figure adapted from [36].

discovering the distinction between aerobic and anaerobic metabolism. He also studied the heat change during a nerve impulse but did not measure any change in temperature at the beginning [44].

Later they managed to improve the sensitivity of the measurement system and measured a heat release during a nerve impulse at the scale of about 10^{-3} cal/g·min for several nerve species [45]. Until 1958, the time resolution was high enough to resolve two phases of the heat production: a fast positive heat production, followed by a slower (300 ms) absorption of heat nearly as large as the heat produced [46]. Similar results measured for other species of nerves later confirmed this observation. Fig. 2.9 shows (A) the measured temperature change during a nerve impulse from pike olfactory nerves and (B) the calculated heat block pattern dQ/dt, which consists of a positive (heat release) phase followed by a negative (heat reabsorption) phase. As a control experiment, the authors locally heated the nerve with a Peltier device, and found the heat dissipated with a much slower process. This indicates that the reabsorption phase is not due to heat diffusion into water. Besides, it cannot be connected with 'pumping back' Na^+ and K^+ ions, which is a much slower process and would release heat as well. This suggests that it is very likely that both phases of the heat change are related to the nerve impulse.

From the 1980s, Tasaki and his colleagues measured the heat change during action potential with thermal detector made of pyroelectric polymer polyvinylidene fluoride (PVDF) that has a better time-resolution. They confirmed the

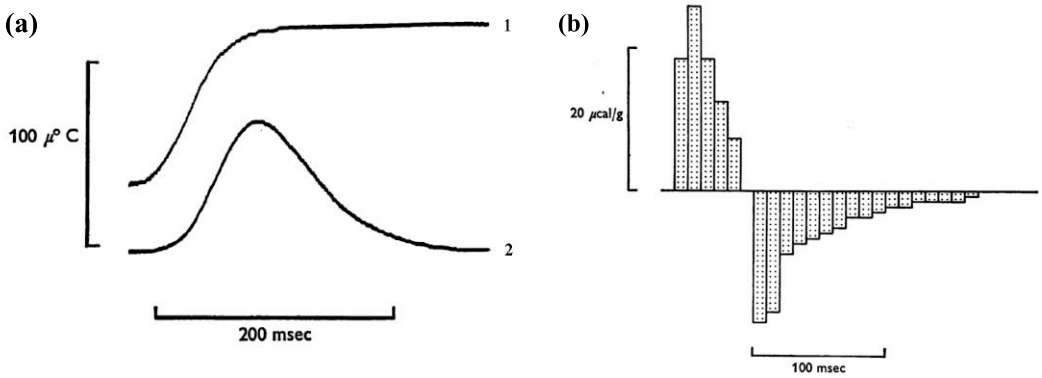

Figure 2.9: (a) The temperature change in pike olfactory nerves: 1 temperature control with the nerve locally heated by a Peltier device; 2 temperature change during a nerve impulse. (b) heat block pattern calculated from curve 2 in (a); the heat is first positive and then negative, meaning that heat is first released from the nerves followed by a reabsorption in the second phase. Figures adapted from [47].

two-phase properties of heat curve during nerve impulse, i.e. a fast initial phase of heat release followed by a relatively slow reabsorption phase [34, 48, 49]. However, they found that the thermal relaxation (half-maximal) time was much faster than previously reported, usually between 30 and 60 ms (Fig. 2.10). They conducted such experiments and got similar results in both non-myelinated nerves and myelinated nerves. Both groups showed that there is no net change of heat

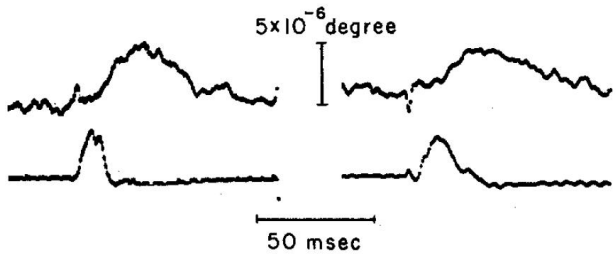

Figure 2.10: Upper traces: Temperature changes in the nerves from claws of lobsters during a nerve impulse; lower traces: action potentials recorded extracellularly. Figure taken from [48].

during a nerve impulse. The whole process of a nerve impulse looks like an adiabatic pulse with no heat dissipated.

All the property changes mentioned above are not covered by the HH model, especially the reversible heat change as it is a pure electrical model. According to the equivalent circuit in HH model, ions flow across the membrane through resistors, which typically will heat up due to friction when there is a current flow

regardless of the direction. The heat dissipation of currents should be

$$\frac{dQ}{dt} = P = I \cdot U \cong \sum_i g_i (V - E_i)^2 \tag{2.18}$$

where Q is the heat, P is the rate of heat change which corresponds to the power of the electrical circuit, g_i is the conductance of ionic resistors which always takes a positive value, V is the membrane potential, and E_i is the resting potential for each ions. Therefore, based on HH model, no matter which direction the ion travels, the heat dissipations add up to a very large value and should alway stay positive. This contradicts the experimental findings discussed above.

2.2.4 Lipid Channels

When fluorescence markers or labeled-Na^+ are contained inside pure lipid vesicles and the temperature is changed, one observes the diffusion of them out of the vesicles in the phase transition range, with a maximum diffusion rate at the melting point [50]. This indicates that protein-free lipid membranes are permeable to ions and small molecules. Therefore, when the membrane is close to the transition, the lipid bilayer is not a perfect capacitor anymore.

The protein channel functions are usually characterized with patch-clamping technique, which measures the current as a function of time with membrane potential fixed at a certain value by the feedback circuit [51]. Channel-like events have also been found in pure synthetic lipid membranes in the absence of proteins close to the phase transitions. The lipid channels reported typically have similar conductance from tens to hundreds of pS, and similar lifetime as those observed in the presence of proteins [52]. Lipid channels display moderate selectivity [53, 54] and are found to be blocked by anesthetics and small drugs, in the same manner with that of channel proteins [55]. The magnitude of currents is a function of membrane voltage and ion species [54]. Fig. 2.11 shows typical results from patch-clamp measurements on membranes in the presence and absence of proteins, respectively. It is difficult to distinguish these two events.

Based on the phenomena that the HH model cannot explain, and the fact that the lipid membranes in the absence of proteins provide a path for ionic currents, one may then wonder, are the protein channels really responsible for the conduction of ions across the membrane in a nerve impulse? Should we consider other possible explanations for nerve impulses?

Below a theory proposed by Heimburg and Jackson [57], which describes the nerve impulse from a thermodynamic point of view, will be introduced.

2.3 Soliton Model

In 2005, Heimburg and Jackson proposed an alternative model (referred to as 'Soliton model' hereafter) which considers the nerve impulse as localized sound

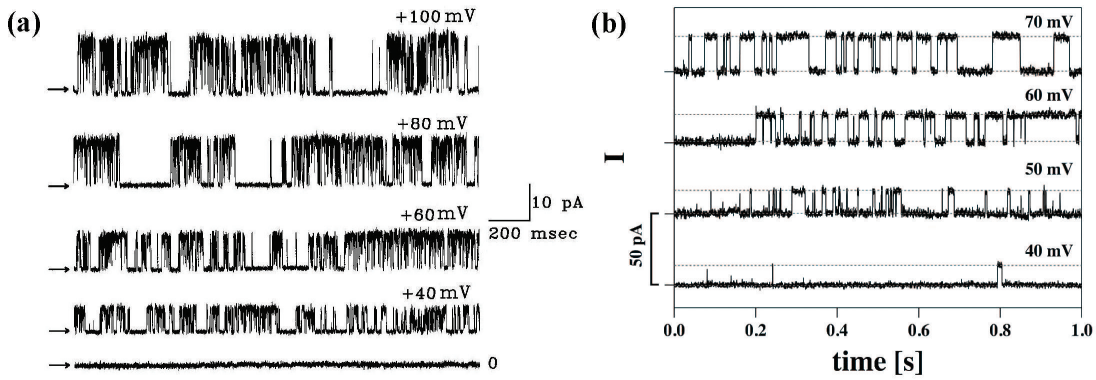

Figure 2.11: Channel events in protein ion channel and lipid channel. (a) Single-channel recording of at several holding potentials. Arrows indicate closed state of channel. Figure adapted from [56]. (b) Current-traces for a DMPC:DLPC=10:1 mol/mol membrane (150 mM KCl, T=30 ℃) at four voltages. Figure adapted from [52].

waves propagating along the axon membrane without distortion, like solitons. For the existence of solitons, the medium in which the soliton propagates should have two properties: non-linearity and dispersion. Non-linearity means that the speed of sound is a non-linear function of lateral density, and dispersion refers to the frequency dependence of the speed of sound. Biological membranes have both properties close to the phase transition [57]. Figure. 2.12 shows the non-linearity

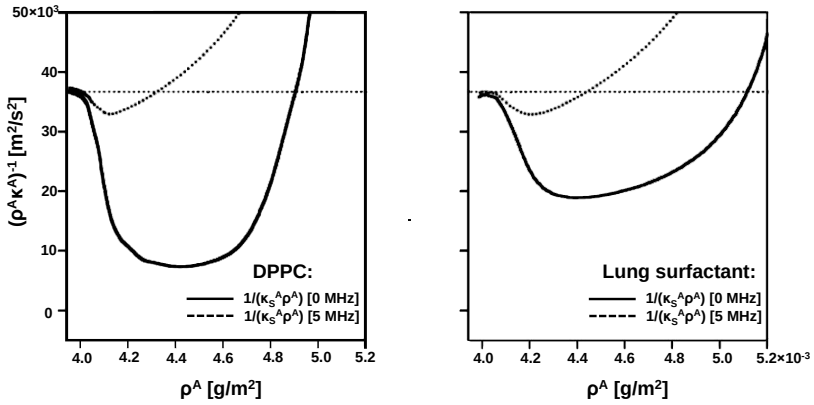

Figure 2.12: The sound velocity $c^2 = 1/(\kappa_S^A \rho^A)$ as a function of lateral density ρ^A at two different frequencies 0 MHz and 5 MHz: The left figure is for DPPC large unilamellar vesicles at $T = 45$ ℃; the right figure is for lung surfactant at $T = 37$ ℃. Figure taken from [57].

and dispersion properties of an artificial lipid membrane DPPC and a biological sample lung surfactant in the phase transition.

In physiological conditions, biological membranes are in the fluid phase. They display phase transitions similar to artificial lipid membranes. The transition is always found slightly below physiological temperature [57, 58, 59]. Fig. 2.13 shows several examples of such transitions in biological samples. The lipid melt-

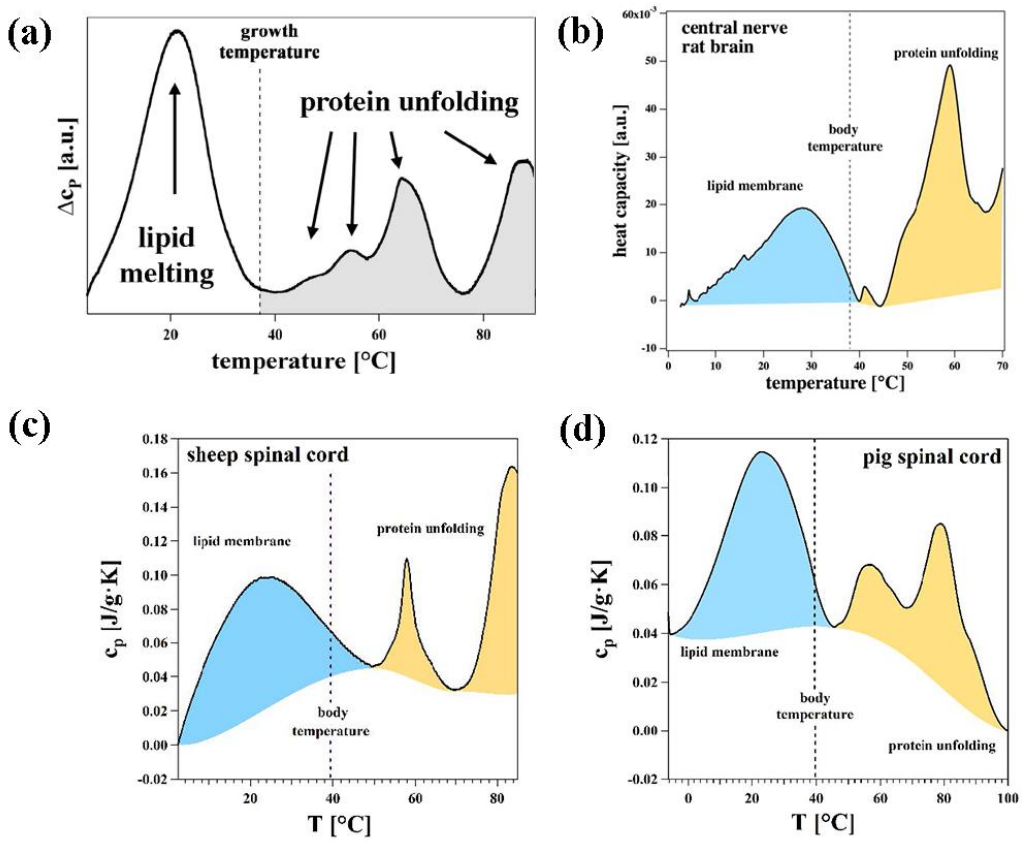

Figure 2.13: Heat capacity profiles of membranes from (a) E. coli (Figure taken from [57]); (b) from rat brain (Figure taken from [59]); (c) sheep spinal cord (Figure taken from [58]; (d) pig spinal cord (Figure taken from [58]. The vertical dashed line shows the physiological temperature of each species. The peak for lipid melting is shown in white or blue, and peaks for protein unfolding are shown in gray or yellow.

ing transition in all cases are found close to and slightly below the physiological temperatures. At different growth temperatures, the organisms adjust their lipid composition so that the membranes conserve their physical properties [60, 61], including that the melting temperature of lipid membranes is kept always just below the body temperature. The Soliton model states that during a nerve impulse, the nerve membrane goes through a phase transition from the fluid phase to the gel phase, followed by a transition back to the resting fluid state.

2.3.1 Elastic Constants

The speed of sound in fluid is related to the compressibility and density of the medium. Compressibilities are found to change significantly and display a pronounced maxima in the lipid melting transition [62]. The lateral compressibility in transition can be derived from the heat capacity profiles [57], which will be demonstrated in the following.

Heat capacity is defined as

$$c_p = \frac{dQ}{dT} = \left(\frac{d\langle H\rangle}{dT}\right)_p \tag{2.19}$$

where $\langle H\rangle$ is the mean enthalpy of the system given by:

$$\langle H\rangle = \frac{\sum_i H_i exp(-H_i/RT)}{\sum_i exp(-H_i/RT)} \tag{2.20}$$

where $H_i = E_i + pV_i$ is the enthalpy of state i.

The area compressibility is defined as

$$\kappa_T^A = \frac{1}{\langle A\rangle}\left(\frac{d\langle A\rangle}{d\Pi}\right)_T ; \quad \langle A\rangle = \frac{\sum_i A_i exp(-H_i/RT)}{\sum_i exp(-H_i/RT)} \tag{2.21}$$

where Π is the lateral pressure, p is the hydrostatic pressure and $\langle A\rangle$ is the mean area. The heat capacity c_p and the isothermal area compressibility κ_T^A are related to the fluctuations in enthalpy and area in the following manner

$$c_p = \frac{\langle H^2\rangle - \langle H\rangle^2}{RT^2} \qquad \kappa_T^A = \frac{\langle A^2\rangle - \langle A\rangle^2}{\langle A\rangle \cdot RT} \tag{2.22}$$

Derivation details of Eq. 2.22 from Eq. 2.19, Eq. 2.20, Eq. 2.21 can be found in Appendix A. The excess area change ΔA is found experimentally to be proportional to the excess enthalpy change ΔH in the lipid melting trasition region [62, 63]

$$\Delta A(T) = \gamma_A \Delta H(T) \tag{2.23}$$

The value of the constant $\gamma_A = 8.9 \times 10^3$ cm^2/J is identical for various phosphatidylcholines, lipid mixtures, lung surfactant and E. coli [64, 57]. The total area compressibility can then be obtained by

$$\kappa_T^A = \kappa_{T,0}^A + \Delta\kappa_T^A = \kappa_{T,0}^A + \frac{\gamma_A^2 T}{\langle A\rangle}\Delta c_p \tag{2.24}$$

where $\kappa_{T,0}^A$ is the area compressibility outside the phase transition. From the above, the isothermal area compressibility in the lipid melting transition has been derived from the heat capacity profile which can be measured by DSC.

The speed of sound in elastic media is a function of isentropic lateral compressibility κ_S^A,

$$c_0 = \sqrt{1/\rho^A \kappa_S^A} \tag{2.25}$$

One can show a relation between isentropic area compressibility and isothermal area compressibility using Maxwell's relations [57]

$$\kappa_S^A = \kappa_T^A - \frac{T}{\langle A\rangle c_p^{system}(\omega)} \cdot \left(\frac{dA}{dT}\right)_p^2 \tag{2.26}$$

where κ_T^A is the isothermal compressibility that can be calculated from the heat capacity profile according to Eq. 2.24; $\langle A \rangle$ can be calculated from the change of area according to Eq. 2.23 given the starting area; $\left(\frac{dA}{dT}\right)_p$ is proportional to the change of enthalpy which can be calculated by integral of the heat capacity profile (Eq.2.23); $c_p^{system}(\omega)$ is the source of dispersion (frequency dependence), which depends on the time scale of the compression. If we allow the system to exchange heat for a long time, the time scale is much longer than the relaxation of the membrane. The aqueous environment will absorb heat as a heat reservior, and $c_p(\omega)$ will go infinity, thus $\kappa_S^A \approx \kappa_T^A$. The lateral speed of sound is then given by $c = \sqrt{1/\kappa_T^A \rho^A}$.

2.3.2 Solitons in Nerves

The soliton model is based on the equation for sound propagation. For the propagation of sound, we can write down the wave equation

$$\frac{\partial^2 \rho}{\partial t^2} = div(c^2 grad\rho) \tag{2.27}$$

Assuming that a nerve axon is a long, narrow, homogeneous cylinder with its longitudinal axis on the x direction, the equation for 1D sound propagation in the absence of dispersion is

$$\frac{\partial^2}{\partial t^2}\Delta\rho^A = \frac{\partial}{\partial x}\left(c^2\left(\frac{\partial}{\partial x}\Delta\rho^A\right)\right) \tag{2.28}$$

where $\Delta\rho^A = \rho^A - \rho_0^A$ is the change in lateral density of the axon membrane which is a function of x and t, and c is the speed of sound. Since the speed of sound is a non-linear function of lateral density and frequency in the vicinity of lipid phase transition as described above, it can be expanded to second order to represent the non-linearity,

$$c^2 = c_0^2 + p\Delta\rho^A + q(\Delta\rho^A)^2 + \dots \tag{2.29}$$

where c_0 is the speed of sound in the fluid phase of the membrane far from the transition region. $p < 0$, $q > 0$ are the Taylor expansion coefficients that can be obtained by quadratic fitting of the speed of sound to the lateral density. For dispersion, the speed of sound c is a function of frequency ω

$$c = f(\omega) \tag{2.30}$$

It can be expanded as follows

$$c^2 = c_0^2 + \left(\frac{\partial c^2}{\partial \omega}\right)_0 w + \frac{1}{2}\left(\frac{\partial^2 c^2}{\partial \omega^2}\right)_0 \omega^2 + \dots \tag{2.31}$$

Since the speed of sound is time reversible and frequency reversible,

$$c^2 = c_0^2 + \frac{1}{2}\left(\frac{\partial^2 c^2}{\partial \omega^2}\right)_0 \omega^2 = c_0^2 + h_0\omega^2 \tag{2.32}$$

This is the most simple dispersion relation. In mechanical system $h_0 > 0$ as c is larger when frequency is larger.

The dispersion term was approximated to take a simple form in [57], $-h\partial^4\Delta\rho^A/\partial z^4$ with $h > 0$ to account for the positive frequency correlation of sound velocity. It is shown in appendix B that the dispersion term added to the equation is meaningful for the nerve system. The final equation of Soliton model then takes the form of

$$\frac{\partial^2}{\partial t^2}\Delta\rho^A = \frac{\partial}{\partial x}((c_0^2 + p\Delta\rho^A + q(\Delta\rho^A)^2)\frac{\partial}{\partial x}\Delta\rho^A) - h\frac{\partial^4}{\partial x^4}\Delta\rho^A \tag{2.33}$$

Continuing with solving the equation, by moving the coordinate system to $z = x - vt$, with v being the velocity of pulse, the differential equation will be time-independent. In this case, $\partial\Delta\rho^A/\partial x = \partial\Delta\rho/\partial z$, $\partial\Delta\rho^A/\partial t = -v\partial\Delta\rho^A/\partial z$. The soliton equation will be transformed into

$$v^2\frac{\partial^2\Delta\rho^A}{\partial z^2} = \frac{\partial}{\partial z}[(c_0^2 + p\Delta\rho^A + q(\Delta\rho^A)^2)\frac{\partial}{\partial z}\Delta\rho^A] - h\frac{\partial^4\Delta\rho^A}{\partial z^4} \tag{2.34}$$

integrate against z twice,

$$h\frac{\partial^2\Delta\rho^A}{\partial z^2} = (c_0^2 - v^2)\Delta\rho^A + \frac{1}{2}p(\Delta\rho^A)^2 + \frac{1}{3}q(\Delta\rho^A)^3 \tag{2.35}$$

then multiply both sides of the equation by $\partial\Delta\rho^A/\partial z$, and integrate again

$$h(\frac{\partial\Delta\rho^A}{\partial z})^2 = (c_0^2 - v^2)(\Delta\rho^A)^2 + \frac{p}{3}(\Delta\rho^A)^3 + \frac{q}{6}(\Delta\rho^A)^4 \tag{2.36}$$

This equation has pulse-like solutions, and it is symmetrical to z. Therefore ρ^A must have a maximum at $z = 0$. For large z, $(\Delta\rho^A)^3, (\Delta\rho^A)^4$ will be very small and thus could be neglected. Eq. 2.36 is then turned into

$$h(\frac{\partial\Delta\rho^A}{\partial z})^2 = (c_0^2 - v^2)(\Delta\rho^A)^2 \tag{2.37}$$

$$\sqrt{h}\frac{\partial\rho^A}{\partial z} = \sqrt{c_0^2 - v^2}\cdot\Delta\rho^A \tag{2.38}$$

Solutions with the form of exponential decay $\Delta\rho^A \sim exp(-\sqrt{\frac{c_0^2 - v^2}{h}}|z|)$ can be obtained. pulse-like solution can only be obtained if $v < c_0$ (when $v > c_0$, no localized solution can be obtained). At the maximum, the left side of Eq. 2.36 is zero, and the right side has an analytical solution:

$$\Delta\rho = \frac{-\frac{p}{3} \pm \sqrt{\frac{p^2}{9} - \frac{4q}{6}(c_0^2 - v^2)}}{\frac{q}{3}} = -\frac{p}{q} \pm \frac{p}{q}\sqrt{1 - \frac{6q}{p^2}(c_0^2 - v^2)} \tag{2.39}$$

v has a limit of $v \leq c_0$, another limit is when the term under square root equals to zero, there is a minimum velocity

$$v_{limit}^2 = c_0^2 - \frac{p^2}{6q} \tag{2.40}$$

with a maximum amplitude of

$$\Delta\rho_{max,limit}^A = \frac{|p|}{q} \tag{2.41}$$

Fig. 2.14 shows the soliton profiles calculated for DPPC large unilamellar vesicles. with increasing amplitude, the velocity decreases. The black curve

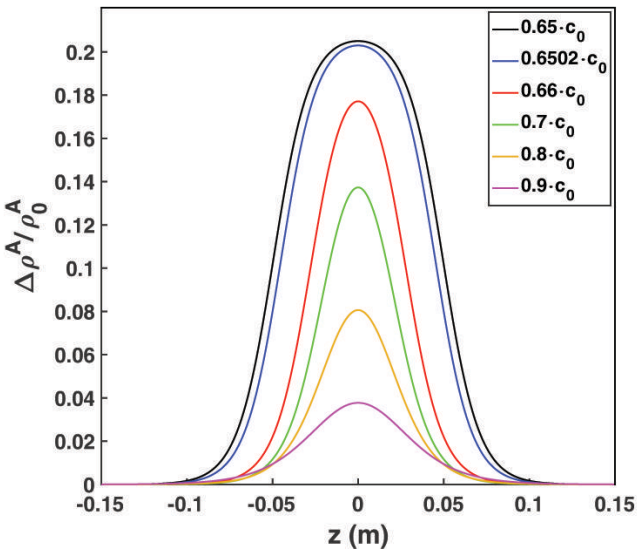

Figure 2.14: Soliton profiles calculated for DPPC large unilamellar vesicles (LUV) at $T = 45$ °C for different velocities, $0.65 \cdot c_0$, $0.6502 \cdot c_0$, $0.66 \cdot c_0$, $0.7 \cdot c_0$, $0.8 \cdot c_0$ and $0.9 \cdot c_0$, respectively. Figure based on the Soliton model [57].

represents the limiting soliton profile with a minimum velocity.

2.3.3 Nerve Impulses in Soliton Model

The Soliton model can reasonably explain several observations which are not explained by the HH model.

According to Soliton model, the membrane of the nerve goes through a phase transition from the fluid phase to the gel phase, and then back to the fluid phase during a nerve impulse. With DPPC membrane going through the whole phase transition, there is a volume change of 4.7% and an area change of 24.6%, with the corresponding thickness change to be 16% (7.4 Å). In the calculated soliton profile (Fig. 2.14), the maximum change in lateral density is about 21%, meaning that the membrane is pushed through about 85% of the transition. This corresponds

to a thickness change of 6.4 Å, and thus a thickness change of the membrane cylinder of 1.28 nm. This is of the same order what has been measured in the mechanical experiments [32, 33, 35]. As a consequence of piezoelectric effect, the membrane potential change is estimated to be an order of around 50 mV.

In addition, if we rethink about the components of the membrane current, it consists of a capacitive part by charging the membrane capacitor, I_c, and an ionic part by ions moving through the resistors of channel proteins, I_i

$$I = I_c + I_i \tag{2.42}$$

As the charge on a planar capacitor is given by $Q = C \cdot \Delta V$, the capacitive current is therefore

$$I_c = \frac{dQ}{dt} = C\frac{dV}{dt} + V\frac{dC}{dt} \tag{2.43}$$

where C is the capacitance of the membrane. The second term $V\frac{dC}{dt}$ on the right hand of Eq. 2.43 is zero when capacitance C is constant, which is assumed in HH model during an action potential based on the value outside the membrane transition.

The differential equation in HH model describing the nerve impulse propagation is

$$\frac{a}{aR_i}\frac{\partial^2 V}{\partial x^2} = C_m\frac{\partial V}{\partial t} + \sum_i g_i(V - E_i) \tag{2.44}$$

where $C_m\frac{\partial V}{\partial t}$ is the capacitive current through a capacitor with a constant capacitance C_m. However, the change in membrane dimension during a nerve impulse would result in a change in the membrane capacitance. Therefore, the capacitive current should instead be given by

$$I_c = C_m\frac{\partial V}{\partial t} + V\frac{\partial C_m}{\partial t} \tag{2.45}$$

with the second term accounting for the change in the dimension.

The optical observations of nerve impulse can also be easily understood with the change in the arrangement and conformation of lipid molecules, and the thickness of the membranes in the phase transition. Regarding the heat change, the membrane first goes through a phase transition from the fluid phase to the gel phase, which releases heat. Subsequently, it goes through a phase transition of the opposite process, i.e. from the gel phase to the fluid phase, which will absorb exactly the same amount of heat released. Overall, the nerve impulse is a reversible adiabatic process with not net heat change. This reasonably explains the heat change measured in experiments mentioned in Sec. 2.2.3. In Chapter 5, a further explanation of the heat change during a nerve impulse and an oscillation reaction that shares the same adiabatic feather will be discussed with linear non-equilibrium thermodynamics.

2.3.4 Anesthesia in Soliton model

A variety of substances with different chemical structures cause anesthesia, including ester-based, amide-based, chloroform, N_2O, noble gas Xenon etc. Interestingly, Meyer and Overton found that they all obey a common rule [9, 65, 66]. The effective anesthetic dose (ED_{50}), i.e. the effective concentration of anesthetics in air or water at which 50% of the organisms studied are anesthetized, is linearly proportional to their solubility in olive oil. Overton noticed that cell

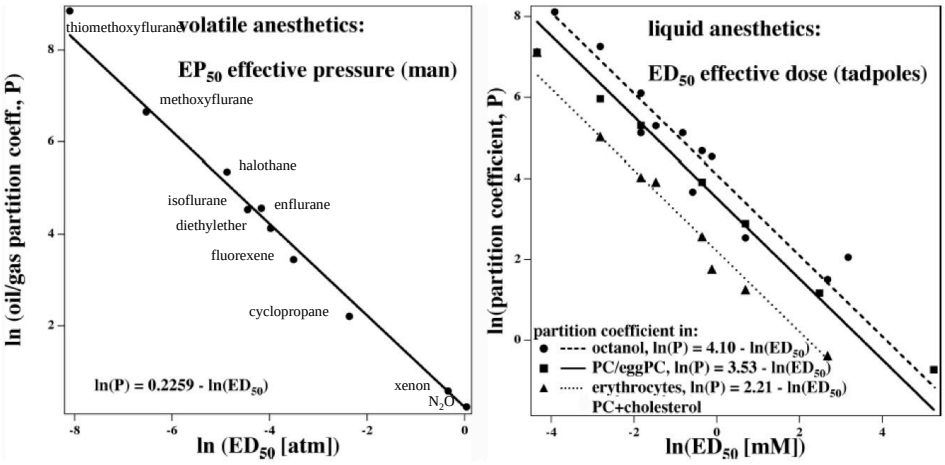

Figure 2.15: The oil/gas partition coefficient for volatile anesthetics, or the oil/water partition coefficient for liquid anesthetics is linearly dependent on the critical anesthetic dose (EP_{50} for volatile anesthetics and ED_{50} for liquid anesthetics). The plots are in logarithm scale, one always finds a slope -1. Figure taken from [9], with the left figure originally adapted from [66], and data of the right figure from [67].

membranes have many common properties with olive oil. Therefore, it can also be stated that the critical anesthetic dose is proportional to the solubility in lipid membranes. This is true for PC membranes as shown in Fig. 2.15. It was later found that anesthetics lower the melting point of lipid membranes.

Fig. 2.16 shows the effect of local anesthetic lidocaine on DMPC membranes. Assuming that anesthetic molecule dissolves very well in fluid phase, but not at all in the gel phase, the shift of the melting point can be described by the freezing point depression law,

$$\Delta T_m = \frac{RT_m^2}{\Delta H} x_A \tag{2.46}$$

where T_m is the melting temperature (freezing point), R is the gas constant, ΔH is the enthalpy change in the transition, and x_A is the molar fraction of the anesthetic molecules. As anesthetics shift the melting transition to a lower temperature, the phase transition is moved further away from the physiological temperature. Therefore, it requires a higher free energy to push the membranes through the transition, resulting in a shift in the stimulus threshold to activate

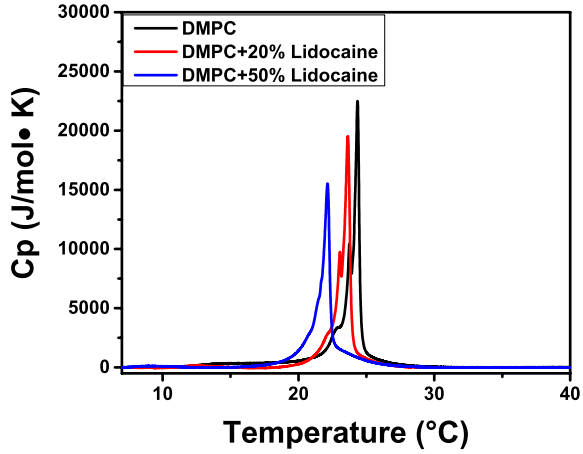

Figure 2.16: The effect of lidocaine on the phase transition of 1,2-dimyristoyl-sn-glycero-3-phosphocholine (DMPC) unilamellar vesicles. Measured in the lab of Membrane Biophysics group, Niels Bohr Institute.

the nerve. As long as anesthetics continue shifting the melting point and the nerve keep the vitality, there is not such a limit of 2.5 times for the threshold shifting. This applies to both local anesthesia and general anesthesia.

Chapter 3

Materials and Methods

3.1 Materials

Nerves: The nerves used in the thesis are from lobster, *Homarus americanus*, earthworm *Lumbricus terrestris* and frog (*Rana Esculenta*). Lobsters were imported from Canada by a local supplier. Canadian worms were purchased from a local pet shop. Frog sciatic nerves were provided by our collaborator from Department of Experimental Medicine, University of Copenhagen.

Nerves are kept in solutions with similar ionic composition to the extracellular fluids of each animal species after dissection. Lobster saline solution:
• 462 mM NaCl (VWR Chemicals, Belgium), 16 mM KCl (Sigma-Aldrich, USA), 26 mM $CaCl_2$ (MERCK Eurolab), 8 mM $MgCl_2$ (Sigma-Aldrich, USA), 10 mM TRIS and 11 mM Glucose (Sigma-Aldrich, USA), adjusted to pH 7.4 with HCl ($\geq$37%, Sigma-Aldrich, USA) [68].
• Earthworm Ringer's solution: 75 mM NaCl, 4 mM KCl, 2 mM $CaCl_2$, 1 mM $MgCl_2$, 10 mM TRIS, and 23 mM glucose, adjusted to pH 7.4 with HCl [69].
• Frog Ringer's solution: 115 mM NaCl, 2.5 mM KCl, 1.8 mM $CaCl_2$, 1.08 mM $Na_2HPO_4{\cdot}2H_2O$, 0.43 mM $NaH_2PO_4{\cdot}H_2O$. A high potassium concentration solution was used to make frog nerves inexcitable, with NaCl replaced entirely by KCl to a final K^+ concentration of 117 mM [70].

Ethics: Experiments with lobster and earthworm have been carried out in accordance with the policy on the use of animals of the (American) Society for Neuroscience and the US Guide for the Care and Use of Laboratory Animals [71]. The experiments presented here with frog nerve were conducted in accordance with the University of Copenhagen Animal Ethics Policy [72] and a license is not required. The frogs used were handled by the animal facility at the Department of Experimental Medicine at the University of Copenhagen which is accredited by the Association for Assessment and Accreditation of Laboratory Animal Care International (AAALAC) [73].

Briggs-Rauscher solutions: Solution 1 KIO_3 (Sigma-Aldrich, USA) 3 g/100 ml; **Solution 2** H_2O_2 (30%, VWR Chemicals, Belgium) 33 ml (+67 ml

H_2O), $HClO_4$ (70%, Sigma-Aldrich, USA) 2 g/100 ml; **Solution 3** Malonic acid (Sigma-Aldrich, USA) 1.56 g/100 ml, $MnSO_4$ (Sigma-Aldrich, USA) 0.34 g/100 ml, H_2SO_4 (95-97%, MERCK, Germany) 0.24 g/100 ml, Starch 1 g/100 ml (indicator); **Solution 4** $MnSO_4$ 0.3 g/100 ml.

Lipid: 1,2-dipalmitoyl-*sn*-glycero-3-phosphocholine (DPPC) was purchased from Avanti Polar Lipids (Alabaster/AL, USA), stored at -20 ℃, and used without further purification. Chloroform was purchased from MERCK, Germany. Electrolyte solution for lipid sample contains 150 mM KCl, 1 mM EDTA, 1 mM HEPES, pH adjusted to ~ 7.4.

Lidocaine($\geq$98%) was purchased from Sigma-Aldrich. All chemicals were used without further purification. All water used was Milli Q water (18.1 MΩ) from Direct-Q® 3 UV water purification system.

3.2 Sample Preparation

3.2.1 Nerve Samples

Lobster nerves: The dissection process of lobsters generally follows that described in [74]. Important steps are further described as follows. Lobsters are received alive and kept moist at 4 ℃ before dissection. The lobster is first kept upside-down to keep it relaxed and to minimize the movement (Fig. 3.1 (a)). When it stops moving, it is put on the table with all the legs and the tail spread unfolded. The head of the lobster is first chopped off when the cumoesophageal connectives (connected to the brain) are not used in the experiments. Claws and legs are amputated at the joint with the body and kept in the saline solution at 4 ℃ before use. Then the lobster is flipped upside down and cut in the middle into two parts, the body part and the tail part. Continuing with the upper part, the carapace, viscera, muscles are removed, and the cephalothoracic cavity is exposed. The connections along the cavity are cut with a pair of dissection scissors horizontally (Fig. 3.1 (b)). The ventral cord is lying under the cavity (Fig. 3.1 (c)). There are five ganglia of thoracic nerve cord where the nerve is connected with the tissues around. which need to be cut before removing the ventral cord. If the cumoesophageal connectives are needed for experiments (Fig. 3.1 (d)), the stomach is gentally removed and the connections between the two connectives and surrounding tissues are cut, so that the ventral cord from the brain all the way to the 5th pair of thoracic connectives can be fully removed. The nerve is kept in lobster saline solution before use. Holding the tail of lobster in one hand with the carapace in the palm, the edges between the abdomen and carapace are cut, subsequently between the abdomen and muscles, and then the abdomen together with the abdominal ventral cord can be removed (Fig. 3.1 (e)). The abdomen is put in a petri dish with lobster saline solution. The connections between the ventral cord and muscles around need to be cut so that the ventral cord can be

freely removed. The abdominal ventral cord is keep in the saline solution at 4 ℃ before use.

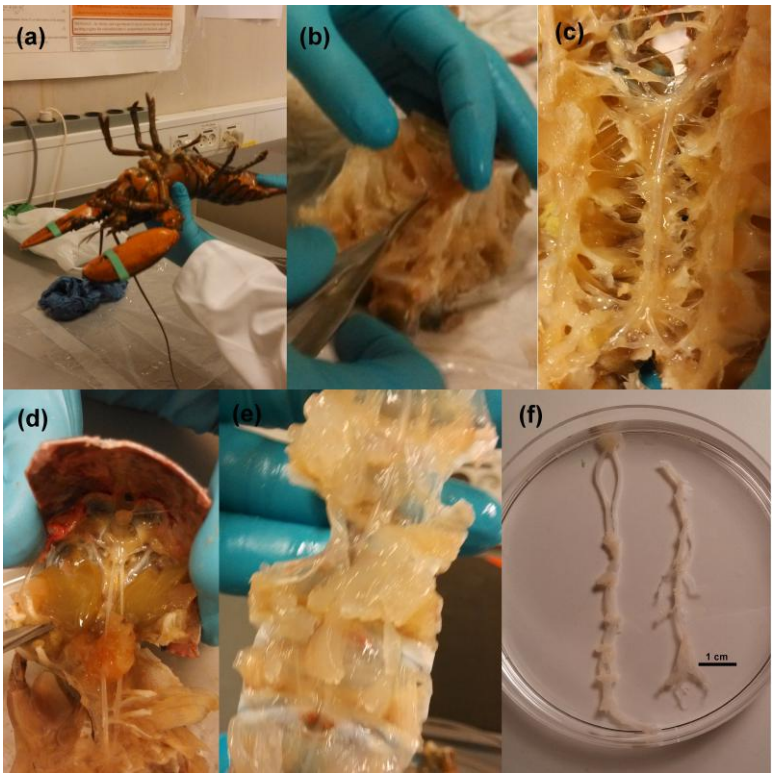

Figure 3.1: Dissection process of a lobster: (a) Flipped the lobster upside down for it to relax; (b) insert one side of the scissors horizontally below the cavity and cut along the middle of the cavity; (c) The exposed ventral cord (transparent) after cutting open the cavity; (d) cumoesophageal connectives (transparent) and the stomach (red) in the middle. (e) The abdominal ventral cord is attached to the skin; (f) the extracted ventral cord in two parts placed in the saline solution.

Earthworm ventral cord: The earthworm is put into 10% ethanol solution for about 7 minutes until it stops moving, i.e. to anesthetize it. The skin is then washed with tap water quickly to remove the residual ethanol, and water drops on the worm skin are dried with tissue paper. The worm is subsequently placed in a dissecting petri dish with the dorsal side up and stabilized with pins. The skin is stabbed with the tip of scissors from above the head, and cut all the way down about 3 cm before the clitellum with the scissors as horizontal as possible. Care is taken not to damage the internal organs. The skin is then spread out and pinned all the way down with pins angled out to keep them out of the way. The intestine is gently pushed aside with forceps and removed. The transparent ventral cord is then exposed. The nerve runs along the length of the worm with connections to surrounding muscles at each ganglia. It is necessary to drop some saline solutions on the interior of the opened worm once in a while to keep the nerve moist. The blood vessel on top of the ventral cord is gently removed with

scissors, and all the connections around and below are cut. Finally the ventral cord is removed with scissors and kept in a petri dish with earthworm saline solution. The nerve is usually kept in the solution before use for at least about 10 min after being cut off from the body.

3.2.2 Lipid Samples

DPPC lipid powders are taken out of the fridge and thawed to room temperature with the container sealed to avoid absorption of water from the environment.

A stock solution of DPPC is prepared by dissolving the powder in chloroform to a concentration of 10 mM. Lidocaine stock solution is prepared in the same way to a concentration of 10 mM.

DPPC and lidocaine mixtures are obtained by mixing the two stock solutions at the desired ratio in a vial.

The mixed samples are then dried under a gentle stream of nitrogen for about half an hour to remove the solvent. Subsequently the samples are dried under vacuum for at least four hours to completely remove the solvent.

The dried lipid/lipid-lidocaine samples are resuspended in buffer solution to a final lipid concentration of 10 mM. The samples are then heated above melting temperature and vortexed until a uniformly milky solution is formed, which is multilamellar vesicles (MLVs) solution.

The multilamellar vesicle solution is subsequently extruded through a filter membrane with pores of 0.1 μm in diameter (Whatman Nuclepore Track-Etch Membrane). This step is repeated 17 times to get DPPC large uni-lamellar vesicles (LUVs).

The LUV samples are used not longer than 1 h after preparation to avoid aggregation. The LUV solution and reference buffer solution are kept in vacuum for 15 min to remove any gas bubbles in the solution before being added into the calorimeter cells.

3.3 Methods

3.3.1 Electrophysiology

As it is convenient and widely adopted to measure the electrical signal of a nerve impulse, electrophysiology is the main technique used in this thesis.

Intracellular recording: To obtain an accurate membrane potential, one could perform an intracellular recording by inserting a glass pipette with an electrode into the nerve, and measure the potential changes with respect to a grounded reference electrode in the extracellular solution. However, intracellular recording requires very precise micromanipulation, a special patch-clamp amplifier, and a single neuron preparation. Besides, it is difficult to perform

measurements on vertebrate nerve fibers and it does damage to the membrane close to the pipette tip. For all of these reasons, a less demanding technique in terms operation, instrumentation — extracellular recording, was used in the experiments.

Extracellular recording: Extracellular recording measures the potential changes at the membrane surface rather than the potential across the membrane. In our setup, two recording electrodes are put in close proximity to the nerve membrane, and they are connected to a differential amplifier to measure the potential difference between them. The setup mostly used is Powerlab 26T (ADInstruments, Australia), an integrated data acquisition system with built-in function generator. Differential voltage output is given out with three electrodes, positive, negative and ground, which could be separated by a T-shape connector into two sets of stimulation signals of exactly the same voltage difference. In this way, two points on the nerve could be stimulated at the same time with the same voltage, as was done in the collision experiments. The data acqusition system used in the heat measurement and magnetic field measurement will be described in detail later in the correspondent chapters.

3.3.2 Differential Scanning Calorimetry (DSC)

Differential Scanning Calorimeter is a widely used calorimetric technique to obtain thermodynamical information from small amount of materials. There are two cells in a calorimeter, a sample cell and a reference cell. The calorimeter measures the difference of heat needed to increase the temperature of the two cells by the same degree, or the difference of heat released to decrease the temperature of the two cells by the same value. In the work presented here, the sample is DPPC/DPPC lidocaine in buffer solution, and the reference is the buffer solution.

There are two types of DSC instrument, namely heat flux DSC and power compensation DSC. In heat flux DSC, there is only one furnace heating both cells. The primary signal measured is the temperature difference between the sample and the reference. When there is a heat-consuming process in the sample, its temperature will be lower than the temperature of reference, and heat flow is then calculated from the temperature difference.

In the work presented here, a VP DSC from MicroCal (USA) was used, which is a power compensation DSC. A schematic illustration is shown in Fig. 3.2. The reference and sample cell are housed within an insulating jacket. The device is designed to always maintain these two cells at the same temperature. During a measurement, the reference and sample cells are heated at a constant preset scan rate. As the lipid sample goes through a phase transition, heat is absorbed or released, creating a temperature difference (ΔT) between the sample and the reference cell. This results in a thermal gradient across Peltier units that sets up a proportional voltage which in turn is converted to power to form a feedback

loop to the heaters to return DT (the temperature differential) to zero.

$$\Delta P = P_s - P_r \neq 0 \tag{3.1}$$

The excess heat ΔQ added to the sample can then be calculated by integrating the excess power over heating time, Δt,

$$\Delta Q = \int_t^{t+\Delta t} \Delta P(t')dt' \cong \Delta P \cdot \Delta t \tag{3.2}$$

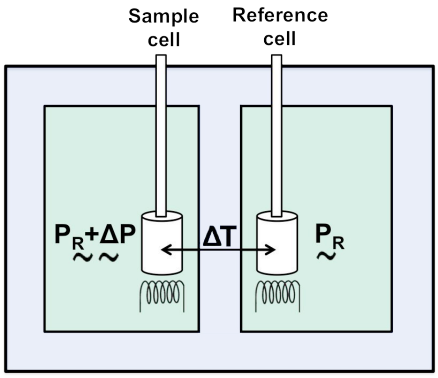

Figure 3.2: Schematic drawing of heat compensation DSC

Since the cells are kept at constant pressure, i.e. $\Delta p = 0$, the heat capacity Δc_p at constant pressure can be derived as follows:

$$\Delta c_p = \left(\frac{dQ}{dT}\right)_P \cong \left(\frac{\Delta Q}{\Delta T}\right)_P = \frac{\Delta P}{\Delta T/\Delta t} \tag{3.3}$$

where $\Delta T/\Delta t$ is the preset scan rate. Thus, the excess heat capacity as a function of temperature can be obtained by dividing the compensated power of the calorimeter by the scan rate. From the heat capacity profile, the enthalpy and entropy change during phase transition could be obtained by integration. Taking the melting process as an example:

$$\Delta H_0 = \int_{T_g}^{T_f} \Delta c_p dT \tag{3.4}$$

$$\Delta S_0 = \int_{T_g}^{T_f} \frac{\Delta c_p}{T} dT = \frac{\Delta H_0}{T_m} \tag{3.5}$$

where T_g is a temperature below the melting transition, i.e. gel phase; and T_f is a temperature above the melting transition, i.e. fluid phase.

3.3.3 Thermocouple and Thermopiles

Thermoelectric effect In 1821, German physicist Thomas Johann Seebeck found that a circuit made of two dissimilar metals, with junctions held at different temperatures would deflect a compass magnet. It was later realized that

an electrical current was induced by a "thermoelectric force", and deflected the magnet. The temperature difference produces an electromotive force (emf) in a closed circuit, known as the "Seebeck effect". The opposite process is called "Peltier effect". It describes that an electrical current would generate heating or cooling at the junction of two dissimilar metals, which has been widely applied in refrigeration industry. The Seebeck effect and Peltier effect were later related through thermodynamics and "Thomson effect"was predicted. Heat is absorbed or produced when current flows in a material with a temperature gradient. Seebeck effect, Peltier effect and Thomson effect are known as three thermoelectric effects, which directly convert temperature difference to electric voltage and vice versa. The Seebeck effect is the basis of thermocouples.

Thermocouple From Seebeck effect, we know that when two dissimilar metal wires join at both ends and one of the ends is heated, there is a continuous current flowing in the thermoelectric circuit. If there is only one joint and the other is an open circuit, there will be an open circuit voltage at the end. The voltage gradient (∇V) is proportional to the gradient in temperature (∇T)

$$\nabla V = -S(T)\nabla T \tag{3.6}$$

$S(T)$ is a temperature-dependent property of materials, which is called Seebeck coefficient. Fig. 3.3 is a T-type thermocouple made of copper (S_+) and constantan (S_-) in the standard measurement configuration. In the configuration, there are

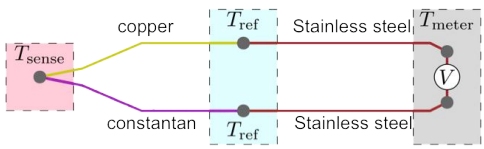

Figure 3.3: T-type thermocouple (copper-constantan) in the standard thermocouple measurement configuration. $\mathrm{T_{sense}}$ is the temperature at the joint, i. e. the temperature to be measured; $\mathrm{T_{ref}}$ is the reference junction that are put into a medium with a well defined known temperature; and $\mathrm{T_{meter}}$ is the temperature at the connections with the volt meter.

four regions with temperature gradient:

1. Change from $\mathrm{T_{meter}}$ to $\mathrm{T_{ref}}$ in the lower stainless steel wire, $V_1 = \int_{T_{meter}}^{T_{ref}} (-S_{SS}(T))dT$;
2. Change from $\mathrm{T_{ref}}$ to $\mathrm{T_{sense}}$ in the constantan wire, $V_2 = \int_{T_{ref}}^{T_{sense}} (-S_-(T))dT$;
3. Change from $\mathrm{T_{sense}}$ to $\mathrm{T_{ref}}$ in the copper wire, $V_3 = \int_{T_{sense}}^{T_{ref}} (-S_+(T))dT$;
4. Change from $\mathrm{T_{ref}}$ to $\mathrm{T_{meter}}$ in the upper stainless stell wire, $V_4 = \int_{T_{ref}}^{T_{meter}} (-S_{SS}(T))dT$.

$V_1 = -V_4$, which cancel each other. Thus the measured voltage is

$$V = \int_{T_{ref}}^{T_{sense}} (S_+(T) - S_-(T))dT \tag{3.7}$$

In the experiments of BR reaction, a T-type thermocouple coated with stainless steel was used for measurements, ice water bath was used for reference as a natural thermostat with a fixed temperature of 0 ℃.

Thermopile A thermocouple has a limited sensitivity of about tens of micro

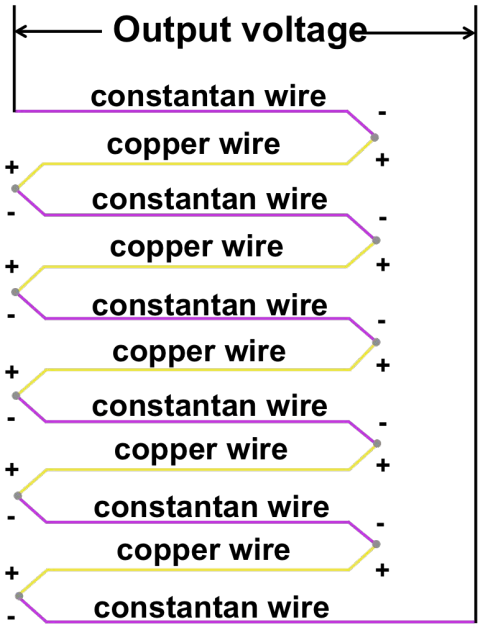

Figure 3.4: Thermopile made of five pairs of T-type thermocouples.

volts per degree, and thus it has limited application for measurements of small temperature change. But by putting a certain number of thermocouples in series, forming a thermopile, the sensitivity will be increased by several folds.

Fig. 3.4 shows a thermopile made of five pairs of T-type thermocouples. There are two contact lines with junctions. The temperature difference between the two lines is measured. One of the lines should be placed where the temperature to be measured, and the other at the reference. A temperature gradient will form in each of the wires if the two lines are at different temperatures, and thus a voltage gradient is present in each wires. It resembles a series circuit where the total voltage is the sum of each individual voltages. Therefore, the sensitivity adds up. The sensitivity of a T-type thermocouple is 43 µV/℃, thus the sensitivity of the thermoplie is $5 \cdot 43$ µV/℃=215 µV/℃.

3.3.4 Voltammetry

Electrochemical Cell A reduction-oxidation (redox) reaction is a chemical reaction which involves changes of the oxidation state of atoms. It consists of a reduction process in which the atom involved gain electrons, and an oxidation process in which the atom loses electrons. A non-spontaneous redox can be driven by electrolysis. A typical electrolytic configuration comprises an external battery,

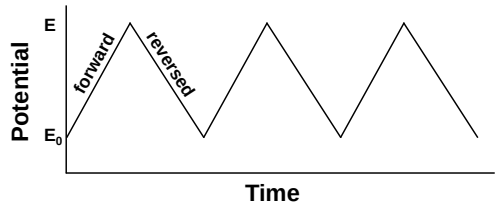

Figure 3.5: A typical potential ramp in a cyclic voltammetry measurement. The potential starts from a vaule of E_0, and increases linearly to a set value E. It then goes back linearly to the initial value. This cycle is typically repeated several times.

(at least) two electrodes and electrolytes. The battery provides an external field, which drives the flow of the electrons. As a result, at one electrode (cathode), electroactive species in the solution gain electrons and reduction reaction happens on the interface of the electrode and the solution. At the other electrode (anode), the active species in the solution lose electrons and oxidation reaction happens. The electrode potential changes due to redox reactions, which is related to the concentration of active species through the Nernst equation:

$$E = E^0 + \frac{2.3RT}{nF} log \frac{C_O(0,t)}{C_R(0,t)} \tag{3.8}$$

where E is the electrode potential, E^0 is the standard potential for the redox reaction, R is the gas constant, T is temperature, n is the number of moles of electrons transferred in the reaction, F is the Faraday constant, $C_O(0,t)$ is the concentration of the active speices in the oxidized form and $C_R(0,t)$ is the concentration of the active species in the reduction form. Thus the concentration of electroactive species in the solution can be determined by an electrochemical cell.

A typical electrochemical cell in experiments consists of a working electrode, a reference electrode and an auxiliary electrode (also called counter electrode). The reaction of interest happens on the working electrode, and the released electrons flow to the auxiliary electrode, thereby forming a electron circuit. Additionally, the electrode potential at the working electrode, referring to the reference electrode, is measured.

Cyclic Voltammetry The electrochemical properties of a species can be determined by cyclic voltammetry. In a cyclic voltammetry experiments, the working electrode is typically ramped linearly versus time in opposite directions. A typical cycle of potential change as a function of time is shown in Fig. 3.5. The current response on the working electrode is monitored. When there a reduction/oxidation process happens at the working electrode, electrons are gained/released from the concerned species, and thus there will be a pronounced change in the current which displays as a peak. In a reversible redox process, the peaks on a forward ramp and a reversed ramp have opposite signs, but appears at the same potential relative to the starting value (E_0 in forward

ramp, and E in th revesed ramp) in the recorded cyclic voltammogram traces. The shapes of the voltammetric traces and their unique potential positions are fingerprints for the corresponding electrochemical process, in analogous to a conventional spectrum.

Constant-potential (potentiostatic) method Once the characteristic potential for an electroactive species is determined from the cyclic voltammetry experiments, the potential of the working electrode can be fixed at this value to drive a certain electron-transfer reaction. The resulting current measured in this case is proportional to the concentration of the species under study.

Chapter 4

Penetration of Action Potentials Upon Collision in Invertebrate Nerves

4.1 Background

When a neuron is stimulated close to the cell body, an action potential is initiated and propagates down the axon. When a nerve impulse is generated at other positions on the axon, it travels in two opposite directions: orthodromic conduction toward the axon terminal; and antidromic conduction toward the cell body. If

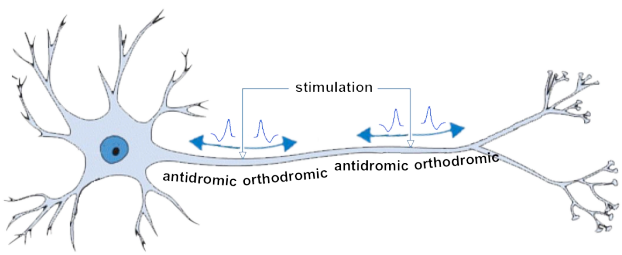

Figure 4.1: Schematic illustration of orthodromic and antidromic action potential.

two sites on the axon are stimulated simultaneously, there are four action potentials in total initiated in different directions, two of which will meet each other in the middle and collide. Based on the HH model, a refractory period follows an action potential because of the inactivation of the voltage-gated sodium channels that depolarize the axon membrane for a few milliseconds. During the refractory period, the neuron becomes inexcitable and unable to generate a new action potential. Therefore, the two action potentials should annihilate after collision as the membrane left behind by the other impulse is in the refractory period.

However, in the Soliton model, nerve impulses are considered as electromechanical density pulses, similar as solitons. During the collision of solitons, the solution cannot be represented as a linear combination of two solitons, but they can restore their shapes after collision possibly with a phase shift. In the work presented by Gonzalez-Perez et al. [69], the equation for soliton propagation in 1D biomembrane cylinder was solved numerically. Fig. 4.2 shows the calculated results.

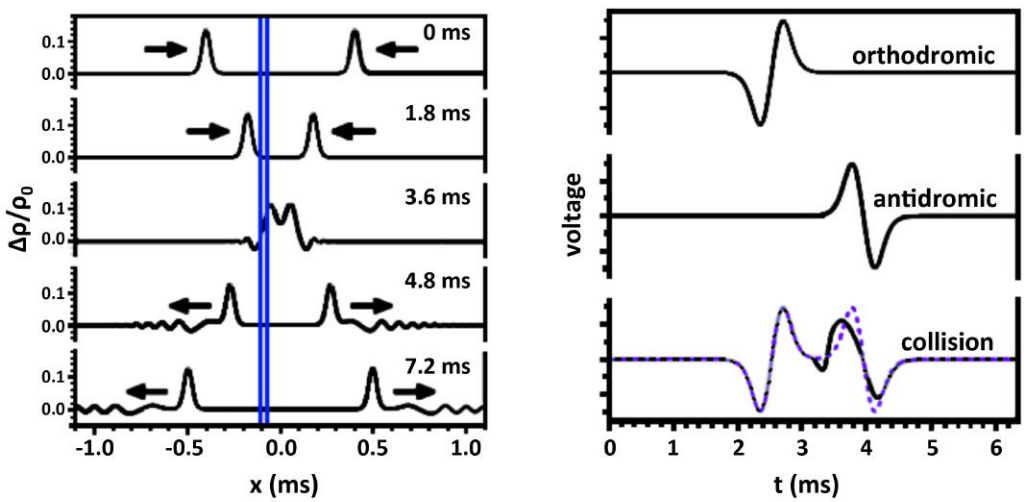

Figure 4.2: The left panel shows the collision of two impulses in the soliton theory of nerves ($v = 0.7c_0$). Two blue lines represent the position of two hypothetical recording electrodes separated by a distance of 16 mm. The right panel shows the calculated voltage difference between the two electrodes. The traces show (top) the single orthodromic action potential (AP), (center) the antidromic AP, (bottom) solid: the recording of the two colliding pulses; dashed blue: the sum of the orthodromic and antidromic without a collision. Figures taken from [69].

The left panel shows the pulses before and after collision at five different times t. The shape, velocity, and energy of the pulses are almost unchanged. One finds a broadened intermediate collision state, which is wider than the individual solitary waves. Therefore based on soliton model, two nerve pulses traveling in opposite direction colliding with each other can penetrate through each other and continue propagating with almost unchanged properties.

Tasaki [75] studied the collision of two nerve impulses in motor nerve fibers innervating the sartorius muscle of the toad and concluded that the two impulses annihilate with each other upon collision. However he argued that the blockage of impulses are not a result of refractoriness left behind by the other impulse, but because of a lack of internal stimulating current by which the normal transmission is effected. Limited work has been done to confirm or to reject this finding since Tasaki's work. Instead, annihilation after collision of two impulses has been generally believed and used in some other experiments, e.g. to identify axonal

destinations of single cells in the central nervous system.

Since different opinions exist with respect to what would happen after two nerve impulses colliding with each other, it is important to investigate whether they annihilate or pass through each other. Gonzalez-Perez et al. [69] performed experiments on two invertebrate nerves, the abdominal ventral cord of lobster *Homarus americanus*, and the ventral cord extracted from earthworm *Lumbricus terrestris*. They showed that collision of two nerve impulses generated simultaneously on two sides of the nerve traveling toward each other did not result in mutual annihilation. Instead, they penetrated through each other and continued propagating with their shape and velocity almost unchanged.

However, Berg et al. [76] questioned the work by Gonzalez-Perez et al. [69] with the following arguments:

1) In the experiments, nerves are sitting in the air on the chamber instead of in a physiological condition, which might affect the results;

2) The nerves used in their experiments are not pure axons, but rather interrupted by ganglia which might have signal processing effect resulting in generation of action potentials in new axons.

Berg et al. then performed experiments on nerve bundles from walking legs of lobsters and sciatic nerves from frogs which contain bundles of axons without interruption of ganglia. Based on the results, they concluded that two impulses annihilated upon collision. However, it shall be noted that they used a different configuration of electrodes. The configuration of the electrodes used by Berg et al. is compared with that used by Gonzalez-Perez et al. in Fig. 4.3.

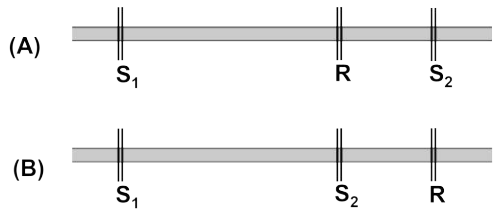

Figure 4.3: (A) Electrode configuration adopted by Gonzalez-Perez et al. Stimulation electrodes are denoted as S_1, S_2, and recording electrodes are denoted as R. Stimulation electrodes are placed on the two ends of the nerve, recording electrodes are in between two stimulations but close to one side. (B) Electrode configuration adopted by Berg et al. Stimulation electrodes are placed on the same side of the nerve, recording electrodes are at one end of the nerve.

To investigate the arguments and discrepancies discussed above, the collision of two nerve impulses traveling in opposite directions is further studied in this chapter. The work in this chapter is designed as follows:

1) Abdominal ventral cord from lobsters, a similar preparation as Gonzalez-Perez et al. adopted, is used in the first part. The difference is that the nerve will be in a physiological saline solution during measurements. The purpose is to

study the impact of nerve exposure during the collision experiments, i.e. in air or in a physiological condition, on the experimental results;

2) Nerve bundles from walking legs of lobsters, a similar preparation as Berg et al. adopted, is used in the second part. The goal is to study whether the presence of ganglia will impact the results of the collision experiments. Both electrode configurations shown in Fig. 4.3 are examined.

4.2 Abdominal Ventral Cord of Lobsters in Liquid Chamber

One of the samples Gonzalez-Perez et al. used is the abdominal ventral cord from lobster tails which contains six ganglia and four giant axons. Two median giant axons run all the way through the abdominal ventral cord as single neurons, while two lateral giant axons are connected at each ganglion, and extend over six neurons [77]. A schematic illustration of the nerve and the anatomy is shown shown in Fig. 4.4 (a) (c).

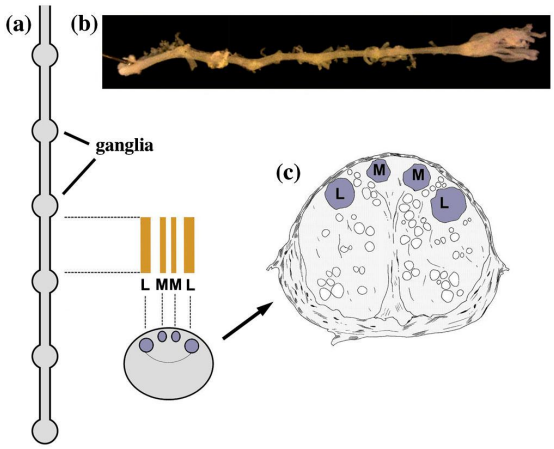

Figure 4.4: (a) Schematic illustration of a lobster ventral cord at the abdominal site with six ganglia, (b) a photo of abdominal ventral cord extracted from the lobster tail, (c) anatomy of four giant axons in the ventral cord. Figure taken from [69].

In the experiments presented in this chapter, all the roots coming out of ganglia are cut so that the diameter of the nerve fits the glass capillary in the liquid chamber where the nerve and saline solution sit. Besides, the signal becomes cleaner after cutting the roots as they generate some weak spontaneous spikes.

4.2.1 Liquid Chamber

The chamber used in the work of this part consists of a plastic base with electrical connections, a glass capillary surrounded by gold electrodes at different intervals and a plastic back with syringe connections to change solutions in the capillary

as shown in Fig. 4.5. The nerve was tied with thread on both sides. One of

Figure 4.5: A picture of the liquid chamber. On the back are the tubes for injection of solutions, with switches numbered as 1, 2, 3 to control the flow; the glass capillary into which the nerve goes is the transparent cylinder on the base with gold electrodes inside at different positions. The holes in the front are for electrical connections.

the threads was connected to a thin copper wire which leads the nerve into the glass capillary. Saline solution was injected with a syringe from the holes on the top that were connected to the capillary through tubes. Once the nerve was in the capillary, it gently touched the surrounding gold electrodes, resulting in good connections between the nerve and electrodes. Stimulation of the axon was led off through two pairs of electrodes at the two ends of the nerve. The nerve could be stimulated simultaneously from both sides. A pair of recording electrodes were located close to the orthodromic stimulation side.

Experiments were conducted in a way that the nerve was first stimulated separately from each end at the same stimulation voltage, and the action potentials were recorded respectively. It was subsequently stimulated simultaneously from both ends. In this case, the orthodromic impulse first reached the recording electrodes, and thus the orthodromic signal was first recorded. The orthodromic impulse then met the antidromic impulse close to the middle of the nerve and they collided with each other. If they annihilated, the signal recorded would only consist of the orthodromic impulse. On the other hand, however, if they penetrated each other, the antidromic signal would meet the recording electrodes later, and thus both orthodromic and antidromic impulse would be recorded. The above procedures were repeated at different stimulation voltages. The amplitude of stimulation voltage was increased step by step to excite more neurons until all the giant axons were active.

4.2.2 Results and Discussions

Typical results for this part of experiments are presented in Fig. 4.6. From the left to the right of the figure, the results are for three different stimulation

voltages. As described above, at each stimulation voltage, the orthodromic and antidromic impulses are recorded separately; the nerve is then stimulated at both ends simultaneously and the signals are recorded. The results for the orthodromic, antidromic and collision are shown in the upper, middle and lower traces respectively.

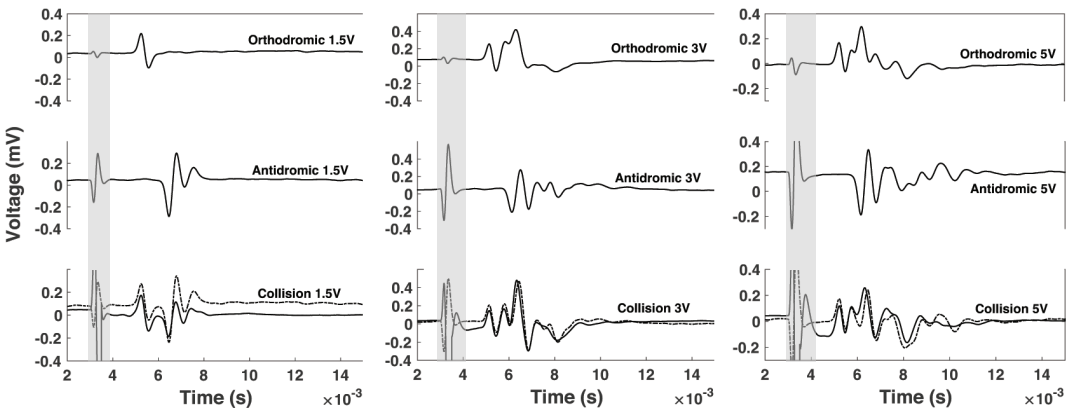

Figure 4.6: Collision experiments on abdominal ventral cord from lobster with increasing stimulation voltages. The upper traces are impulses initiated at a site close to thorax (orthodromic); the middle traces are impulses initiated close to tail (antidromic); and the solid lower traces are signals recorded when the nerve was stimulated at both ends (collision), dashed lines are the sum of the two traces above added for comparison with the measured one.

The peaks in the marked grey areas are stimulation artifacts. As can be seen from the figure, when the stimulation voltage is increased, more peaks are generated in both directions. Furthermore, the measured collision signals are almost identical to the sum of orthodromic and antidromic signal at all stimulation voltages. Based on the results, we conclude that the impulses generated and propagating from two sides penetrated each other instead of annihilating.

In addition, the results obtained in this work are consistent with those presented by Gonzalez-Perez et al. in [69]. It is then concluded that the chamber Gonzalez-Perez et al. used without saline solutions does not make a difference on the results of collision experiments.

4.3 Axon Bundle From Lobster Walking Legs

Similar collision experiments were performed on peripheral nerves from lobster walking legs, which contain bundles of non-interrupted axons. Numerous axons are inside the bundle, resulting in a compound action potential in the measurements. Since we have demonstrated in Sec. 4.2 that two kinds of chambers do not make a difference on the results in the collision experiments, the chamber adopted by Gonzalez-Perez et al. is used in this part as it fits the size of nerve

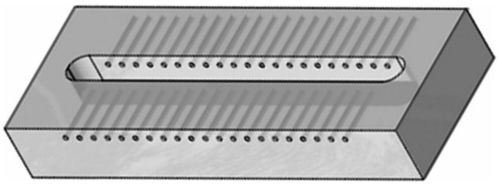

Figure 4.7: The design of nerve chamber. The holes on the two sides of the chamber have a size of 0.5 mm diameter for holding the stainless steel electrodes. The nerve sits on the electrodes. A certain amount of saline solutions is added into the groove in the middle without touching the electrodes. The chamber is then covered by a cover slip so that a saturated of water vapor is kept during the measurements to keep the nerve from drying. The distance between two electrodes is 2.5 mm. The chamber is made of Lucite. Figure taken from [69].

bundles from lobster walking legs and is less time-consuming. The design of the chamber can be found in Fig. 4.7.

Typical results are shown in Fig. 4.8. Collision experiments were performed in the same manner as described Sec. 4.2, as well as the data analysis. With

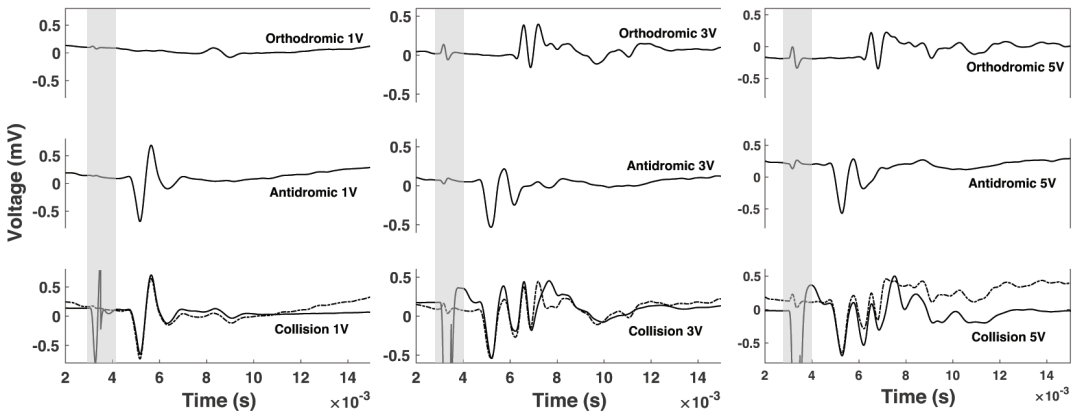

Figure 4.8: Collision experiments on nerve bundles from lobster legs with increasing stimulation voltages. The upper traces are impulses initiated at a site close to the body (orthodromic); the middle ones are impulses initiated close to the claw (antidromic); and the lower solid traces are signals recorded when the nerve was stimulated at both ends (collision). The dashed line is the sum of the above two traces added for comparison with the measured one. The electrode configuration is like the one in Fig. 4.3 (a).

the increase of the stimulation voltages, more peaks show up in both directions. After 3V stimulation, the number of peaks doesn't change much, indicating that all the axons in the bundle are excited. It can be seen from the figure that at all stimulation voltages, all the peaks from both sides are present in the collision traces, proving the penetration of impulses traveling from different sides. There can be found some shifting of peaks, which is consistent with the prediction of Soliton theory.

The experiments in [76] on peripheral nerves from lobster legs and frog sciatic nerves were done with a different electrode configuration, as shown in Fig. 4.3 (B). Two pairs of stimulation electrodes were on the same side of the recording electrodes with different distances, which was also tested in our experiments.

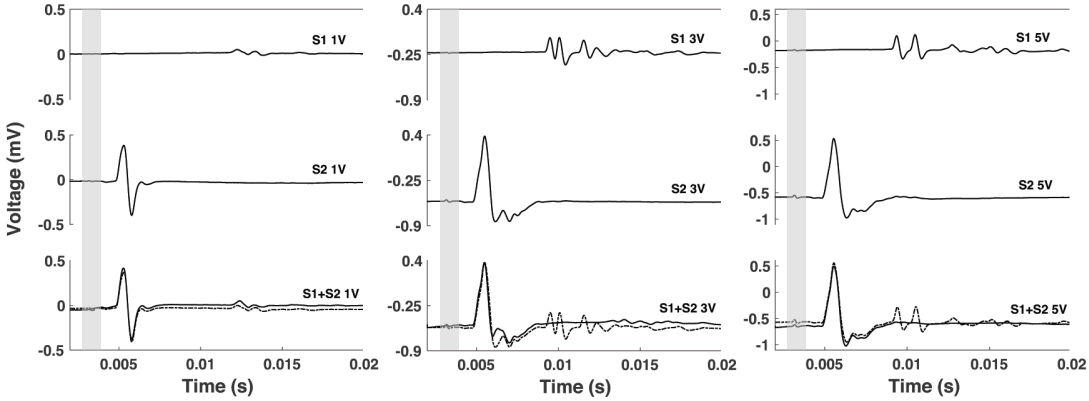

Figure 4.9: Collision experiments on nerve bundles from lobster legs with increasing stimulation voltages. The upper traces are impulses initiated at a site close to body (orthodromic); the middle ones are impulses initiated close to claw (antidromic); and the lower solid ones are signals recorded when the nerve was stimulated at both ends (collision). The dashed line is the sum of the two traces above added for comparison with the measured trace. The electrode configuration is like the one in Fig. 4.3

Typical results are shown in Fig. 4.9. The stimulation electrodes far away from recording electrodes are denoted as S_1, the closer pair is denoted as S_2. The bundle of axons is first stimulated with S_1 and S_2 respectively, followed by simultaneous stimulation from S_1 and S_2. Stimulation voltage is increased step by step. After the stimulation voltage reaches 3 V, the peaks don't change much from both directions, indicating that all the axons are firing. With this configuration of electrodes, similar results as Berg et al. reported are obtained. Only the action potential from the nearer stimulation (S_2) is found when both parts of nerves are stimulated at higher voltages. At lower voltage (1 V in Fig. 4.9), the signal from the stimulation far away is also recorded when both positions are stimulated simultaneously. This means that,
1) we handle our nerve samples properly;
2) we operate correctly in our experiments;
3) the experiments with two electrode configurations do not measure the same phenomenon.
We speculate that the nerve is highly perturbed after a stimulation which suppresses another action potential at the same site for a certain period of time. The nerve impulses did pass through each other upon collision, however, signal from S_1 could not be detected as it could not reach the recording electrodes.

To confirm our speculation, we did further experiments with two pairs of recording electrodes, recording simultaneously in the middle of two stimulations

(R_1) and at the end of the nerve (R_2), as shown in Fig. 4.10. It is a combination of the two configurations in Fig. 4.3. Fig. 4.11a shows the results from recording

Figure 4.10: Electrode configuration with two pairs of recording electrodes. R_1 is placed in the middle of two stimulations; R_2 is placed at the end of the nerve.

electrodes R_1 and Fig. 4.11b shows the results from recording electrodes R_2.

At both recordings, more peaks show up as the stimulation voltage is increased. The signal from stimulation S_1 is significantly far away from R_2, so that the peaks are better separated and have smaller amplitudes due to velocity differences in different axons. The signal recorded with simultaneous stimulation from both sides (S_1+S_2) are almost identical to the sum of each individual signals at the recording in the middle (R_1); while in the recording at one end (R_2), only the signal from the closer stimulation shows up at higher voltages. This is consistent with our expectation, as the results at recordings R_1 and R_2 are consistent with each individual measurements. It indicates that the fact that the signal from S_1 cannot be recorded at R_2 is not due to annihilation, but more likely that the membranes are much perturbed by stimulation S_2 with high voltages.

4.4 Perturbation Tests on Nerves

To further support our argument with respect to perturbation in Sec. 4.3, the refractory period was tested with the electrode configuration shown in Fig. 4.12. Recording electrodes R were placed at one end of the nerve, the first pair of stimulation electrodes S_1 was far away from the recording R, and another pair of stimulation electrodes S_2 was close to the recording R.

In the experiments, the starting time at which two stimulations were sent out were adjusted so that two situations were achieved (the nerve impulses initiated at S_1 is denoted as P_1, and the nerve impulse initiated at S_2 is denoted as P_2):

1) A stimulation S_1 was sent out so that P1 could pass the position of S_2 first, followed by a stimulation S_2. Due to the refractory period P_1 left at the position of S_2, a nerve impulse P_2 cannot be initiated within a certain period of time. The time interval of the two stimulations were later increased until the signals from both stimulations (P_1 and P_2) could be recorded.

2) A stimulation S_2 was sent out first, so that P_2 was initiated first. Followed by P_1 passing the position of S_2. Due to the refractory period left by S_2 and P_2, a nerve impulse P_1 cannot pass the position S_2 and thus cannot be detected within a certain period of time. The time interval of two stimulations were later increased until the signals from both stimulations could be recorded.

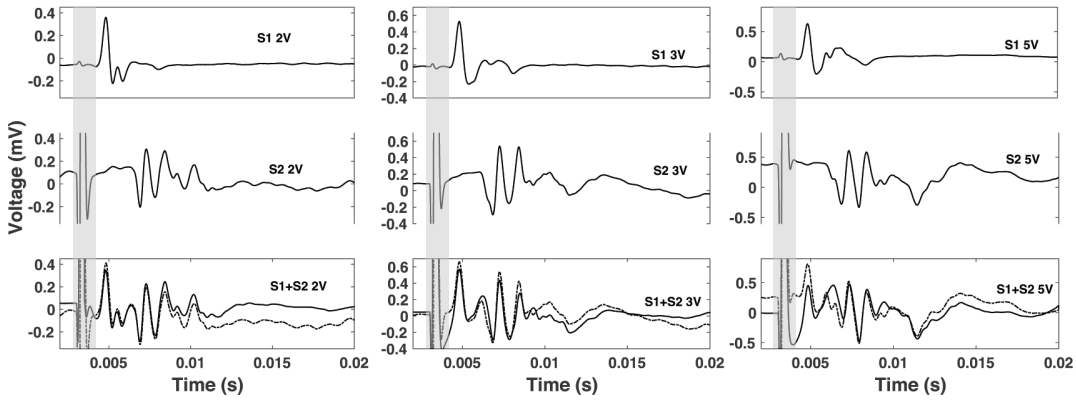

(a) Recording at R1

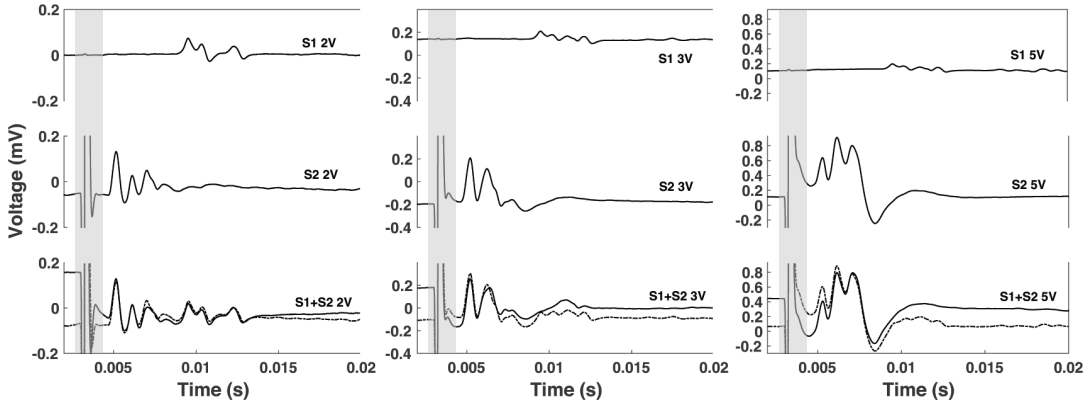

(b) Recording at R2

Figure 4.11: Collision experiments on nerve bundles from lobster legs with two pairs of recording electrodes. The upper traces are impulses initiated at S_1; the middle ones are impulses initiated at S_2; and the lower ones are signals recorded when the nerve was simultaneously stimulated at S_1 and S_2. The dashed lines are the sum of the two traces above added for comparison with the measured trace.

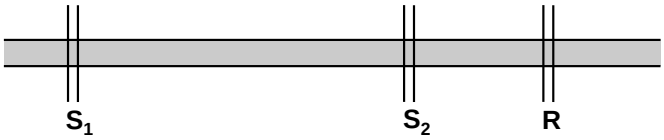

Figure 4.12: Electrode configuration in refractory period tests. Stimulation electrodes R_1 are placed close to one end of the nerve, far away from the recording electrodes R; another pair of stimulation electrodes R_2 are placed close the recording electrodes R.

As this test requires that individual peaks can be well identified from the recorded signals, a preparation with less axons was adopted with the purpose to obtain cleaner signals: the ventral cord from the earthworm *Lumbricus terrestris*. The anatomy of earthworm ventral cord is shown in Fig. 4.13. There are in total

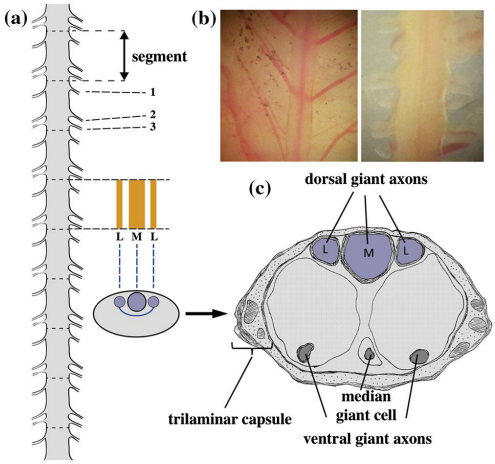

Figure 4.13: Schematic drawing of the anatomy of an earthworm ventral cord. (a) schematic representation of an earthworm ventral cord with the segments. (b) pictures during dissection showing the ventral cord attached to muscular tissues (left) and completely isolated. (c) internal anatomy showing the distribution of axons, Median and lateral giant fibers are marked with M and L. Figure adapted from [69].

three giant axons on the dorsal side of the ventral cord. One of them is the median giant axon, and the other two are lateral giant axons with a slightly smaller diameter and connected to each other at each ganglia. A typical signal from this preparation contains only one peak at lower stimulation voltage corresponding to the signal from the median giant axon; and two peaks at higher stimulation voltages, with the first from the median giant axon and the second from two lateral giant axons.

Fig. 4.14 shows the results, in which the signals were initiated at high stimulation voltage to excite all the giant axons. Two peaks were present in each measurements. As can be seen in Fig. 4.14 (a), both peaks from S_2 arrived earlier at the recording electrodes (middle trace) compared to the corresponding peaks from S_1 (the upper trace), indicating that signals from S_1 arrived at the position of S_2 after an impulse was generated by S_2. When the two stimulations were sent

out successively at this time interval, only the peaks from S_2 could be detected. This means that the nerve at the position of S_2 was left in a refractory period when the impulse from S_1 arrived, so that the signal from S_1 could not pass that area.

The time interval between S_2 and S_1 was subsequently increased until both signals could be detected (data not shown here). Fig. 4.14 (b) shows the condition right before this point. If we look at the first peak and read out the time points corresponding to the peak values, and do a subtraction between the two values obtained from the upper trace and the middle, we could get the time interval between the arrival of the signals from two stimulations at S_2. It was calculated to be $\Delta t = 3.6$ ms, which means that the nerve was left in a refractory period $\tau \geq 3.6$ ms after a high voltage stimulation.

The time interval between two stimulations were then adjusted to allow the signal from S_1 to pass the position of S_2 first, and then S_2 was sent out. In Fig. 4.14 (c), it can be seen that peaks from S_1 (upper trace) arrived the recording electrodes earlier than that from S_2 (middle trace), indicating that a stimulation S_2 was generated after the signal from S_1 passed. The time interval of two stimulations was then increased so that all the peaks from both stimulations were recorded, as shown in Fig. 4.14 (d). This means that the nerve has recovered from the refractory state.

We do the same subtraction for the time of the first peak and get a $\Delta t' = 2.8$ ms. Therefore, the refractory period after a nerve impulse passes should be $\tau' \leq 2.8$ ms.

Comparing the two values of refractory period τ and τ', one finds that $\tau > \tau'$. This represents that the refractory period after a high voltage stimulation is significantly longer than that after a nerve impulse passes, which confirms our argument that the membranes of the nerve is largely perturbed after a high voltage stimulation.

4.5 Summary

To further investigate the collision of two nerve impulses traveling in opposite directions, experiments were performed on two preparations: abdominal ventral cord from lobsters, and nerve bundles from lobster walking legs. Main conclusions are summarized as follows:

1) The results on abdominal ventral cord with nerves in physiological solutions during the collision experiments are consistent with that obtained with a simple chamber without sufficient amount of solutions during the experiments as reported by Gonzalez-Perez et al. [69]. It is concluded that the two types of nerve chambers would have limited impact on the experimental outcome.

2) For the nerve bundles without interruption of ganglia, different electrode configurations were studied and it is concluded that impulses penetrated through

each other on pure axons upon collision but they cannot pass a largely perturbed region from high voltage stimulation. This is supported by the finding on a ventral cord from earthworm that the refractory period for the area after high voltage stimulation is significantly longer than that for an area where the nerve impulse passes.

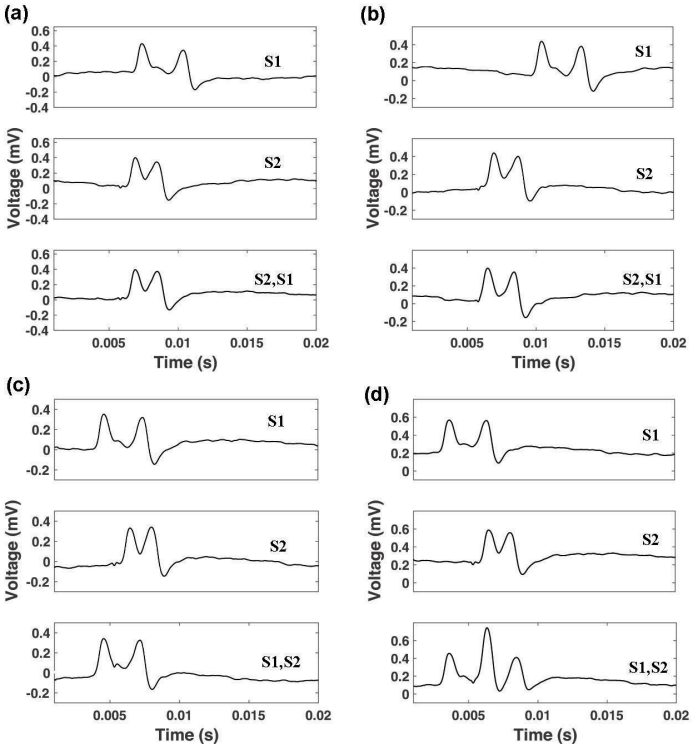

Figure 4.14: The recordings in the perturbation tests. There are two impulses initiated at both stimulations. The upper traces are from stimulation S_1 only, the middle traces are from simulation S_2 only, the lower trace is recorded when the two stimulation sent out in sequence with adjusted time intervals. (a) For both peaks, those initiated at S_2 arrived at the recording electrodes first, those from S_1 arrived later. In this case only the signals from S_2 could be recorded when both stimulations were sent out with this particular time interval. (b) This case is similar with (a), but with a larger separation between S_1 and S_2. Only impulses initiated at S_2 could be recorded. (c) For both peaks, those initiated at S_1 arrived at the recording electrodes first, those from S_2 arrived later. In this case only the signals from S_1 could be recorded when both stimulations were sent out with this particular time interval. (d) The time interval in (c) was increased so that S_2 started after the refractory period of the impulses initiated at S_1. As a result, all the peaks from S_1 and S_2 could be recorded.

Chapter 5

Heat Change During Adiabatic Processes

5.1 Background

The heat change during a nerve impulse has been reported to contain two phases, an initial heat release followed by a reabsorption of all the heat released [78, 79, 48]. This process is in phase with the action potential [48]. This heat change may originate from three possible sources [80]:
1) the flow of ions from one biological compartment to another during the spike;
2) the free energy changes that follow the discharging and charging of a condenser;
3) the entropy changes over the process of the action potential.

The flow of ions cannot account for the heat change observed in experiments for the following reason. The cation fluxes in the garfish olfactory nerve fibers were measured to be 33 nmole/g at 0 ℃ for potassium efflux [81]. The positive heat released by such a nerve was found to be 44.2 µcal/g, corresponding to the heat production of 1340 cal/mole cation flux. This value is several orders of magnitude larger than the heat from mixing of potassium chloride with sodium chloride. Therefore, it is unlikely that the heat change during the action potential can be attributed to the mixing of cations [47].

Continuing with the condenser theory, the nerve membrane consists of a membrane capacitor in the equivalent circuit, which is charged at rest. A charged membrane capacitor stores free energy. Upon discharging the membrane (depolarization), this free energy would be released as heat resulting in a local heating of the medium. During the repolarization process, free energy is stored in the membrane capacitor again. If this energy comes from the ions in solution, there would be a corresponding cooling of the medium. Therefore, it will display a heat change of two phases, an initial heat production, followed by a local cooling, and the timing should be in phase of the action potential. The amount of heat released by discharging the membrane is equal to the total capacitive energy given

by $\Delta G = \int \frac{1}{2} C_m V^2 dA$. Keynes and Ritchie calculated the value for Mammalian C fibers and found that the heat release due to discharging the membrane capacitor is an order of magnitude smaller than what was measured in experiments [82]. It means that charging and discharging the membrane capacitor is not sufficient to account for the heat change during a nerve impulse either.

For these reasons, the heat change during a nerve impulse cannot be explained by the equivalent circuit based on which HH theory is built. It seems that the third source, entropy changes is very likely to account for it. The Soliton model considers the nerve impulse as solitary electromechanical pulse propagating in the nerve, which is an adiabatic (isentropic) reversible process. Another such example is the oscillation reactions like the iodine clock, which are found to oscillate in heat, as well as substances [83, 84]. The heat during such a reaction was found to oscillate for minutes [84], which consists of several adiabatic processes. These adiabatic reversible processes can be described by linear non-equilibrium thermodynamics, which will be introduced as follows.

5.1.1 Theory[1]

From the first law and the second law of thermodynamics, the change of the internal energy can be written as

$$dE = TdS - pdV + (-fdl - \Pi dA + \ldots) + \Psi_{el} dq + \sum_i \mu_i dn_i \tag{5.1}$$

solving for the entropy dS,

$$dS = \frac{1}{T} dE + \frac{p}{T} dV + \left(\frac{f}{T} dl + \frac{\Pi}{T} dA + \ldots \right) - \frac{\Psi_{el}}{T} dq + \ldots - \sum_i \frac{\mu_i}{T} dn_i \tag{5.2}$$

where dE, dV, dq, and dn_i are changes in extensive variables; $\underline{X_Q} = grad\left(\frac{1}{T}\right)$ is defined as the thermodynamic force related to heat Q, which leads to the flux of heat; in analogy, $\underline{X_{el}} = grad\left(-\frac{\Psi_{el}}{T}\right)$ is the thermodynamic force related to charges, which leads to the flux of electrons; $\underline{X_i} = grad\left(-\frac{\mu_i}{T}\right)$ is the thermodynamic force of particle species i which leads to the flux of particles.

Einstein proposed that the entropy can be considered as a potential [86]. Considering the entropy as a function of the extensive thermodynamic variables ξ_i, e.g. internal energy E, volume V, area A, charge q, the number of particles n_i etc, ξ_0 is the value of the variable in equilibrium, and the equilibrium entropy is S_0. In harmonic approximation, the entropy can be expanded as

$$S = S_0 + \sum_i \left(\frac{\partial S}{\partial \xi_i} \right)_0 (\xi_i - \xi_i^0) + \frac{1}{2} \sum_{ij} \left(\frac{\partial^2 S}{\partial \xi_i \partial \xi_j} \right)_0 (\xi_i - \xi_i^0)(\xi_j - \xi_j^0) + \ldots \tag{5.3}$$

[1]The theory summarized in this chapter is mainly based on the course handout of "Biophysics of biological non-equilibrium systems" and reference [85].

Since the entropy in equilibrium is in its maximum, the linear term can be omitted, so that

$$S - S_0 \approx \frac{1}{2}\sum_{ij}\left(\frac{\partial^2 S}{\partial\xi_i\partial\xi_j}\right)_0 (\xi_i - \xi_i^0)(\xi_j - \xi_j^0) \tag{5.4}$$

If coefficient g_{ij} is defined as $-g_{ij} = \left(\frac{\partial^2 S}{\partial\xi_i\partial\xi_j}\right)_0$, which represents a positive definite matrix with $g_{ij} = g_{ji}$, and $\alpha_i = (\xi_i - \xi_i^0)$. then Eq. 5.4 is turned into

$$S - S_0 \approx \frac{1}{2}\sum_{ij} g_{ij}\alpha_i\alpha_j \tag{5.5}$$

The entropy as a function of two variables in the harmonic approximation is shown in Fig. 5.1.

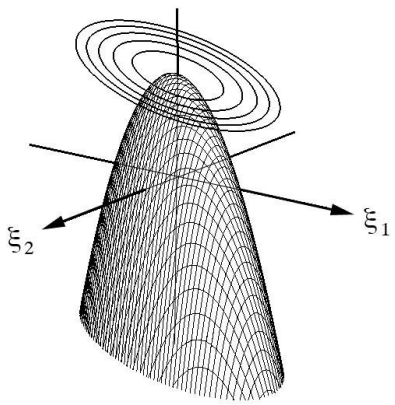

Figure 5.1: Entropy as a function of two variables, ξ_1 and ξ_2 in the harmonic approximation. Figure taken from [87].

If a thermodynamic system is out of the equilibrium, relaxation will drive the system back to more likely states with higher entropy. The entropy production can be written as a sum of the products of the thermodynamic forces with their conjugated fluxes

$$\sigma = \frac{dS}{dt} = \sum_i \underbrace{\frac{\partial S}{\partial\xi_i}}_{=X_i} \cdot \underbrace{\frac{\partial\xi_i}{\partial t}}_{=J_i} = \sum_{ij} X_i J_i \tag{5.6}$$

where X_i is a thermodynamic force, and J_i is the conjugated thermodynamic fluxes of the variable ξ_i.

In the linear approximation, the thermodynamic fluxes can be expanded as linear combinations of thermodynamic forces [88, 89]

$$\begin{aligned} J_1 &= L_{11}X_1 + L_{12}X_2 + \dots \\ J_2 &= L_{21}X_1 + L_{22}X_2 + \dots \\ J_3 &= \dots \end{aligned} \tag{5.7}$$

or $\underline{J} = \underline{\underline{L}}\,\underline{X}$. This set of equations are called phenomenological equations. Generally, the matrix $\underline{\underline{L}}$ can be written as the sum of a symmetric matrix ($\underline{\underline{L}}^S$) and an antisymmetric matrix ($\underline{\underline{L}}^A$)

$$\underline{\underline{L}} = \underline{\underline{L}}^S + \underline{\underline{L}}^A \tag{5.8}$$

The symmetric matrix ($\underline{\underline{L}}^S$) describes dissipative processes, as presented by Onsager [88, 89]; while the antisymmetric matrix ($\underline{\underline{L}}^A$) describes adiabatic and reversible processes. A real relaxation process with both dissipation and adiabatic processes is a combination of these two matrix, and can be interpreted as spiral trajectories in the entropy potential surface moving towards the equilibrium. These three processes are illustrated in Fig. 5.2 [85].

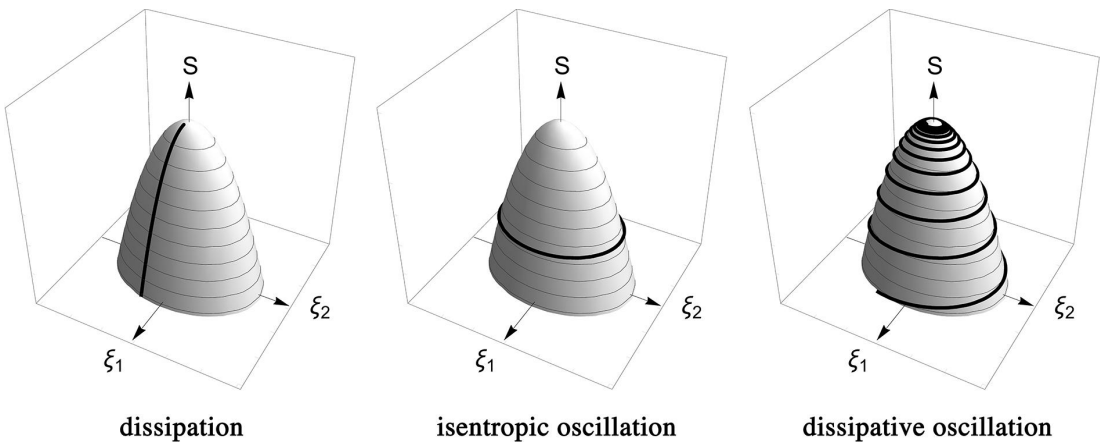

Figure 5.2: Schematic representation of dissipation, isentropic oscillations and real processes with both oscillations and dissipation in a harmonic entropy potential with two variables, ξ_1 and ξ_2. Figure taken from [85].

The entropy production can then be written as

$$\frac{dS}{dt} = \sum_{ij} L_{ij} X_i X_j = \sum_{ijkl} L_{ij} g_{jk} g_{il} \alpha_k \alpha_l \tag{5.9}$$

where $X_i = -\sum_j g_{ij}\alpha_j$ and $J_i = \sum L_{ij} X_j = -\sum_{jk} L_{ij} g_{jk} \alpha_k$.

Assuming ξ_1 is temperature T, ξ_2 is another thermodynamic variable that oscillates, the entropy is conserved in an adiabatic reversible process. Therefore, if any other thermodynamic variables oscillate during such a process, the system will go around the entropy potential plane like the one shown in Fig. 5.2 (middle). This will result in an oscillation in temperature. In this chapter, we make efforts to measure the heat change during a nerve impulse and the Briggs-Rauscher reaction, which share the feature as an adiabatic reversible process. We then discuss these reversible oscillations with linear non-equilibrium thermodynamics.

5.2 Temperature Change of Nerve Impulses

5.2.1 Experimental

The thermopile made of Bismuth Telluride is provided by Martin Jägle's group from Fraunhofer Institute. It consists of 33 pairs of thermocouples that are constructed in series as shown in Fig. 5.3. The thermopile is supported by a polyimide film Kapton. Every third of the 33 thermocouples is connected to an electrode, so that there are 11/12 electrodes in total on each side. The thermopower of each thermocouple is around 400 $\mu V/K$, and thus the expected sensitivity over the whole thermopile is 12-14 mV/K.

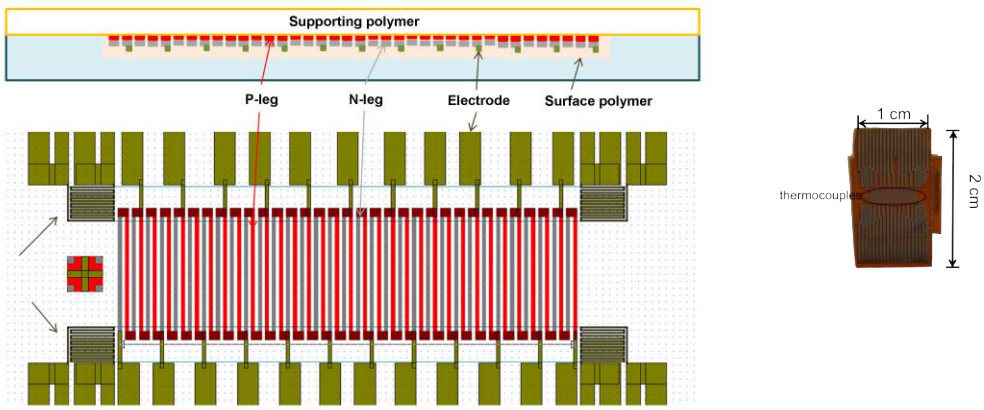

Figure 5.3: (a) Schematic illustration of the construction of the thermopile. The red lines are p-type thermocouples, and the gray lines are n-type thermocouples, different types of thermocouples are in analogous of two dissimilar metals. The green blocks are electrical connections. (b) a picture of the real thermopile. Thermocouples are in the black circle in the middle; the electrical connections are on the two sides (up and down) of the thermocouples; the brown base is the supporting kapton.

The thermopile chip was mounted in the middle of a nerve chamber as schematically shown in Fig. 5.4. The chamber is made of acrylic glass Lucite with electrodes (stainless steel pins) inserted in the small holes on the two sides. The nerve lay on top of the pins and the thermopile chip. Several drops of saline solution were added in the groove in the middle of the chamber to keep water vapor surrounding the nerve. Electrical stimulation pulses were sent out from a function generator of an integrated data acquisition (DAQ) instrument Powerlab 8/35. The signal in the thermal channel was amplified by 3333 times and the signal in the electrical channel was amplified by 1000 times before going into an AD converter from NI Instrument, and the data acquisition was controlled with a Labview program.

As the thermocouples are conductors with an internal resistance of around

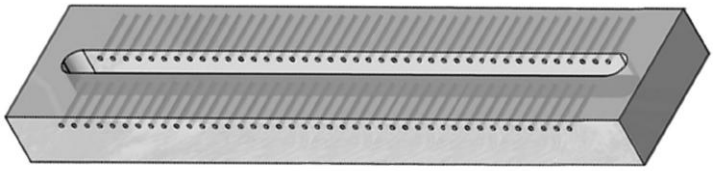

Figure 5.4: Schematic illustration of the nerve chamber. Stainless steel pins go through the small holes on the two sides working as electrodes. The nerve is placed on the electrodes. Electrodes for stimulation and recording are placed on two sides of the chamber, and the thermopile chip is mounted in the middle. Some drops of saline solution are dropped in the groove without touching the electrodes.

27 kΩ each, they also act as electrodes picking up the electrical signal from the nerve impulse. Therefore, one needs to electrically insulate the surface of the thermopile. Conformal coating and teflon-based coating were tried with spraying and spin-coating, respectively.

The thermopile chip was first coated with a DCA aerosol modified silicone conformal coating from Electrolube (UK). Before coating, the chip was rinsed by acetone, ethanol and millipore water respectively to remove possible contamination and dusts. It was then dried under clean nitrogen air. The coating was sprayed onto the thermocouples with the electrical connections at the ends covered by glass cover slips to protect electrical contacts. Two passes of spraying were done by hand with careful control of speed. The resulting thickness of the coating layer was estimated to be around 10 µm. After the solvent in the spray visually evaporated, such that it became a gel-like layer, the coated chip was left under vacuum for hours to totally remove the solvent. The chip was subsequently thermal annealed at 60 ℃ for 24 h (shorter time would be needed at a higher temperature).

5.2.2 Results and Discussions

Electrical and thermal measurements were first performed on nerve bundles from lobster walking legs. A typical result is shown in Fig. 5.5. The gray areas are stimulation artifacts. The electrical signal was measured along with thermal signal to confirm that the nerve was alive and functioning. Both signals were averaged 500 times. It can be seen in Fig. 5.5 (b) that there seem to be peaks of about 140 µK at around $t = 0.001$ s. However, the signal to noise ratio is rather low. Moreover, it cannot be excluded that the signal may be originated from thermocouples acting as electrodes due to electrical breakdown of the coating.

To test the coating we did measurements on a frog sciatic nerve, which contains axons of similar sizes with a myelinated layer around. This preparation was adopted for two reasons:
1) their action potentials are significantly larger in amplitude than those of the

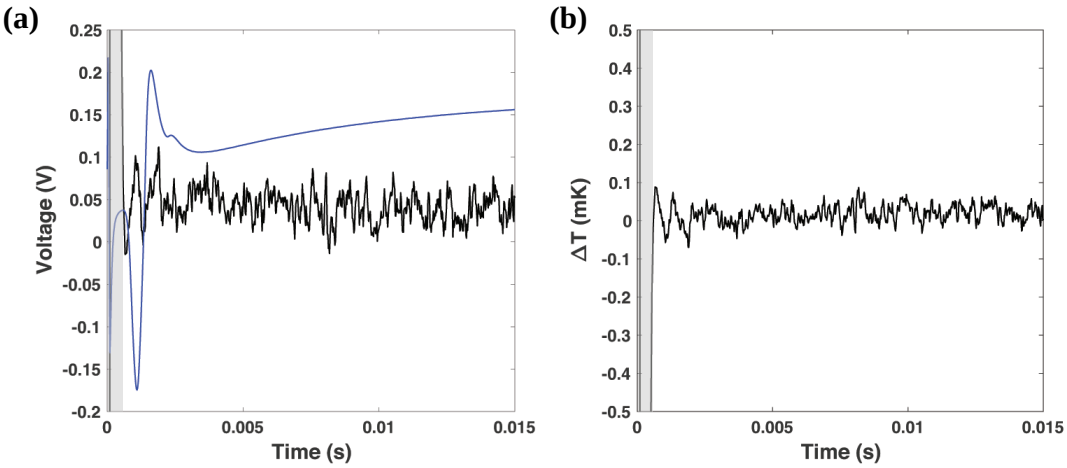

Figure 5.5: (a) Recording in electrical and thermal channels on nerve bundles from lobster walking legs. The black curve is the raw recording from the thermal channel,in which the signal is multiplied by a factor of 40 to compare with the electrical signal; and the blue curve is the extracellularly recorded action potential. (b) calculated temperature change with time.

nerves from lobster legs, and the expected heat released is lower due to the presence of myelin layer. The signal would thus be significantly larger than the expected heat if it is indeed due to the electrical signal in the thermal channel; 2) the saline solution of frog nerves has lower concentrations of ions, and therefore it would slow down the break-down of coating.

Fig. 5.6 shows a typical result of the measurement using a frog sciatic nerve. The temperature change is shown in Fig. 5.6 (b) and it has a maximum value of about 6 mK. This is about two orders of magnitude larger than what was reported from a frog sciatic nerve [49]. It indicates what was measured in the heat channel is likely to be an electrical signal from the nerve impulse because of the electrical break-down of coating. To further confirm this conclusion, we did the same measurement with the nerve placed on the other side of the thermopile. As the thermopile measures the temperature difference between the two measuring lines, if the recorded signal comes from a heat change, the sign of the temperature difference should be of the same magnitude but with opposite signs in this 'reversed' configuration. Thus the peaks should be reversed with similar amplitude. On the other hand, if it is the signal is due to an electrical pick up, the thermocouples do not have any change as electrodes. Thus the peaks should not change their signs and should have a similar response as shown in Fig. 5.6.

Fig 5.7 shows the signals recorded in the thermal channel with the nerve on the opposite side of the thermopile. One can see that the signal from electrical recording becomes weaker than in Fig. 5.6 (a), and so as that in the thermal channel. The sign of the peaks is not reversed, and the amplitude did not change significantly compared to that in Fig. 5.6 (b). This further confirms that the

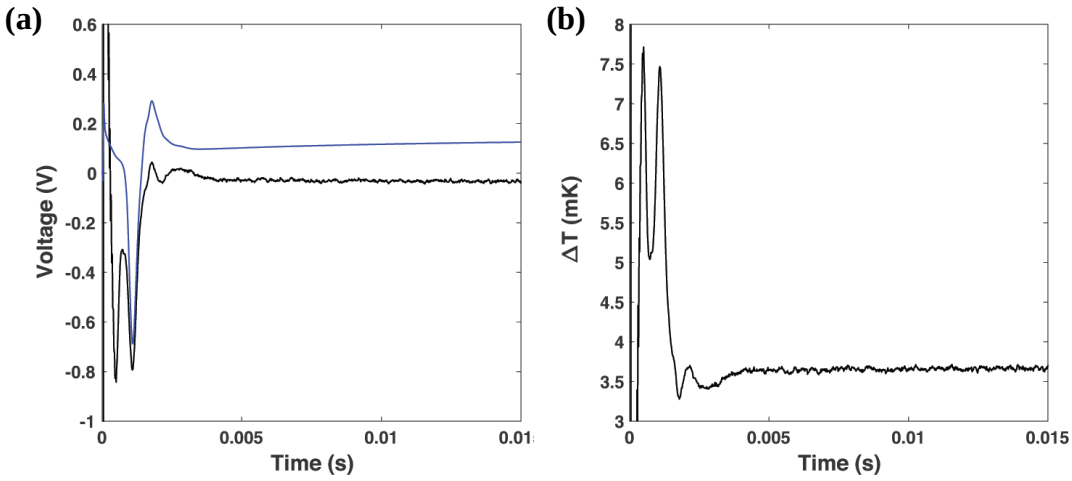

Figure 5.6: (a) Recording from electrical and thermal channels on frog sciatic nerve. The black curve is the raw recording from the thermal channel multiplied by a factor of 10 to be comparable with the electrical recording, and the blue curve is the extracellularly recorded action potential. (b) Calculated temperature change with time.

signal comes from an electrical action potential. Furthermore, it means that the coating procedure was not successful. Similar results were obtained with the Teflon based coating. At the moment, we are still working on the electrical insulation of the thermopile chip, thus no successful data on the temperature measurement on nerves are reported here. Below we show the measurement of heat change during a similar adiabatic process, Briggs-Rauscher reaction.

5.3 Temperature Change of Briggs-Rauscher Reaction

Briggs-Rauscher reaction is an oscillating chemical reaction, also referred to as the iodine clock reaction. It is named after Thomas S. Briggs and Warren C. Rauscher, who first reported the observation and measured the iodide oscillation during the reaction [83]. The reaction starts with several transparent solutions, which, when mixed together, give rise to a color oscillation from transparent to gold to blue. Pictures of solutions with these three colors are shown in Fig. 5.8.

Eventually the color becomes dark blue and does not change again after several minutes. The color oscillation is accompanied by oscillations in substances and heat.

5.3.1 Experimental

In our experiments, four solutions were involved in the reaction:
Solution 1 KIO_3;

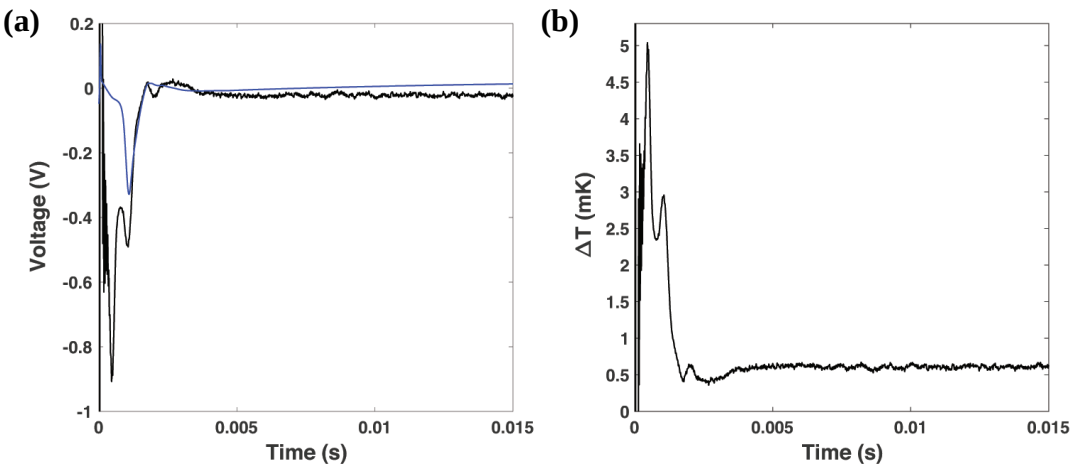

Figure 5.7: (a) Raw data in electrical and thermal channels after the nerve is moved to the other side of the thermopile. The black curve is the signal from the thermal channel, multiplied by a factor of 10 to be comparable with the electrical recording (the blue curve) (b) Temperature change calculated from the black curve in the left figure.

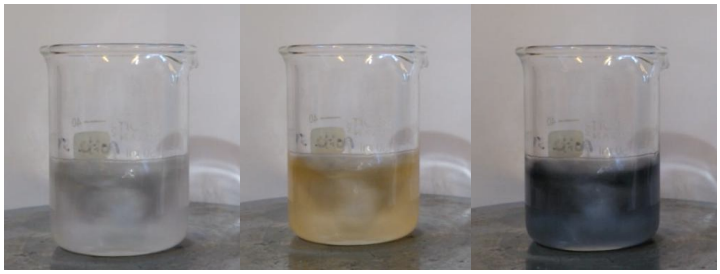

Figure 5.8: Pictures showing the color change in Briggs-Rauscher reaction. Left: transparent; middle: golden; right: blue.

Solution 2 H_2O_2 (30%) 33 ml (+67 ml H_2O), $HClO_4$ (70%) 2 g/100 ml;
Solution 3 Malonic acid 1.56 g/100 ml, $MnSO_4$ 0.34 g/100 ml, H_2SO_4 0.24 g/100 ml, Starch 1 g/100 ml (indicator);
Solution 4 $MnSO_4$ 0.3 g/100 ml.

The solutions were added in order into a beaker. A commercial T-type thermocouple was used to measure the temperature change during the reaction. It was coated with stainless steel to avoid being rusted by the corrosive solutions. Due to the coating layers, the response time of the thermocouple was prolonged to 0.5 s. Ice water was chosen as a reference. The signal was amplified 1000 times. Data acquisition was taken with an AD converter controlled by a Labview program. The sampling rate was 2 kHz. Data were subsequently smoothed and analyzed in Matlab with a lowpass filter of 40 Hz.

Thermal insulation of the beaker was tried later with simple plastic heat insulator, and stirring of the solution was tried by a magneton during the reaction process.

5.3.2 Results and Discussions

The temperature change during the reaction was first measured without heat insulation and stirring. The temperature change is shown in Fig.5.9 (a), which

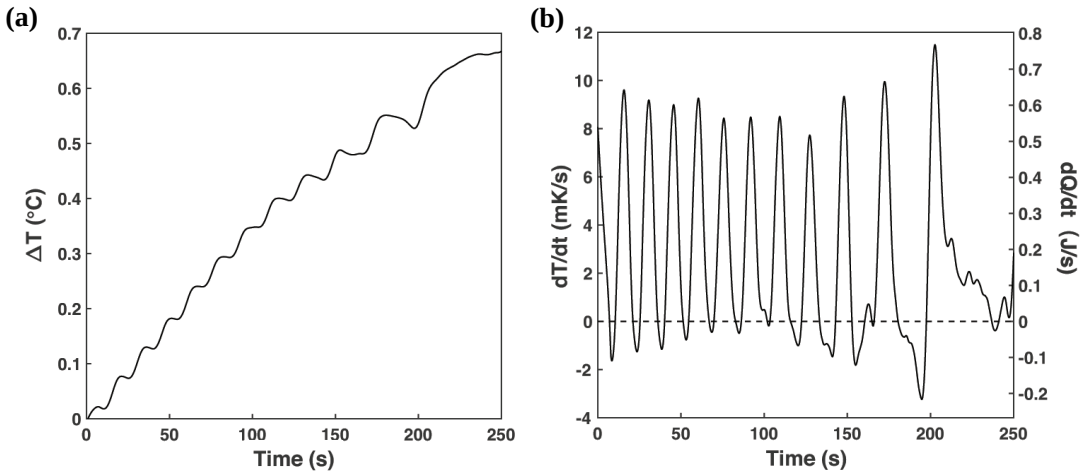

Figure 5.9: (a) Temperature changes in a Briggs-Rauscher reaction. (b) The time derivative of the heat change curve.

displays an oscillation manner with a continuous increase.

Assuming the atmospheric pressure does not change over the whole experimental process, the temperature change is related to the heat change through the heat capacity at constant pressure,

$$dQ = c_p dT \tag{5.10}$$

thus,

$$\frac{dQ}{dt} = c_p \frac{dT}{dt} \tag{5.11}$$

Assume that the heat capacity of the solutions has approximately the same value of water,i.e. 4.18 J·cm^{-3}·K^{-1}, the total volume of solutions involved in the experiments is 16 cm^{-3}, such that

$$\begin{aligned} \frac{dQ}{dt} &= 4.18\,(\mathrm{J}\cdot\mathrm{cm}^{-3}\cdot\mathrm{K}^{-1}\cdot 16\mathrm{cm}^{-3})\frac{dT}{dt} \\ &= 66.88\,(\mathrm{J}\cdot\mathrm{K}^{-1})\frac{dT}{dt} \end{aligned} \tag{5.12}$$

The time derivative of the temperature change is shown in Fig.5.9 (b) (left scale) and that of the heat change is calculated and shown in Fig. 5.9 (b) (right scale). One can identify negative areas in the curve, which indicates that there must be a heat absorption phase. The heat change can be considered as being composed of an oscillation in heat plus a heat release process. The period of oscillation is about 17 s at the beginning of the reaction, and is prolonged when the oscillation

is approaching the end. It is correlated with the color change during reaction, which is observed to slow down until it stops in a dark blue color.

The temperature increase could come from either the reaction or another process which releases heat. To investigate the origin of it, the same temperature measurement was performed implementing the following changes, respectively: 1) the reaction beaker was thermally insulated with a simple plastic heat insulation layer; 2) stirring was applied during the whole experiment process; 3) a lid was put on top of the beaker without any other insulation nor stirring.

The results will be described in the following, but data will be found in the appendix C. In all the three conditions, we found that the continuous increase has a significant larger magnitude than the results shown above. In addition, it continues to increase after the oscillations stop. It seems very likely that there is another heat dissipating process happening along with the oscillation reaction, as the temperature increase is more pronounced when heat dissipation into the environment is prevented. Stirring would promote this process. When a lid is put on the reaction container, a violet color on the lid is observed after the reaction. Considering the substances involved, it can be inferred that the color comes from iodine. The speculation is that there are iodine vapor mixed in the gas released from solution, which would subsequently deposit from vapor to solid state and release heat.

I^- was found to be an intermediate product, which also oscillates during the reaction [83]. The concentration of iodide ions was measured with an electrochemical setup. The basic idea of this approach is to measure the characteristic redox potential of I^- and make a specification curve. Subsequently the concentration of I^- is calculated from the response at the characteristic potential.

The I^- redox profile was measured in KI solution with cyclic voltammetry. Two characteristic peaks can be seen in Fig. 5.10 (a). The black lines are blank, red and blue lines are measured when the concentration of KI is increased by adding more KI into the solution. It can be seen that when the concentration of I^- is increased, the peak intensity also increases with more I^- involved in redox reactions. The reduction potential 0.5 V is chosen to be fixed on the working electrode and the current change with time is measured, which is proportional to the concentration of I^-. Fig. 5.10 (b) shows that the concentration of I^- displays oscillations during the reaction process and increases at the end of the oscillation.

Different studies on the mechanism of the reaction have shown that there are many substeps during the reaction process [90, 91, 92, 93]. Overall it is an autocatalyzed reaction. In Sec. 5.1, it has been stated that every process can be described as a sum of a dissipation process described by the symmetric matrix ($\underline{\underline{L}}^S$) and an oscillation described by the antisymmetric matrix ($\underline{\underline{L}}^A$). With oscillations, we only take into account the antisymmetric terms.

The fluxes associated with heat and concentration of I^- are heat (and entropy) flux (J_q) and particle flux (J_c), with conjugated thermodynamic forces

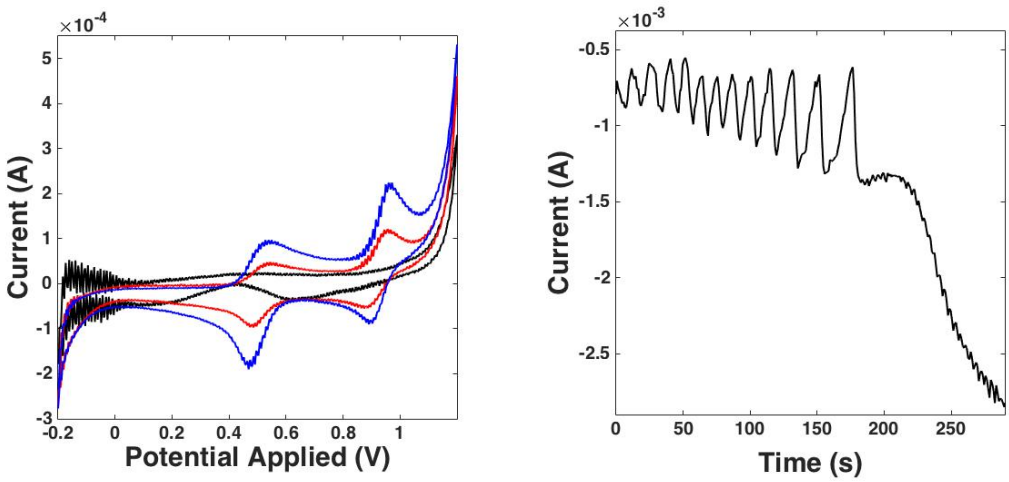

(a) (b)

Figure 5.10: (a) Cyclic voltammetry of I^-. The black traces are blank; red and blue traces are with the concentration of I^- increased. The potential was first increased linearly and then decreased in the same manner. Positive peaks are cathodic currents (increasing potential), and negative peaks are anodic currents (decreasing potential). As the redox reactions of I^- are reversible, the cathodic currents and the anodic currents are symmetrical. The characteristic peak we chose in the following experiment is the reduction peak at 0.5 V. (b) Current trace when characteristic reduction potential (0.5 V) was fixed on the working electrode. The concentration of I^- is proportional to the current. The electrochemical measurement was done in collaboration with Lingling Zhang from Aarhus University.

$X_Q = grad\left(\frac{1}{T}\right)$ and $X_i = grad\left(-\frac{\mu_i}{T}\right)$. Considering the system with these two variables, the phenomenological equations follow

$$\begin{aligned} \frac{dQ}{dt} &= J_q = L_{12}^A X_i = -L_{12}^A(g_{21}Q + g_{22}c) \\ \frac{dc}{dt} &= J_c = -L_{12}^A X_q = L_{12}^A(g_{11}Q + g_{12}c) \end{aligned} \tag{5.13}$$

The time derivatives are

$$\begin{aligned} \frac{d^2Q}{dt^2} &= -L_{12}^A\left(g_{12}\frac{dQ}{dt} + g_{22}\frac{dc}{dt}\right) = -(L_{12}^A)^2 det(\underline{\underline{g}})Q \\ \frac{d^2c}{dt^2} &= L_{12}^A\left(g_{11}\frac{dQ}{dt} + g_{12}\frac{dc}{dt}\right) = -(L_{12}^A)^2 det(\underline{\underline{g}})c \end{aligned} \tag{5.14}$$

which displays periodic solutions with $Q = Q_0 cos(\omega t + \phi_1)$ and $c = c_0 cos(\omega t + \phi_2)$ with a frequency ω ($\omega^2 = (L_{12}^A)^2 det(\underline{\underline{g}})$). Thus, the antisymmetric matrix leads to oscillations in heat and concentrations in the system.

5.4 Summary

The heat change during a nerve impulse was measured, but with no success due to technical problems to be solved. Instead, we measured the heat change during an oscillation reaction, Briggs-Rauscher reation that shares the adiabatic reversible feature with the nerve impulse. The heat and concentration of iodide were found to oscillate with time. The oscillations in adiabatic reversible processes can be described with methods of linear non-equilibrium thermodynamics.

Chapter 6

Local Anesthetic Effect on Action Potential Propagation in Unmyelinated Nerves

6.1 Background

Local anesthetics reversibly cause regional loss of sensation, which provides pain relief effect during surgeries. The first extracted anesthetic is cocaine, which was used as an anesthetic during medical procedure from 1884. After that, synthetic alternatives such as procaine and tetracaine were developed and commonly used as local anesthetic. However, they cause allergic reactions. Until 1943, lidocaine was discovered and an alternative class, amide-type anesthetics have been widely applied in clinical applications ever since.

Since Hodgkin and Huxley proposed the HH model for action potentials [25] and the discovery of ion channel proteins [94, 26], the action of local anesthetics has been mostly attributed to the effect on sodium ion channels. Two main theories are as follows:

• The membrane expansion theory: anesthetics are absorbed into the hydrophobic regions of the nerve membrane, resulting in an local expansion of the area and volume of the membrane matrix [95]. This may induce a decrease in the diameter of sodium channels, resulting in inhibition of both sodium conductance and neural excitation [96, 97].

• The specific receptor theory: local anesthetics bind to a specific receptor existing in the sodium channel either on its external surface or on the surface facing internal axoplasm [98, 99]. Once the binding happens, the permeability of sodium ions is decreased or suppressed, such that the nerve cannot be excited. The specific receptor theory is more widely accepted.

Both theories involve a blocking effect of the sodium channels, which can be intuitively described by the Noble's model (introduced in Chapter 1) for nerve excitation. Fig. 6.1 shows the membrane current-voltage relation with different

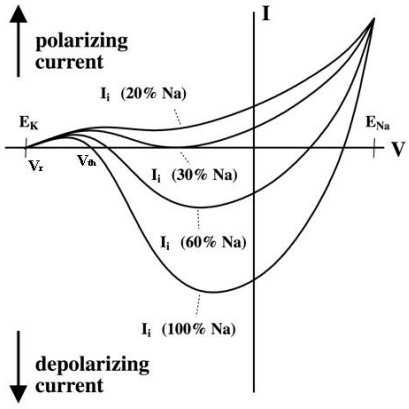

Figure 6.1: The membrane current-potential relation with different percentages of sodium channels blocked by local anesthetic. The numbers of percentage are for the sodium channels that are still functioning. The calculation is done by Thomas Heimburg with data digitized from [27].

percentages of sodium channels blocked by anesthetics. One can see that the membrane depolarizing current becomes smaller with the blockage of sodium channels, meaning a smaller number of sodium ions will be able to move across the membrane, and thus an action potential with a smaller amplitude. Moreover, When 30% of the sodium channels are left functioning, there is no depolarizing current anymore, which means that the membrane cannot be depolarized, and thus no action potential can be initiated anymore. At this point, the threshold potential (V_{th}) is shifted by a maximum degree of about 2.6 times magnitude of the original value.

While in the Soliton model, the change in membrane potential is a piezoelectric effect. Since anesthetics do not change much of the ion distribution on the two sides of the nerve membrane, as well as the thickness change during an action potential, the amplitude of the action potential is expected to be largely unchanged by anesthetics. Moreover, since the anesthetics can lower the melting point of biological membranes further than 2.6 times, one would thus expect that the stimulation threshold would be able to be shifted to a higher value.

6.2 Materials and Methods

6.2.1 Nerves

Three types of nerves are involved in the work of this chapter, namely circumoesophageal connectives (referred to as connectives hereafter) from lobsters, the abdominal ventral cord from lobsters and the ventral cord from the earthworms. The anatomy of the abdominal ventral cord from lobsters and the ventral cord from the earthworms have been described in Chapter 3.

There are two connectives in a lobster. The connections between them are cut

in the middle of the ganglia on the two sides. Each of them contains a number of groups of axons with different diameters. One to three of them are giants with a diameter of about 100 µm [100, 101, 102]. Fig. 6.2 (a) shows the whole nerve

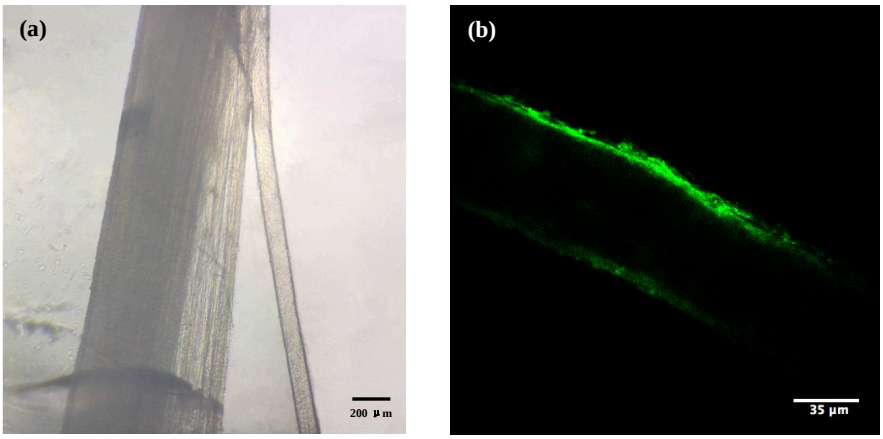

Figure 6.2: (a) Picture of a single axon separated from the nerve bundle of cumoesophageal connectives. (b) Picture taken by confocal fluorescence microscope on a separated single axon (a different axon from the one shown in (a)). The axon was separated and dyed with Laurdan, which combines to lipid membranes. The picture under confocal microscope was taken in collaboration with Jonathan R. Brewer from University of Southern Denmark.

bundle with one of the giant axons separated under a dissection light microscope. One can recognize a number of smaller axons in the bulk bundle apart from the giant axon on the right. Fig. 6.2 (b) shows one of the axons under confocal microscope with its lipid membrane stained.

6.2.2 Chamber

Experiments with nerve bundles of circumoesophageal connectives from lobsters were conducted in a nerve chamber with pockets. The electrodes lay on the bottom of the pockets. Segments of nerves were separated by Vaseline in order to hold solutions in a certain pocket, preventing short circuiting between the stimulation and recording electrodes. The pocket with the stimulation electrodes was injected with 250 µl saline solution, and the action potential was measured with increasing stimulation voltages as a control response. A certain volume of lidocaine saline solution was then added into the stimulation pocket to a final lidocaine concentration in the pocket to be 100 µM. Subsequently the action potential was recorded again with the stimulation voltage increased gradually.

Experiments with the abdominal ventral cord from lobsters were conducted in the liquid chamber which contains a glass capillary with gold electrodes surrounding the nerve as shown in Chapter 3. The action potential was first recorded with the nerve in the saline solution as a control experiment. Subsequently the

solution was exchanged by a 50 µM lidocaine-saline solution, and the action potential was then recorded again with the stimulation voltage increased gradually. The liquid chamber was only used for this particular nerve due to match between the diameter and length of the capillary and those of the nerve. Other species of nerves available did not fit.

Experiments with the ventral nerve cord from earthworms were conducted in a normal nerve chamber as shown in Fig. 4.7. The action potential was first recorded with the nerve lying on the electrodes and with stimulation voltage increased gradually. Several drops of saline solution were placed in the groove without touching the electrodes. A lid was put on top of the chamber to keep a saturated water vapor inside the chamber. The nerve was then taken off the chamber and put into a petri dish with lidocaine-saline solution for several minutes. Afterwards, the electrical recording process was repeated. The above procedures were repeated several times to find an efficient diffusion time of lidocaine into the nerve membranes. With this method, care needs to be taken with the amount of saline solution attached to the nerve every time before it is placed onto the chamber. Since the extracellular recording measures the potential difference between the two recording electrodes, any difference of amount of saline solutions on the chamber would result in a deviation of the peak amplitude, which will make the comparison of amplitude not meaningful.

6.2.3 Lidocaine

The local anesthetic used in this chapter is lidocaine. Its chemical structure is shown in Fig. 6.3. Lidocaine is an amide-type local anesthetic. The amide group

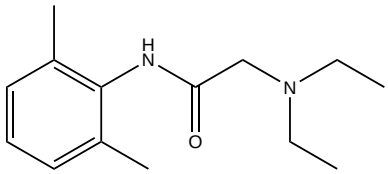

Figure 6.3: The chemical structure of lidocaine, generated by ChemDraw Professional.

is charged at low pH value. Its pKa value is estimated to be 7.9 [103, 104], and the physiological pH value is about 7.4. At pH = 7.4, the aqueous solution is a mixture of charged and uncharged lidocaine molecules. The membrane-water partition coefficient of the uncharged form is higher than that of the charged form [103]. The uncharged form is hydrophobic, which tends to insert into the hydrophobic hydrocarbon chains of the lipid membrane. The charged form is amphiphilic, with the uncharged hydrophobic side tending to stay close to the backbone of the lipid membranes, leaving the charged hydrophilic amide group in water [105].

Lidocaine is a widely used local anesthetic with a long history since 1943.

It was the first amide-type local anesthetic discovered to be an alternative to procaine and tetracaine due to their allergic effect. Therefore, more information and parameters about lidocaine and lidocaine-membrane system are available. Moreover, it has a relatively low lipid-water partition coefficient such that the kinetics are slowed down for the convenience of electrical recording. These are the reasons that lidocaine was chosen as the model local anesthetic for this chapter.

Lidocaine was dissolved in the saline solution for corresponding nerve species. A stock solution of 500 µM lidocaine-saline solution was prepared, and diluted to a desired concentration every time before starting the experiments. pH was monitored so that it is the same as the saline solution, as a difference in pH value would result in a shift of melting transition, and thus a change of threshold for the action potential saturation.

6.3 Results and Discussions

6.3.1 Results

Connective from lobsters

Typical action potentials recorded from the connectives before and after treatment of lidocaine are shown in Fig. 6.4 (a). The sharp peaks in the gray area are

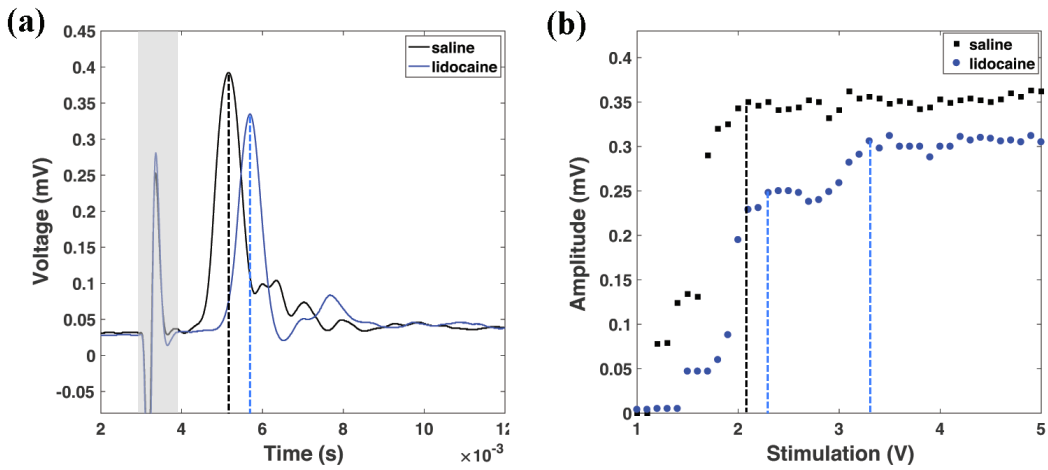

Figure 6.4: The action potential recorded from the connectives of lobsters before and after being treated to lidocaine. (a) The temporal shape of the action potentials. The black curve is the action potential in the control experiment, and the blue curve is after treatment of lidocaine. (b) Peak amplitude as a function of stimulation voltage. The black dots are from the control experiments measured in saline solution. The blue dots are measured from the lidocaine treated nerve.

stimulation artifacts. The peaks from the nerve impulses are compound action potentials (CAPs) from different groups of axons. From Fig. 6.4 (a), we can directly identify two features of the first CAP. Firstly, there is a slight decrease in

the peak amplitude; secondly, the latency between stimulation and the peak increases, indicating a decrease of conduction velocity. The peak amplitude is then plotted as a function of stimulation voltage and shown in Fig. 6.4 (b). When the nerve is in the saline solution (before exposure to lidocaine), the peak amplitude reaches a maximum value at about 2.1 V stimulation. After treated with lidocaine, there are two steps with a threshold-like characteristic, the first threshold is close to that in the saline solution, and the second is increased significantly to about 3.3 V. This results from the concentration gradient of lidocaine in the pocket due to diffusion from where it is added. The axons close to the solution adding point are exposed to lidocaine for a longer time than the others, as well as a higher lidocaine concentration. To eliminate this diffusion effect, experiments were conducted with abdominal ventral cord from lobsters in the liquid chamber where solution can be changed homogeneously.

Abdominal Ventral cord from lobsters

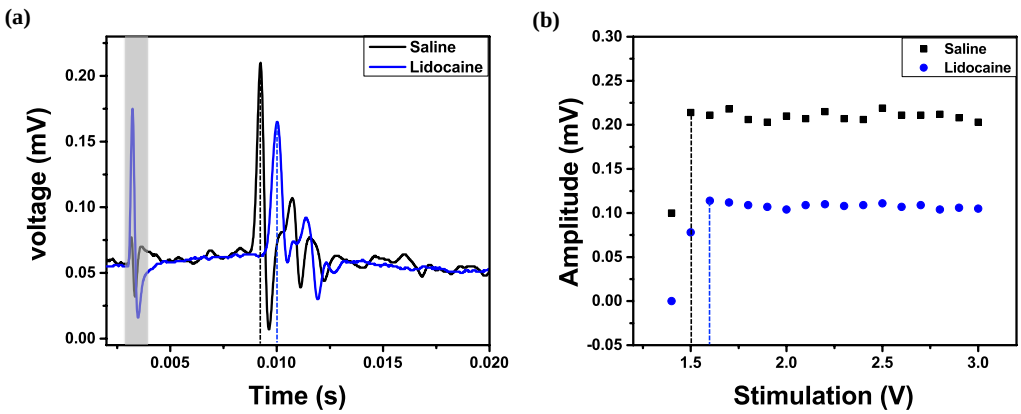

Figure 6.5: The action potential recorded from the abdominal ventral cord of lobsters before and after being treated to lidocaine. (a) The temporal shape of the action potentials. The black curve is the action potential in the control experiment, and the blue curve is after treatment of lidocaine. (b) Peak amplitude as a function of stimulation voltage. The black dots are from the control experiments measured in saline solution. The blue dots are measured from the lidocaine treated nerve.

The peaks in Fig. 6.5 also represent the compound action potentials from groups of neurons. The data analysis was done in the same way as that for connective nerves. The action potentials in Fig. 6.5 (a) display the same changes as those in connective nerves before and after treatment of lidocaine, i.e. a decrease in the conduction velocity and a decrease in the peak amplitude. The peak amplitude of the first CAP as a function of stimulation voltage is plotted in Fig. 6.5 (b). The threshold for peak saturation is increased by lidocaine.

Ventral Cord From Earthworms

The ventral cord from earthworms contain three giant neurons, one median giant and two lateral giants. The two lateral giants are connected to each other at each ganglion. Two peaks are present in Fig. 6.6 (a). The first peak corresponds to the action potential from the median giant neuron, which is adopted here to represent the response of a single neuron, and the second peak is a compound action potential from the two lateral giants [106]. The stimulation artifact at

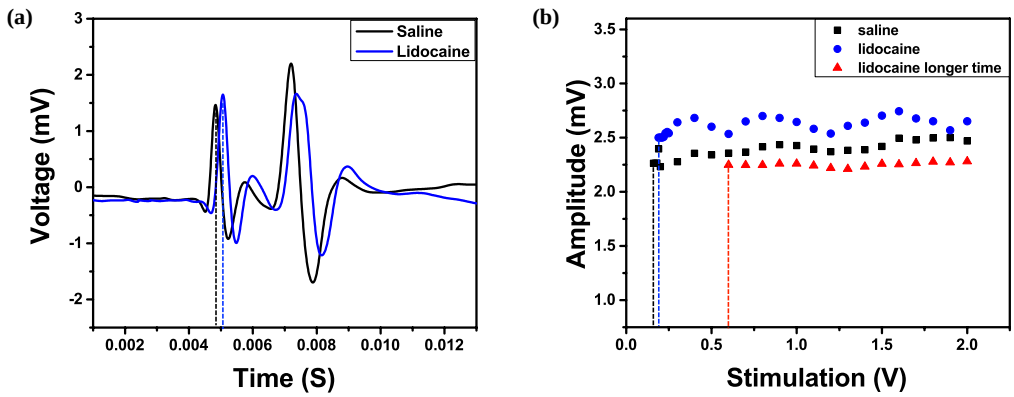

Figure 6.6: The action potential recorded from the ventral cord of earthworms before and after being treated to lidocaine. (a) The temporal shape of the action potentials. The black curve is the action potential in the control experiment, and the blue curve is after treatment of lidocaine. (b) Peak amplitude as a function of stimulation voltage. The black dots are from the control experiments measured in saline solution. The blue dots are measured from the lidocaine treated nerve.

Time = 0.003 s can barely be seen as the action potentials from earthworm ventral cord have significantly larger values than those from the lobster nerves. The latency between the stimulation and the peak increased for both peaks, indicating a decrease in conduction velocity for both peaks. The peak amplitude of the first peak is plotted in Fig. 6.6 (b) as a function of stimulation voltage. The plot for nerve treated with lidocaine for different time are shown in the figure to show that there can be a variation in peak amplitudes due to a slight difference in the amount of saline solution attached to the nerve. The amplitude of the peak almost did not change before and after treatment of lidocaine in the range of experimental system errors. The threshold for the peak appearance is raised from a value of 0.2 V to a value of 0.7 V, which is a change of more than three times.

From the data above, one can extract the following effects of lidocaine on nerve impulses:

• For compound action potentials, the velocity and peak amplitude are both decreased, and the threshold for peak amplitude saturation is raised.

• For the action potential from a single neuron, the velocity decreases, the peak

amplitude stays almost unchanged, and the threshold for the peak saturation can be raised up to more than three times.

6.3.2 Discussions

A even larger threshold shift has been found by Moldovan et al. [107]. They measured the compound action potential on human arms, stimulating at the wrist, and recording on the thumb. Lidocaine was injected with a needle into the arm, close to the median giant nerve. After injection, the nerve was anesthetized with action potential suppressed. The recovery of action potentials was monitored. The peak response as a function of the stimulation current curve during the recovery was recorded. Their data was digitized and replotted in Fig. 6.7.

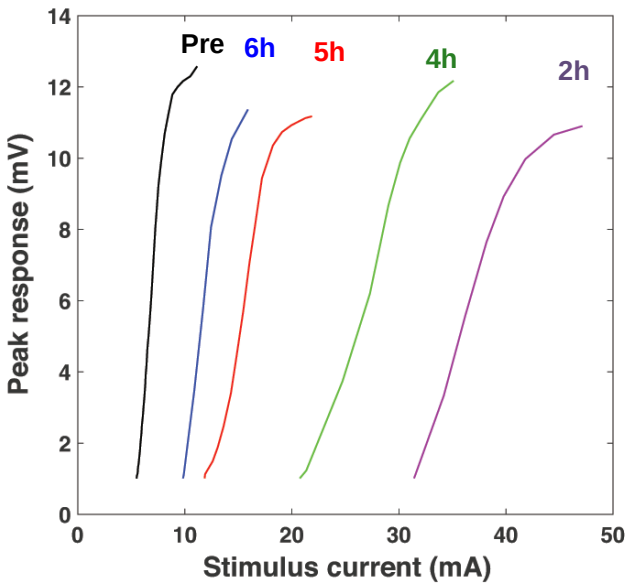

Figure 6.7: The peak response as a function of stimulation current in human arms. The stimulus-response relation are shown before injection of lidocaine (Pre) and at different recovery time points (2 h, 4 h, 5 h, 6 h) after the injection of lidocaine. The original data were plotted in a logarithm scale. The data was digitized from Fig. 3B Moldovan et al. 2014 [107] and replotted in a regular scale.

It can be found that the threshold for peak saturation increased from about 8 mA to a highest measured value of 48 mA, 6 times of the value without lidocaine treatment. The stimulation was stopped below 50 mA due to ethical restrictions. It may be possible that the threshold would continue to be shifted to a higher value provided that the stimulation does not cause a danger to the human body. The observation of threshold shifting cannot be explained by the HH model as the nerve cannot be depolarized anymore after a shift of about 2.6 times. However, it is consistent with the prediction of the Soliton model. Below, the Soliton model will be adopted to explain the effects of lidocaine on action potentials.

Threshold Shifting

As discussed in Chapter 1, anesthetics shift the melting transition of lipids between the gel phase and the fluid phase to a lower degree. DPPC unilamellar vesicles are taken as a model system of membranes, which have a melting temperature of about 41 ℃. The heat capacity profile of DPPC large unilamellar vesicles with different amount of lidocaine are shown in Fig. 6.8 (a). In the phase transition, the heat capacity displays as a peak. The maximum value of the peak is defined as the melting temperature at which half of the lipids are in the fluid phase, and half of them are in the gel phase. The melting temperature of DPPC membranes is shifted to a lower degree with increasing amount of lidocaine in the solution.

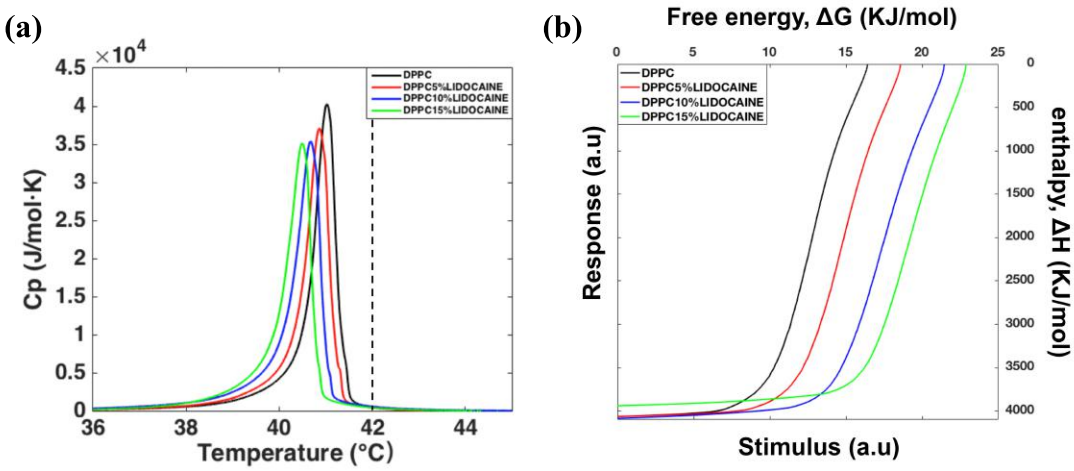

Figure 6.8: (a) The heat capacity profile in the range of the melting transition of 10mM DPPC large unilamellar vesicles (LUVs) with different ratios of lidocaine measured by DSC. The concentration ratios of lidocaine: DPPC = 0, 5%, 10% and 15%, respectively. The rightmost dashed line represents an arbitrary physiological temperature for DPPC model system. (b) The free energy profiles calculated from the heat capacity profiles of DPPC LUVs with different ratios of lidocaine.

As mentioned in Chapter 2, in biological membranes the melting transition is always found to be slightly below the body temperature, a physiological temperature in this model system is arbitrarily defined to be about 42 ℃, slightly above the melting transitions, shown as dashed line on the rightmost in Fig. 6.8 (a).

According to the Soliton theory, during a nerve impulse, the nerve membrane undergoes a phase transition from the fluid phase to the gel phase, and then back to the fluid phase. When lidocaine is added into the system, the phase transition temperature is lowered, such that it becomes further away from the physiological temperature. As a consequence, more free energy is needed to move the membranes from the fluid phase under physiological condition to the gel phase, meaning that a higher stimulation energy needs to be provided to the nerve to initiate an action potential, corresponding to a higher stimulation voltage in

our experiments. The free energy profiles are calculated from the heat capacity profiles and shown in Fig. 6.8 (b). The curves from the left to the right are with an increasing concentration of lidocaine. One finds a higher free energy, corresponding to a higher stimulus required to get a maximum response with increasing concentrations of lidocaine.

Conduction Velocity and Amplitude of Action potentials

The peak amplitude of action potentials stays almost unchanged when treated with lidocaine, while the decrease in the amplitude of the compound action potential may be due to a decrease in the conduction velocity, which results in a separation effect of the action potentials appeared in a peak. As mentioned in Sec. 6.1, local anesthetics causes a local expansion of the nerve membrane, with their molecules diffused into the membrane. The distance between adjacent lipid molecules would thus increase. As a result, the minimum velocity of a soliton would decrease. Fig. 6.9 show the calculated (a) maximum soliton profiles

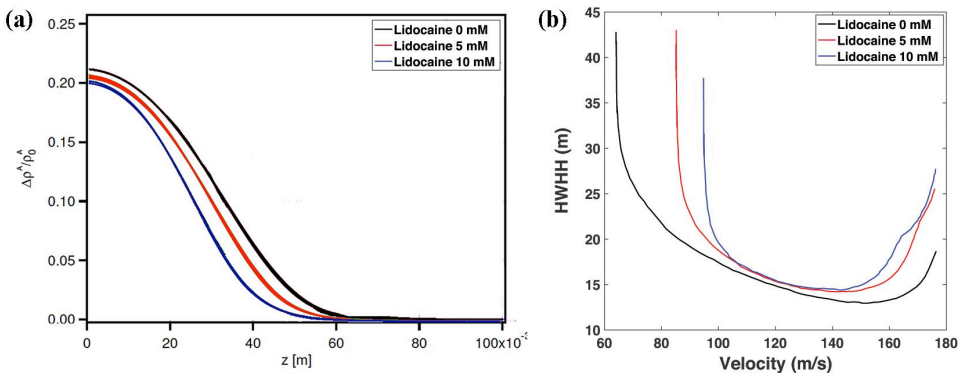

Figure 6.9: (a) Maximum soliton profiles of DPPC LUVs (10 mM) with different amounts of lidocaine. (b) Half width at half height as a function of velocity from the soliton profiles of DPPC LUVs with different amounts of lidocaine. Figures adapted from [108].

and (b) half width at half height as a function of velocity. Fig. 6.9 (a) shows that the maximum amplitude of a soliton is almost unchanged with increasing amount of lidocaine in the system. Fig. 6.9 (b) shows the half height at half width (HWHH) as a function of the velocity. The HWHH displays a minimum value at the minimum velocity. One finds a slight decrease in the minimum velocity with increasing concentrations of lidocaine in the system. The figures are taken from Kaare Græsbøll's master thesis [108] and replotted.

6.4 Summary

Local anesthetic effect is studied with the nerve bundles of connective from lobsters, abdominal ventral cord from lobsters, and the ventral cord from earth-

worms. For compound action potentials, the conduction velocity and the peak amplitude are decreased, and the stimulation threshold is increased by local anesthetic lidocaine. For action potentials from a single neuron, the conduction velocity decreases, peak amplitude stays largely unchanged and the stimulation threshold can be shifted up to more than 2.6 times. These effects can be explained under the framework of the Soliton model.

Chapter 7

Effect of Stretch on Conduction Velocity of Action Potentials in the Ventral Cord from Earthworm *Lumbricus terrestris*

7.1 Background

The equation in HH model for propagating action potential is as follows

$$\frac{a}{2R_i\theta^2}\frac{\partial^2 V}{\partial t^2} = C_m\frac{\partial V}{\partial t} + g_{Na}(V - E_{Na}) + g_K(V - E_K) + g_L(V - E_L) \tag{7.1}$$

where a is the radius of the nerve cylinder, θ is the conduction velocity and R_i is the specific resistance of axoplasm. They are related to each other in the following manner

$$\theta = \sqrt{Ka/2R_i}C_m \tag{7.2}$$

where K is constant, and C_m is the capacitance per unit area of the membrane [25]. This indicates that the conduction velocity of a propagating action potential for the same membrane and axoplasm of a neuron should vary as the square root of the nerve diameter [109].

The relation between the conduction velocity and the nerve diameter has been extensively studied experimentally. Several widely applied approaches are as follows:

1) Some of the axons in a nerve bundle are cut in the middle so that either only the giant axon is left functional, or the signal of the giant axon can be well separated from that of the smaller ones. The conduction velocity for the giant axon is then measured. Subsequently, the diameter of the axon is determined by techniques like microscopes. Different values are then compared between different samples from the same species of nerve [110].

2) The conduction velocity is determined during the growth of normal or regenerated neurons, when the diameter also growths. Thus the values are compared on the same nerve at different growth period [111, 112].

From those types of measurements, the conduction velocity was determined to be $\theta = kD^x$, where θ is the conduction velocity, D is the diameter of the nerve, k is a constant and x varies between 0.5 and 1. Generally the conduction velocity is a linear function ($x = 1$) of diameter in vertebrate myelinated fibers [113, 114, 115, 116], and proportional to the square root ($x = 0.5$) of diameter in unmylinated nerves [110].

However, in the two kinds of measurements mentioned above, the physiological conditions may vary from sample to sample or at different growth periods. Bullock et al. [117] measured the conduction velocity of the giant fibers of *Lumbricus terrestrisis* with the nerve stretched, so that the diameter decreases with stretching. In this case, the values are compared on the same nerve in the same growth period. No appreciable change in the conduction velocity was observed in their work for both the median giant neuron and the lateral giant neurons. However, it was a conference paper and no data plots were shown. Goldman applied this approach in *Lumbricus terrestrisis* and *Aplysia* nerves, and confirmed that the conduction velocity stays constant even after being stretched for considerable lengths [118, 119]. He found that the diameter of the median giant neuron did not change until the nerve was stretched twice of its original length. After this point, the diameter began to decrease as shown in Fig. 7.1. When the nerve was

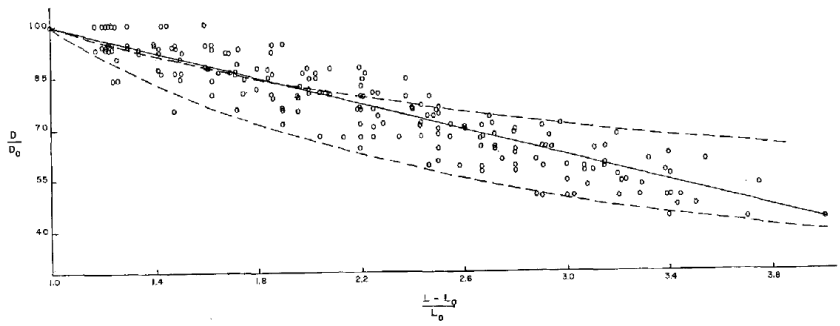

Figure 7.1: The relative change of fiber diameter as a function of the relative length change (from resting length L_0 to stretched length L) in Goldman's measurement. Figure taken from [118].

stretched four times the original length, the nerve was mechanically deformed.

During this stretching process, the conduction velocity first increased due to the uncoiling of the axons inside. When the diameter began to decrease, it remained constant. Finally, when the nerve was close to deformation, the conduction velocity displayed a rapid decrease because of damage of tissues. The change in conduction velocity as a function of change in the length is shown in

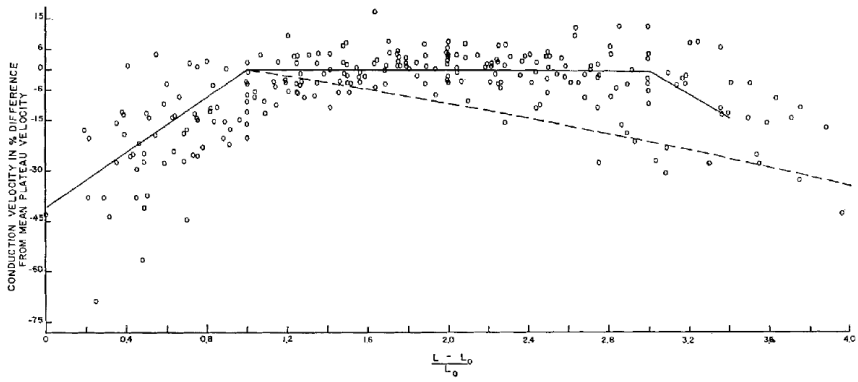

Figure 7.2: The conduction velocity in percentage of the zero-slope solid line as a function of the fraction of change in the fiber length. With a change in the fraction of fiber length from 0 to 1, the conduction velocity increases; between 1 and 3, the conduction velocity stays unchanged; after 3, the conduction velocity falls. The solid line is a fit of the scattered experimental data, and the dashed line is a theoretically predicted velocity to the diameter change.

Fig. 7.2. The ventral cord of earthworms could be stretched up to four times the original length [118].

This contradicts the prediction from the HH model, instead it is consistent with the Soliton model which doesn't include a diameter dependence of the conduction velocity. To further examine the diameter dependence of the conduction velocity of an action potential, the ventral cord of earthworm *Lumbricus terrestrisis* was extracted and stretched with the action potential recorded extracellularly, and the conduction velocity of the lateral giant axons was studied.

7.2 Materials and Methods

Nerve The nerve used in the work of this chapter is the ventral cord from the earthworms. The dissection process has been described in Chapter 3 and the anatomy has been described in Chapter 4. Briefly about the anatomy, there are three giant neurons that run the length of the body. One of them is the median giant nerve, which has the largest diameter of up to 0.07 mm . The other two are the lateral giant nerves, which have similar sizes of up to 0.05 mm diameter, slightly smaller than the median giant axon. They are connected (usually called fused) at each ganglion [120].

Chamber The nerve chamber is a 3D printed plastic chamber shown in Fig. 7.3. Small holes on the two sides of chamber hold the stainless steel pins, which act as electrodes for electrical stimulation and extracellular recording. The distance between two adjacent pins is 2.5 mm. The nerve lies on the pins during experiments. The action potential was measured with two pairs of recording electrodes,

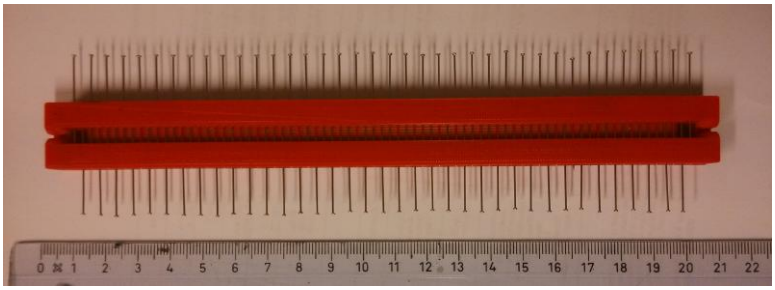

Figure 7.3: A picture of the plastic chamber with stainless steel pins as electrodes used in the stretching experiments.

and conduction velocity was calculated as the distance between the two pairs of recording electrodes divided by the time delay it travels between this two points.

Stretching device The stretching part of the setup consists of a stepmotor (Phidget Stepper P/N 1067), a gear, two tracks and a slide block. A picture of the the setup is shown in Fig. 7.4. The stepmotor is connected to a gear which

Figure 7.4: A picture of the stretching setup. A bipolar stepmotor on the right side of the picture is attached to a geared track, allowing for stretching when the motor moves.

controls the movement of the slide block. The nerve chamber is placed close to the right side of this device, as the stepmotor creates certain noise which can be picked up by the electrical measurement if they are close. The nerve is tied with a piece of thin thread connected to the slide block, such that the nerve is stretched when the slide block moves. The stepmotor is controlled by Matlab program with the direction, speed, and round number which correspond to the direction, speed and distance of the stretching respectively.

7.3 Results and Discussions

A typical action potential recorded extracellularly is shown in Fig. 7.5. At low stimulation voltages, there is only one peak (Fig. 7.5 (a)). This is the action potential from the median giant neuron. As the stimulation increases, another peak shows up later then the first peak (Fig. 7.5 (b)). This is the action potential from the two lateral giant neurons [106].

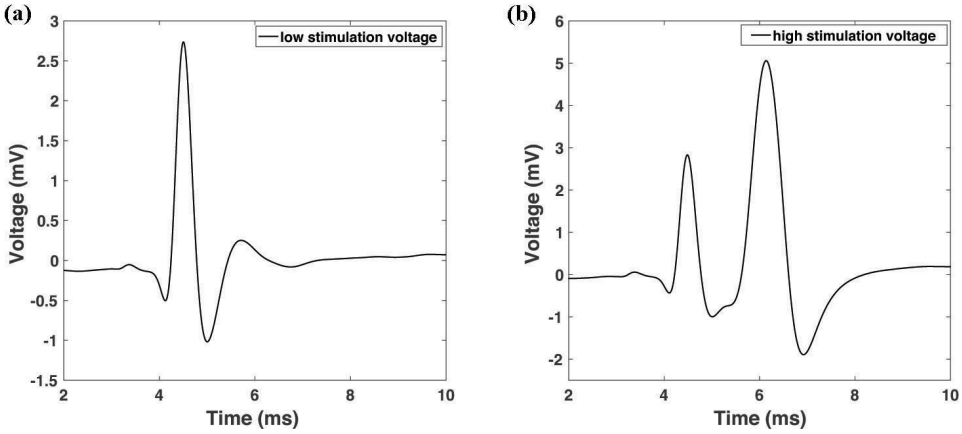

Figure 7.5: Typical action potential recorded extracellularly. (a) At lower stimulation voltage, only one peak shows up. (b) At high stimulation voltages, two peaks show up.

We focus on the response from the lateral giant neurons, as the results for the median giant axon have been shown in detail by Goldman [118]. Besides, the lateral giant axons can tolerate a higher degree of stretch as found in our experiments, which is consistent with what Bullock et al. found [117]. A typical result is shown in Fig. 7.6. The abscissa axis is the ratio of stretch relative to

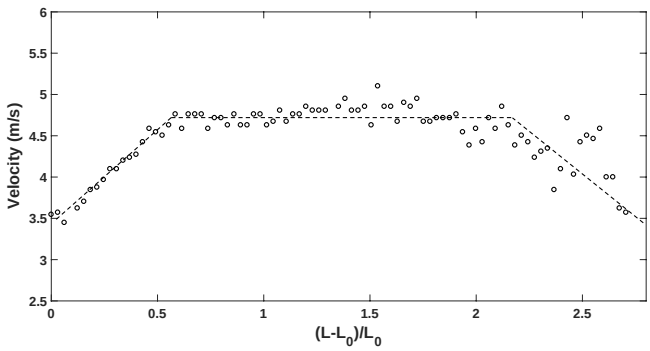

Figure 7.6: Conduction velocity of the second peak as a function of the ratio of length change of the ventral cord from the earthworm.

the initial length. The ordinate axis is the conduction velocity in m/s. One can clearly see the striking similarity to the results for the median giant neuron by Goldman as shown in Fig. 7.2 [118]. The conduction velocity first increases until the nerve was stretched 0.7 times its original length, subsequently it stayed constant until just before the deformation of the nerve, at which point it starts to decrease rapidly. The experiments were terminated when the nerve deformed, and thus the curve is not reversible. The nerve could be stretched about three times longer than the initial length in most of our experiments, shorter than that (four time longer) in Goldman's work [118] probably because the thread in our experiments induced a higher pressure on the nerve than the clamp they used. In addition, Goldman also mentioned in a later study that the exact nerve length

at which the velocity begins to be constant and to decline vary from nerve to nerve. Unfortunately, the change in diameter has not been monitored yet in our experiments due to technical problems. But we believe that the lateral giant axons would display the same change as that of the median giant axon measured by Goldman as in Fig. 7.1 [118].

The neurons were found to run helix coiled in the nerve [118]. Therefore, in Fig. 7.6, the increase at the beginning until the length of the nerve increased about $0.7L_0$ was due to the uncoiling of membrane folds, such that the nerve impulse in fact traveled a shorter distance before reaching the recording electrodes. And the decrease at the end of stretching was due to the damage of nerve tissues close to deformation. From $L - L_0 = 0.7L_0$, until right before the deformation of the nerve, the diameter should be decreasing. If this is the case, the conduction velocity in the lateral giant axons is independent on the diameter change, similar as that for the median giant axon.

Martin [121] and Hodgkin [109] independently proposed explanations for this independence of the conduction velocity on the axon diameter as the stretch being taken up by the smoothing of membrane folds. However, Goldman observed that the diameter of the neuron fiber decreased after being stretched one time longer than the initial value. Thus the smoothing cannot account for the results in Goldman's data as well as ours.

However, in the framework of the Soliton model, the nerve impulse is considered as a solitary sound wave traveling in the nerve membrane. The speed of sound is determined by the elastic constant and the density of the medium. Upon stretching the nerve, the nerve becomes longer, such that the longitudinal spacing between two adjacent lipid molecules increases. At the same time, the cross-sectional area of the membrane cylinder decreases, resulting in the crowding lipid molecules. Since the lipid membrane is in a fluid phase, the lipid molecules would reorganize around to maintain the structure of the nerve membrane. Thus, the properties of lipid membranes, the elastic modulus of the lipid membranes and the spacing between the molecules (density) are maintained. Therefore, the speed of sound would not change as long as the nerve membrane is allowed to equilibrate.

7.4 Summary

The diameter dependence of the conduction velocity of the lateral giant axons was studied with the nerve stretched. It displays three different features at various stretch lengths.

• Before the nerve is stretched about one time longer than the resting length, the conduction velocity increased with a increasing length. This is because of the uncoiling of the membrane inside the nerve, such that the actual distance the nerve impulse traveled in the nerve is shorter before arriving at a fixed pair of

recording electrodes.
• After the nerve is stretched more than one time longer than the resting length, the conduction velocity stays constant for over one time of the resting length, when the diameter of nerves in the ventral cord of earthworm starts to decrease.
• Shortly before the deformation of the nerve, the conduction velocity falls quickly due to the damage to the nerve by stretching.

The results are consistent with those reported by Bullock and Goldman [117, 118, 119]. The fact that the velocity stays constant with a decrease in the fiber diameter over an appreciable range can be explained by the Soliton Model.

Chapter 8

Measurement of Magnetic Field Generated by a Nerve Impulse with a Ultra-sensitive Atomic Magnetometer

8.1 Backgroud

As discussed in Chapter 1, the work performed on a system can take the form of mechanical energy, electrical energy, magnetic energy and etc.

$$dW = -pdV(-fdl - \Pi dA + HdM + \Psi dq + \sum_i \mu_i dn_i) \tag{8.1}$$

In the context of nerve impulses, the most widely studied feature is the electrical property (Ψdq term), which is also the main method adopted in the preceding chapters. This chapter deals with the measurement of magnetic field (HdM) term.

Magnetic field generated by a nerve impulse is first detected by Wikswo et al. [122] with a SQUID (Superconducting Quantum Interference Device) magnetometer. After that, Wikswo and his colleagues investigated the magnetic field generated by excitable tissues in a great detail both experimentally and theoretically [123, 124, 125]. The SQUID magnetometer consists of a toroidal pickup coil surrounding the nerve, a large transfer coil and the SQUID magnetometer in a cylindrical Dewar vessel with its pickup coil cryogenically-cooled by liquid helium. The experimental system is schematically shown in Fig. 8.1. This method has already been used in biomedical applications like the one shown in Fig. 8.2 [126]. With this technique, the nerve under study has to be exposed and go through the center of pickup coil for the measurement, and the magnetometer needs to work in cryogenic medium.

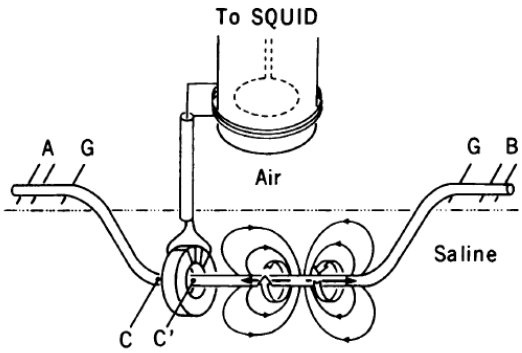

Figure 8.1: Schematic illustration of the measurement of magnetic field from a nerve by SQUID magnetometer. A, B, C and G are electrodes for stimulation and electrical recording. The wide and narrow arrows around the nerve represent the magnetic and electric field, respectively. The toroidal pickup coil around the nerve is connected to a large transfer coil around the cylindrical Dewar vessel in the air. The SQUID magnetometer and its pickup coil (indicated by dashed lines) are inside the cylinder and surrounded by liquid helium. Figure taken from [122].

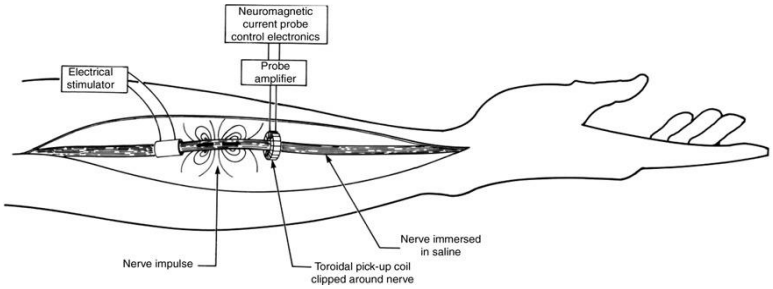

Figure 8.2: Schematic illustration of the neuromagnetic current probe used in clinical settings. The nerve is exposed and the magnetic field from nerve impulses is detected by the pickup coil surrounding the nerve. Figure taken from [126].

With the development of optical magnetometers, it becomes possible to detect the magnetic field with a sensor placed close to the nerve and for the magnetometer to work at room temperature or physiological temperature. Recently, the detection of magnetic field from a nerve impulse with a magnetometer based on Nitrogen-Vacancy centers in diamond has been reported [127]. Due to the limitation of the sensitivity, such magnetometers are promising for applications with the magnetometer placed at micrometer distance or closer to the biological excitable tissues. In this chapter, we apply an optical atomic magnetometer for the measurement of the magnetic field generated by a nerve impulse millimeters away from the sample. The work is in collaboration with the QUANTOP group from the Niles Bohr Institute, University of Copenhagen.

8.2 Materials and Methods

8.2.1 Magnetometer

Cesium Atom

The resonant medium of the magnetometer is a vapour of Cesium (Cs) atoms in a glass cell. Cs has 55 electrons, only one of which is in the outermost shell

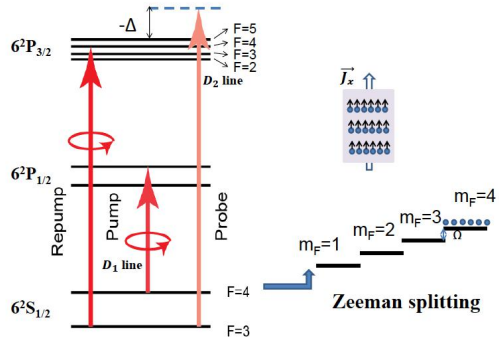

Figure 8.3: The hyperfine structure of cesium. Before measurements all the atoms are pumped into the $F = 4, m_F = 4$ state, with orientation along x. The magnetic field leads to a splitting of the magnetic sublevels by the Lamor frequency Ω. Figure taken from [128].

($n = 6$, with n being the principal quantum number). Due to the interaction between the magnetic moment of the nucleus and the magnetic field generated by the total angular momentum of the electron, the ground state is split into two hyperfine-structure components, characterized by the total angular momentum $\mathbf{F}$. For the ground state of the cesium atom, $\mathbf{F}$ can take two values, i.e. $F = 3$ or $F = 4$. The total angular momentum of the atom can have different x-projection values, with magnetic quantum number $m_F = -F, \ldots, F$. In the presence of a weak external magnetic field along the x-direction (we call it bias field hereafter), $\mathbf{B_x}$, the magnetic sublevels (m_F) split into a ladder of equally spaced levels. The positive ones are shown in Fig. 8.3.

Before taking measurements, all the atoms are prepared by optical pumping into $F = 4$, $m_F = 4$ ground state with the spin orientation along the x-direction. Transitions such as those between $m_F = 3$ and $m_F = 4$ sublevels can be driven by an oscillating magnetic field. The frequency of this oscillating field is called Lamor frequency Ω.

Vapor Cell

The sensitivity of atomic magnetometers is given by [129]

$$\delta B \simeq \frac{1}{g\mu_B} \frac{\hbar}{\sqrt{N\tau T}} \tag{8.2}$$

where μ_B is the Bohr magneton, g is the ground-state Landé factor, $\hbar$ is Planck's constant, T is the time for a magnetic-field measurement, and N is the number of ensemble atoms with coherence time τ. The term $g\mu_B$ is the magnetic moment of the atoms. Consequently, if one wants to improve the sensitivity of an atomic magnetometer, the number of atoms in the system and their spin-relaxation time should be maximized.

Cesium is chosen because it has a high vapor pressure, and thus high sensitivity can be achieved at room temperature or human body temperature. At a room temperature of 22 ℃, the density of cesium atomic is 3.1×10^{16} m^{-3}, which is the highest among all elements appropriate for atomic magnetometry.

If the atoms hit the bare glass wall of the cell, the quantum state will relax back to the ground state. Therefore, the vapor cell is coated with a layer of anti-relaxation alkane coating to preserve the quantum state of the atoms upon collision with the glass. The coating has low adsorption energy for atoms, and thus they spend less time bound to the surface of the cell. Consequently a high spin-relaxation time can be achieved.

The vapor cell used in the measurements is a glass cell which is shown in Fig. 8.4. It contains a channel inside that has a rectangular shape with a size of 1.0 mm × 1.0 mm × 7.7 mm. The cesium vapor is in this channel. The center of the channel to the outer surface of the rectangular cell is less than 1 mm. The average distance between the nerve and the atoms is then a few millimeters, close to a typical distance for many medical applications.

Figure 8.4: A picture of the glass vapor cell. The rectangular channel where the cesium vapor was hold has dimensions of 1.0 mm × 1.0 mm × 7.7 mm and is shown on the top of the picture. The channel is connected to a tube with solid cesium via a tiny hole of a micrometer size. The picture is provided by Hans Christian Stærkind from the Quantop group, NBI Copenhagen.

8.2.2 Principles of Measurements

Larmor Precession

Atoms have internal magnetic moments with angular momentum. When they are exposed to an external magnetic field, the magnetic field exerts a torque on the magnetic moment of the atoms.

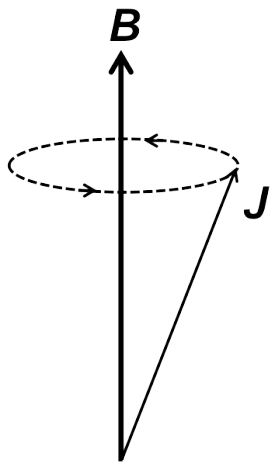

Figure 8.5: Schematic illustration of Larmor precession. **B** is an external magnetic field, **J** is the magnetic moment of the atoms. When the magnetic moment is exposed to an external magnetic field, it begins to precess around the external field.

$$\vec{\tau} = \vec{\mu} \times \vec{B} = \gamma \vec{J} \times \vec{B} \tag{8.3}$$

where $\vec{\tau}$ is the torque (different from that in Eq. 8.2), $\vec{\mu}$ is the magnetic dipole moment, $\vec{J}$ is the angular momentum vector, $\vec{B}$ is the external magnetic field, and γ is the gyromagnetic ratio. The angular momentum vector $\vec{J}$ precesses about the external field axis with an angular frequency called the Larmor frequency ω.

$$\omega = -\gamma B \tag{8.4}$$

This precession is called Larmor Precession.

Experimental System

We define a 3D coordinate to system as shown in Fig. 8.6. The plane parallel to the glass cell is the y–z plane. The direction vertical to y–z plane, which is the direction of the Bias field (B_x) is x direction. All the atoms are initially pumped into the $F = 4, m_F = 4$ state, with orientation along x. The axial current in the nerve close to the cell creates a magnetic field in the y direction, transverse to the initial spin J_x. Therefore, it creates a transverse component of the external magnetic field. The atoms will then do a Larmor precession in the y–z plane. The J_z spin component is detected optically by measuring the polarization rotation

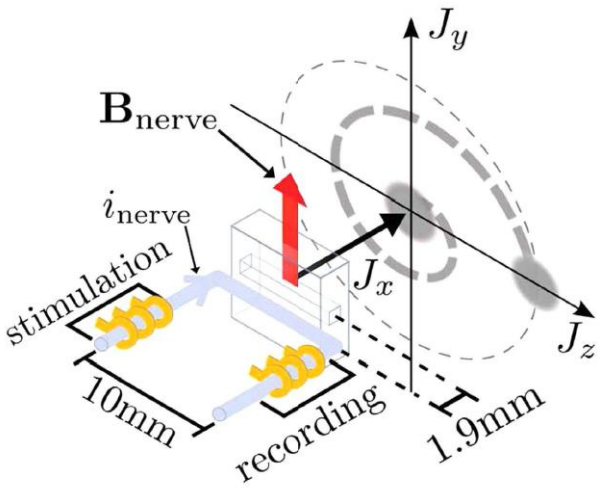

Figure 8.6: Schematic illustration of the measurement system. A 3D coordinate is assigned to the system as shown in the drawing. The cesium cell is parallel to the y–z plane. The atoms are initially pumped to the x direction. The nerve chamber is in the x–z plane with gold electrodes at the two sides. The nerve is pulled in the nerve chamber (shown as blue tube in the figure) in a U-shape manner with the middle part placed close to the atomic cell. The gold electrodes surround the nerve with gentle touch. The axial current of a nerve impulse generates a magnetic field in the y direction which will initiate the Larmor precession of atoms in the y–z plane. The distance between the nerve and the center of the atomic cell is about 1.9 mm. Figure from [70].

of linearly polarized probe light passing through the vapor cell using a balanced polarimeter.

Relaxation Time $\mathbf{T_1}$ and $\mathbf{T_2}$

With optical pumping, the atoms are prepared into the $|F, m_F\rangle = |4, 4\rangle$ ground state. Although the alkane coating significantly prevents the atoms from relaxation, it can not be totally avoided. After some time, the state of the atoms will go back to the equilibrium state. The collision between the cell wall and atoms is inelastic collision, if this happens with a rate of γ_{ic}, the decay of total spin of the ensemble of atoms decay is expected to be

$$J_x(t) = J_x(0)e^{-\gamma_{ic}t} \tag{8.5}$$

with a characteristic time T_1 with

$$\frac{1}{T_1} = \gamma_{ic} \tag{8.6}$$

Taking into account the coherence between $|F, m_F\rangle = |4, 3\rangle$ and $|F, m_F\rangle = |4, 4\rangle$, the inelastic collisions affect both states equally. Whereas, the elastic collisions between the atoms contribute to the decoherence between the two states

without affecting each populations. If the elastic collisions happen at a rate of γ_{ec}, the resulting spin coherence time T_2 should take the following form

$$\frac{1}{T_2} = \gamma_{ic} + \gamma_{ec} = \frac{1}{T_1} + \gamma_{ec} \tag{8.7}$$

From Eq. 8.7, it follows that $T_2 \leq T_1$. Therefore, in the experiments, we always use T_2 as the characteristic time for the atoms. For the vapor cell we used T_2 is 27 ms, which is much longer than the duration of a typical nerve impulse $\sim$ 1–2 ms. This means that the vapor cell is sufficient for measuring the magnetic field generated by the nerve far before the relaxation and decoherence of atoms happen.

8.2.3 Nerve and Electrical Measurement

Frog Sciatic Nerve

The nerve used in the measurements was the frog sciatic nerve from green frogs (Rana Esculenta). Frogs were decapitated and the sciatic nerves were isolated from the spine down to the knee. Nerves in frog legs are schematically shown in Fig. 8.7 (a). The length of the separated nerve is 7-8 cm, and the diameter is about 1.3 mm in the proximal end and slightly thinner in the distal end. The

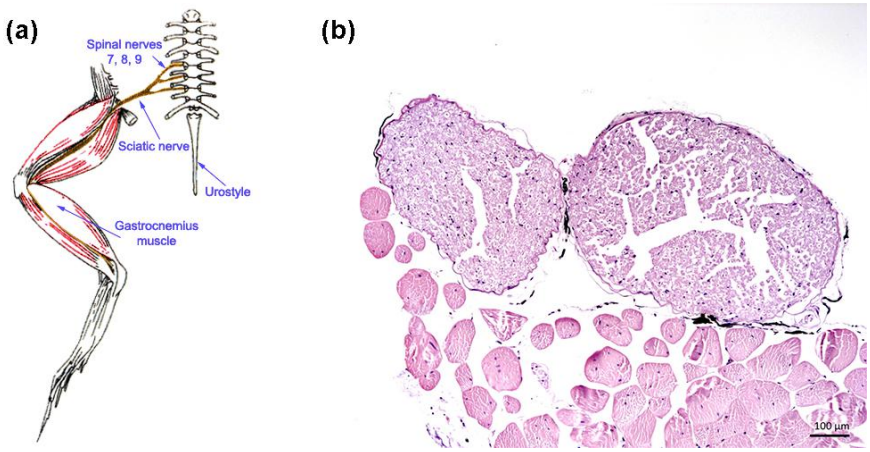

Figure 8.7: (a) Schematic drawing of frog nerves in a leg connected with the spine [130]. (b) the cross section of a frog sciatic nerve after the first division taken with an electron microscope. Two nerve bundles are surrounded by a fascia of connective tissue. The diameters of the two nerve bundles are 0.59 mm and 0.44 mm and they contain 1750 and 950 single axons respectively with a minimal diameter of 7 µm. The average diameter of individual myelinated nerve fibers is 16 µm. [70]

sciatic nerves from frogs are a bundle of small axons held together at the proximal end, which divide into three bundles at the distal end. Fig. 8.7 (b) shows the cross section of the nerve bundle containing thousands of axons taken with an electron microscope. The diameters of the axons are similar.

Electrical Recording

The action potential is recorded extracellularly with a chamber shown in Fig. 8.8

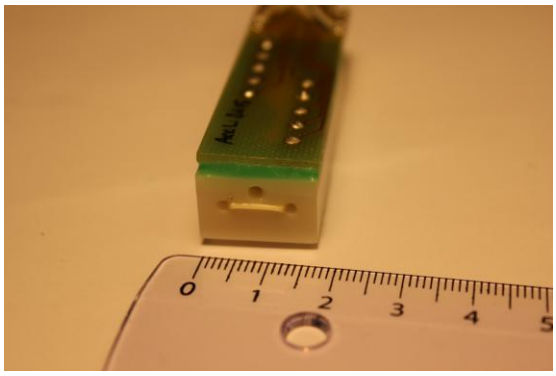

Figure 8.8: The nerve 3D printed nerve chamber with a frog sciatic nerve inside. The front part where the nerve is exposed is placed close to the atomic cell.

Two separated cylindrical channels with a diameter of 2 mm are included in a 3D printed rectangular chamber. The chamber has dimensions of 47 mm × 18 mm × 8.5 mm. The nerve was tied by threads on the two sides. Each side was attached to a thin copper wire, which guided the nerve through each channel in a U-shape manner. The front part of the nerve was exposed and placed close to the magnetometer.

After the nerve was well positioned in the chamber, the front area where the nerve was exposed was treated with several drops of saline solution, and subsequently covered by a thin coverslip (0.13 mm thick), so that the nerve was kept in an environment with saturated water vapor. Under this condition, the nerve could stay alive during the measurements for a couple of hours. Gold electrodes surround the nerve with gentle touch. The distance between two gold electrodes is 3 mm. The electrodes on the stimulation side are far away from the front (optical detection area), which allows the nerve impulse to travel for a certain time before arriving at the optical recording site, so that the recorded optical signal is temporally separated from the stimulation artifact. On the recording side, the electrodes are close to the front (optical detection area), so that the recording signal to the most possible extent represents the electrical signal of the nerve being optically recorded.

Electrical connections are integrated on the back of the chamber. Cables on the stimulation side are connected to a function generator which sends out a biphasic pulse stimulation with a duration of 50 µs. Cables on the recording side are connected to a preamplifier and then a data acquisition system. Three electrodes were used on each side in the measurement for differential voltage stimulation and ground; differential recording and ground, respectively. The nerve was stimulated at the proximal end and the electrical signal was recorded

at the distal end. The electrical signal was amplified 10 times, filtered with 3 kHz low pass filter and 10 Hz high pass filter, and recorded simultaneously with the magnetic field recordings.

8.2.4 Operation of Magnetometer

The magnetometer can be operated in two modes, i.e. pulsed mode and continuous mode, which were both applied to measure the magnetic field generated by a nerve impulse. The names 'pulsed' and 'continuous' refer to the state of lasers during the experiments. The details will be described in the following sections.

Pulsed Mode

In the pulsed mode, pumps and probe lasers were applied as pulses in two successive sequences in each measurement. The pulse sequence is shown in Fig. 8.9. In the first part, a pulse of pump and repump lasers were first applied to prepare

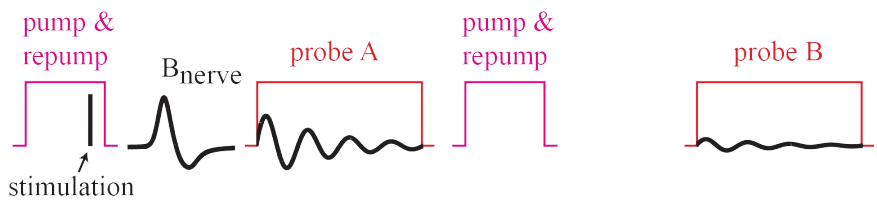

Figure 8.9: Pulse sequence in the pulsed measurement. The pump and repump are first turned on for 7 ms, during which the electrical stimulation was sent out at t = 5.8 ms. The electrical stimulation initiates an action potential which arrives at the optical detection area at about t = 7.2 ms. The probe light was turned on at t = 12 ms for 42 ms to detect the spin of cesium atoms. The sequence of the pump, repump and probe lights was repeated once again without electrical stimulation. Picture from [70].

the spin of Cs atoms along x-direction. The electrical stimulation was started inside this period. The starting time of electrical stimulation was adjusted such that the change of atomic spin due to the stimulation artifact can be damped by pumps before the arrival of the nerve signal. The electrical stimulation initiated a nerve impulse, which would then arrive at the detection area. The duration of pump pulse were adjusted such that they were turned off before the arrival of a nerve impulse. Finally the spins were detected with a pulse of probe light. The sequence was then repeated once without electrical stimulation, so that the background optical signal was recorded. The optical signal from the second measurement was then subtracted from the first part to extract the optical signal from the nerve impulse. Each measurement was taken 1000 times and averaged.

With measurements in this mode, the total magnetic field acting on the atomic spin was detected. It was first done in the experiments to determine whether there was an optical signal or not. The Fourier component of probe oscillations at the

Larmor frequency $|\tilde{B}(\Omega)|$ was detected.

$$|\tilde{B}(\Omega_L)| = C \cdot |\tilde{U}(\Omega_L)| \tag{8.8}$$

where $U(\Omega_L)$ is the voltage signal from the detector when the probe is on and C is a constant.

In the measurements, the electrical signal was first detected and Fourier transformed to get the frequency with a maximum response. The bias field was then adjusted to set the Larmor frequency to this value before optical measurements, so that the oscillating magnetic field generated by the nerve impulse can drive the transition between $|F, m_F\rangle = |4, 4\rangle$ and $|F, m_F\rangle = |4, 3\rangle$ energy levels. The recorded optical signal was again Fourier transformed, and the response at the Larmor frequency was recorded. The constant C in Eq. 8.8 was determined by calibration with a known magnetic field generated by a RF coil.

Continuous Mode

In the continuous mode, pump and probe lasers were applied all the time over the measurement process. The magnetic field was measured as a function of time.

8.3 Results and Discussions

8.3.1 Electrical Recording

Fig. 8.10 shows typical electrical recordings. The left figure shows a typical trace

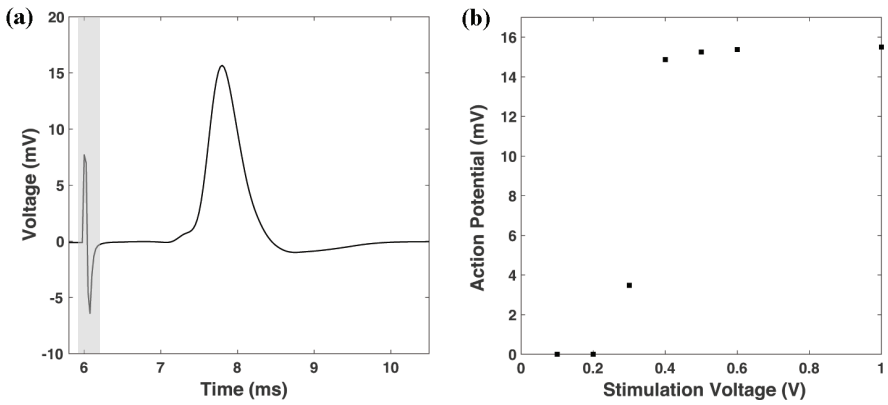

Figure 8.10: Electrical signal measured from the frog nerve. (a) the action potential recorded extracellularly as a function of time. The sharp peak in the gray area is the stimulation artifact. (b) the peak amplitude as a function of the stimulation voltage, which displays a step manner.

of action potential measured by extracellular recording. The signal was amplified 10 times. The peak at around 6 ms in the gray area is the stimulation artifact, which increases linearly with stimulation voltage. The action potential starts at

about 7.2 ms, and lasts for 2 – 3 ms. The amplitude of the action potential has a stepwise dependence on the stimulation voltages and saturates above a threshold, as shown in Fig. 8.10 (b). This was taken as a reference whether we detected an optical signal from the nerve impulse or from the stimulation artifact. If the optical response is linearly dependent on stimulation voltage, the signal should come from the stimulation artifact, while if the dependence is stepwise, it should come from the nerve impulse.

Since the electrical signal from the nerve is recorded as the voltage difference between the two recording electrodes separated by a distance of 3 mm, much smaller than the length of an action potential, the recorded signal can be considered corresponding to the time-derivative of the actual action potential. Thus, when the signal crosses the time axis, it corresponds to the peak of the actual action potential. If we take the time delay between this point and the starting of the stimulation as the time it traveled (Δt), divided by the distance between the stimulation and recording electrodes (Δs), the conduction velocity can be calculated with $v = \Delta s/\Delta t$ to be around 30 m/s.

8.3.2 Pulsed Mode

The Larmor frequency was set to 410 Hz according to the Fourier transform of the electrically recorded action potential. In the pulsed mode, the Fourier component $|\tilde{B}(\Omega_L)|$ of the nerve signal was determined using Eq. 8.8. The oscillation and relaxation of the atomic spin is shown in Fig. 8.11 (a), which was Fourier transformed to get the spectrum in Fig. 8.11 (b). The value of $U(\tilde{\Omega}_L)$ at 410 Hz

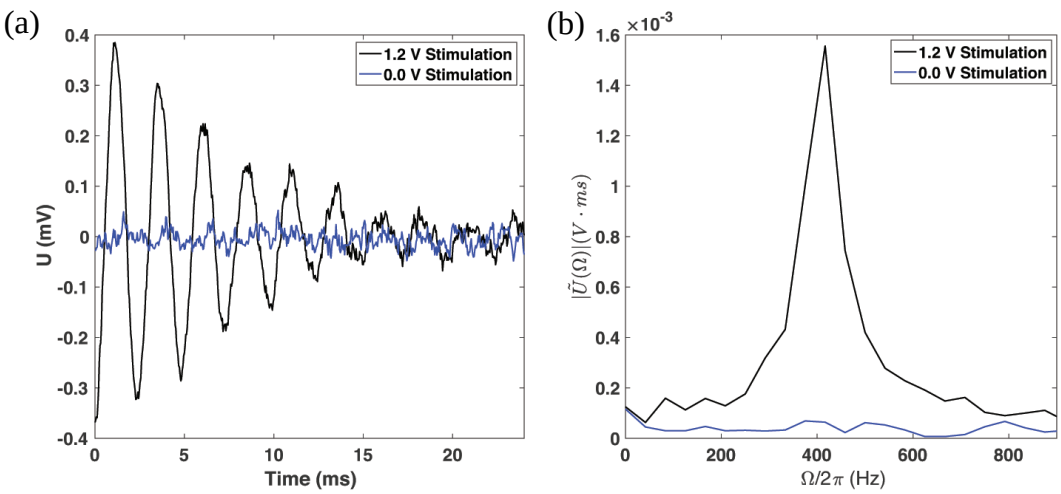

Figure 8.11: (a) The optical signal recorded in the pulsed mode at 0 and 1.2 V stimulation. (b) The signal Fourier transformed from (a). The plots from optical recordings are made with the scripts kindly shared by Hans Christian Stærkind from the Quantop group, NBI Copenhagen.

was taken and used to calculate $|\tilde{B}(\Omega_L)|$ according to Eq. 8.8. The measurement

was done for different stimulation voltages. The voltage dependence of magnetic field is shown in Fig. 8.12.

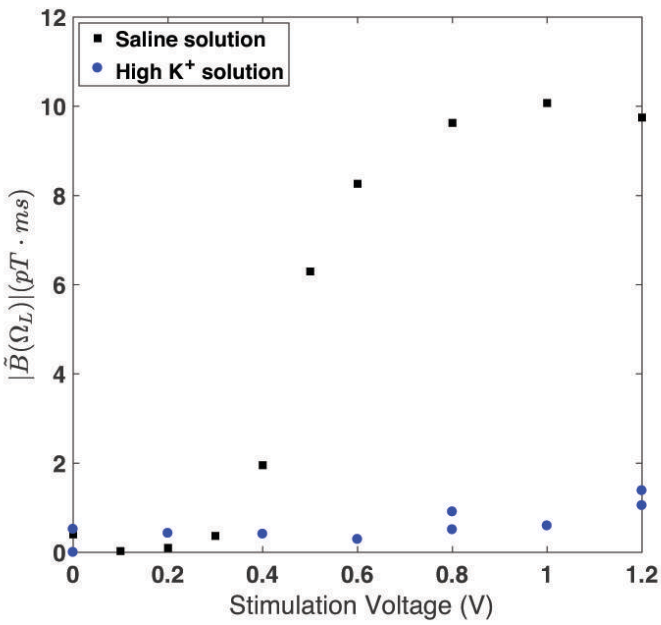

Figure 8.12: The Fourier component of magnetic field at the Larmor frequency measured in the pulsed mode as a function of stimulation voltage. The black square show the magnetic field from the nerve impulse. The blue dots show the magnetic field measured after the nerve was treated to a high K^+ concentration saline solution.

It displays a stepwise dependence on stimulation voltages, which is similar to that of the electrical recordings. This confirms that the magnetic field measured originated from the nerve impulse instead of the stimulation artifact which increases linearly with stimulation voltage.

The nerve was later treated with the high K^+ concentration saline solution to suppress the action potential. Under high K^+ concentration, the action potential is blocked at all stimulation voltages. The optical signal was then detected and plotted in Fig. 8.12 in blue dots. One can see that the optical signal was also suppressed. This further confirms that we measured the magnetic field generated from the nerve impulse.

The nerve was then moved away from the vapor cell in controlled distance steps as shown in Fig. 8.13. The magnetic field recorded as a function of distance was recorded and shown in Fig. 8.13. The closest possible distance between the nerve and vapor cell was taken as zero distance. The magnetic field decreases with increasing distance between the nerve and the vapor cell. A predominant magnetic field signal (compared to the noise at 0 V stimulation, shown as blue dots in Fig. 8.13) can be detected until the nerve was moved away for about 5 mm.

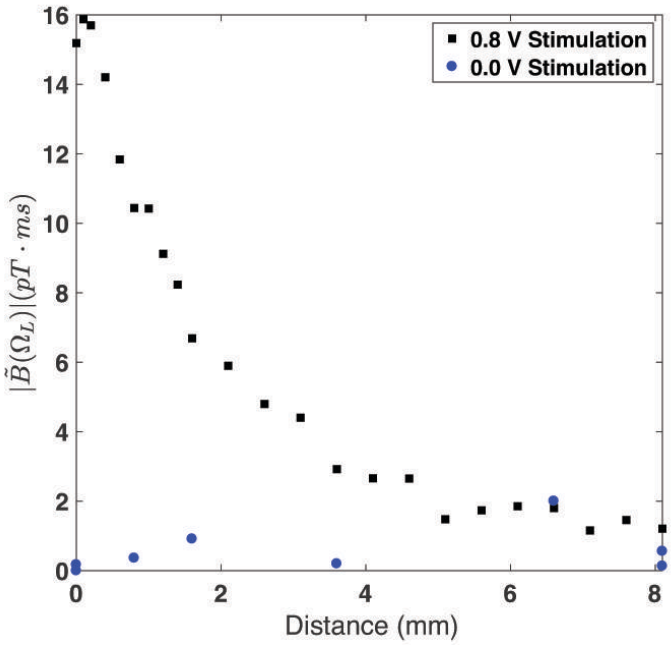

Figure 8.13: The Fourier component of the magnetic field generated by the nerve impulse at the Larmor frequency as a function of the distance between the nerve and the vapor cell. Black squares show the magnetic field with a stimulation of 0.8 V, at which the nerve signal was saturated. The blue dots show the magnetic field when the voltage simulation was turned off.

8.3.3 Continuous Mode

In the continuous mode, the pump and probe lasers were continuously on. The magnetic field from the nerve impulse was measured as a function of time. Fig. 8.14 shows the electrical (a) and optical recording (b) taken simultaneously at different stimulation voltages. There are two features in both electrical and optical signals. The stimulation artifacts in the gray area start at around 6 ms and increase linearly with stimulation voltage. The other parts of the signals which saturate after a certain threshold originate from the nerve impulse. The recorded electrical signal starts later than the optical signal, as the electrical recording electrodes were placed after the optical detection area.

The optical signal is a convolution of the magnetic field from the nerve impulse and the response function of the measurement system. Thus we do a deconvolution and a low pass filtering (cut-off frequency 1200 Hz) to get the time-dependent magnetic field profile as shown in Fig. 8.15.

The peak-to-peak amplitude of the magnetic field from the nerve impulse can be calculated to be about 20 pT. This magnitude of magnetic field from the nerve impulse is smaller than that from what Wikswo et al. measured due to the cancellation of the current on the two sides of the nerve membrane, which will be explain in the following. The axial current from a nerve impulse in a

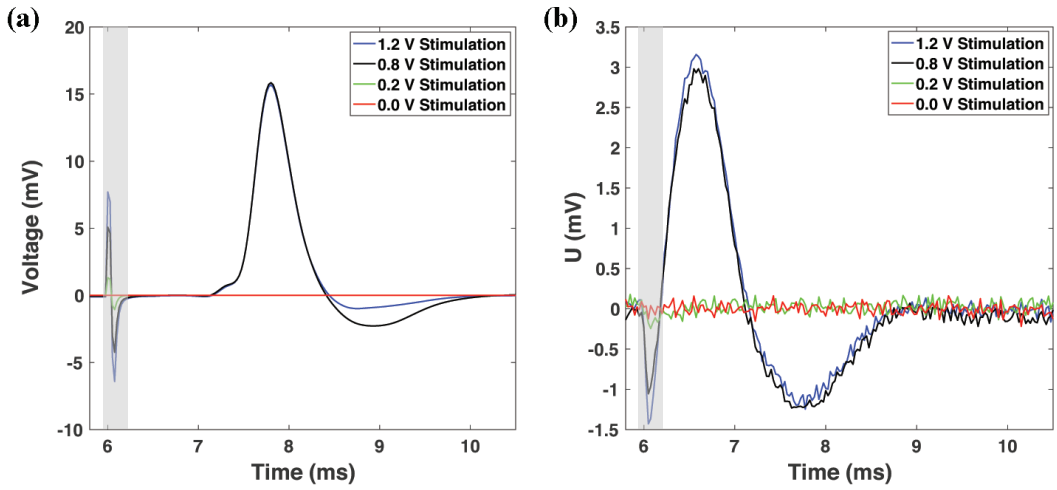

Figure 8.14: (a) Electrical action potential traces at different stimulation voltages, for comparison with the optical signal. (b) the optical signal recorded in the continuous measurement simultaneously taken with the electrical action potential.

nerve cylinder has a distribution as shown in Fig. 8.16. At the position where the impulse propagates, there are currents on the two sides of the membrane with opposite directions which creates a local canceling effect of the axial current. Wikswo et al. detected the magnetic field from frog sciatic nerve with SQUID magnetometer [122], which contained a pickup coil surrounding the nerve. Since it was close enough to the nerve, most of the current on the outside of the nerve was not picked up. Therefore, it reduced the canceling effect to a great extent. In addition, the coil picked up the signals from all directions around the nerve which added up to a value of magnetic field detected. Whereas, in our measurement, the vapor cell was close to one side of the nerve with a distance of several millimeters, the magnetic field detected was much smaller. However, with the high sensitivity of our magnetometer, we measured a reasonable magnetic signal from the nerve impulse in a configuration better for medical use.

The frog sciatic nerve contains thousands of axons inside. If we make a simple model by considering the average current is in the middle of the bundle, the axial current can be calculated from the magnetic field measured in our experiments. The magnetic field from an infinitely long cable is

$$|B| = \frac{\mu_0 I}{2\pi r} \tag{8.9}$$

The current is then calculated to be $I = 2\pi r B/\mu_0 \approx 0.23$ µA.

8.4 Summary

The magnetic field generated by the axial current from a nerve impulse was measured with a sensitive atomic magnetometer in two modes, pulsed mode and

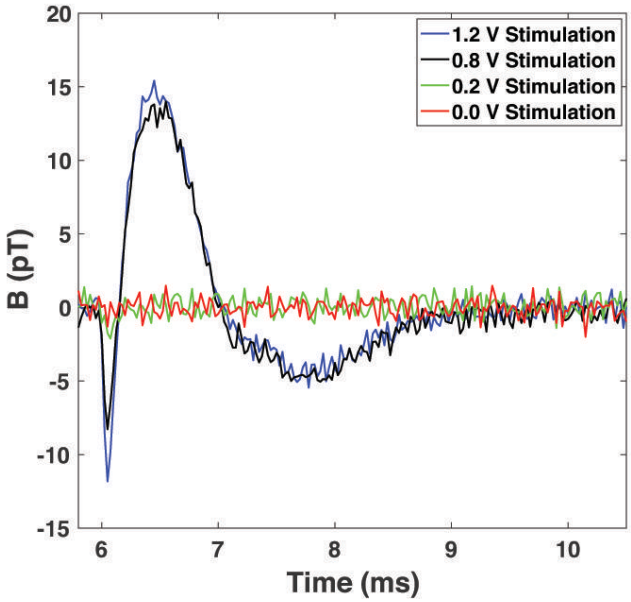

Figure 8.15: The magnetic field profiles as a function of time calculated from a deconvolution of the optical signal from the continuous measurement. The profiles at four different stimulation voltages are plotted.

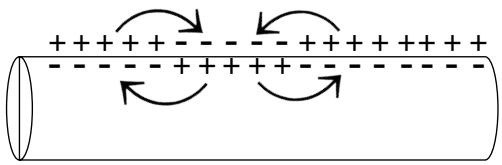

Figure 8.16: The axial current distribution on a nerve membrane where the nerve impulse propagates. Arrows indicate the direction of currents on each site.

continuous mode.

In the pulsed mode, the Fourier component at the Larmor frequency of the magnetic field was detected. It displays a stepwise dependence on the increasing stimulation voltage, similar to that of the electrical response. The magnetic field can be measured with a distance between the nerve and the magnetometer up to about 5 mm.

In the continuous mode, the magnetic field was measured as a function of time. The temporal profile have similar features with the electrical profile. The peak-to-peak value of the magnetic field measured was about 20 pT.

Chapter 9

Conclusions and Outlook

9.1 Conclusions

This thesis consists of several topics with shared motivation of studying the nerve impulse from a thermodynamic perspective, including

1) the collision of two nerve impulses traveling in opposite directions towards each other was studied. We found that they can penetrate each other upon collision and continue propagating with minor changes in their shapes. This result holds when measurements were done with the nerve both in large and small amount of physiological solutions. The presence of ganglia (cluster of cell bodies) does not make a appreciable difference with respect to the outcome.

Two electrode configurations were tried, i.e. with the recording electrodes in the middle of two pairs of stimulation electrodes and at one end of them (as Berg et al. adopted). In the first case, action potentials from both sides could be detected by the recording electrodes; while in the second case, only the action potential from a closer stimulation can be detected. The second configuration did not test directly whether the impulses penetrated each other or annihilated, but rather demonstrates that a nerve impulse cannot pass a highly-perturbed region with a high voltage stimulation. This was found to be valid when both electrode configurations were adopted in the same measurement.

The perturbation explanation was tested with the refractory period measurements. The region where a high voltage stimulation was applied has a significantly longer refractory period than the region where a nerve impulse passed, which confirms the perturbation speculation to some extent.

2) Attempts were made to study the temperature change during an action potential and an oscillating Briggs-Rauscher (BR) reaction, which share the feature of a adiabatic reversible process. The temperature change during an action potential was difficult to measure due to technical problems. However, we managed to measure the temperature oscillation, as well as the oscillation in I^- concentration in the BR reaction. The oscillation in temperature and substances in such a process can be well described by linear non-equilibrium thermodynamics.

3) Local anesthetic effect was investigated with nerves of lobsters and earthworms. For compound action potentials, local anesthetic lidocaine causes a shift in stimulation threshold, as well as a decrease both in conduction velocity and the peak amplitude. While for an action potential, lidocaine causes a shift of stimulation threshold, and a decrease in the conduction velocity, but the peak amplitude stay largely unchanged within experimental errors. The threshold shift can be more than 2.5 folds.

4) The dependence of conduction velocity on the diameter of the nerve was studied with the ventral cord of earthworm being stretched. Upon stretching, the diameter of the nerves would decrease. The conduction velocity in the lateral giant axons was found to increase firstly, then to be constant over a long range of stretching, and finally to decrease rapidly before the deformation of the nerve. The initial increase was due to the uncoiling of nerves inside the ventral cord, and the decrease at the end was due to damage in nerve tissues. The conduction velocity shows appreciable independence of the fiber diameter.

The above conclusions can be well predicted and explained by the Soliton model, which describes a nerve impulse as a localized density pulse resembling solitons that travel at a constant velocity without distortions in the shape.

5) The magnetic field generated by the nerve impulse was detected with an ultra-sensitive atomic magnetometer. The measurement was performed in two operating modes, i.e. the pulsed mode and the continuous mode. In the pulsed mode, the Fourier component of a nerve impulse was detected, which confirmed that there was a magnetic field from the nerve impulse that can be detected by our system. In the continuous mode, the temporal shape of the magnetic field from the nerve impulse was detected, which displayed similar features with the electrically recorded action potential along with the optical measurement. The magnetic field was measured to be around 20 pT, corresponding to a longitudinal current of 0.23 µA by a rough calculation. The measurement can be performed with a distance between the nerve and the sensor of magnetometer to be over 5 mm, providing a promising technique in the medical applications.

9.2 Outlook

The experiments in the thesis were conducted in an indirect manner as we measured the action potential on nerve bundles with extracellular recording, which is sort of an indirect method. To directly verify a certain prediction, all the above mentioned topics would ideally be conducted on a single neuron. The giant axons from lobster cumoesophageal connectives have a diameter of around 100 µm, which is a good option available around the year. For a single axon, it is more applicable to do an intracellular recording with a patch-clamp amplifier. This has been tried in the last few months of this project.

Furthermore, an action potential can be detected by fluorescence microscopes

with the nerve marked with voltage-sensitive fluorescence markers. This would be a good approach for a virtual demonstration of the collision experiments. An improvement of the anesthetic experiments could be monitoring the diffusion of anesthetics, to confirm that the anesthetics are actually in the membranes of the nerve. Besides, it may be interesting to study the difference in the effect of anesthetics on the cell body of a nerve and on the axon of a nerve. It seems in the experiments, when there are ganglia, the anesthetic effect is faster than those without ganglia.

For the temperature measurement on nerves, the main problem with coating process in the heat measurement of nerve impulse is that the coating must be able to tolerate an electrical breakdown, as well as a saline solution with rather high concentrations of ions without being too thick. The following two approaches may be considered:

• As polymers would mostly change their structures and properties when exposed to high concentration salt solutions along with an electric field when they appear as a very thin layer, one can consider first applying a layer of those polymer conformal coating, and subsequently coat a layer of metal such as gold or aluminum on top. The metal layer is compact such that it would effectively protect the chip from saline solutions without losing too much thermal sensitivity and time resolution. And the conformal coating layer would be much more effective in electrical insulation without being exposed to salt solutions.

• Thermal conduction is driven by microscopic collisions of particles and the movement of electrons within a body. Metals are good thermal conductors because of freely moving electrons. Another group of good heat conductor but electrically insulator is inorganic crystal due to the lattice vibration, such as diamond. One might consider such materials as a solution in the case of heat measurement.

Note that a strong adhesion between the coating material and the thermochip is important. It might help to pre-process the chip before applying coating materials. However, this requires that the elements on the thermal chip should be inert to any chemicals in the pre-processing, which needs to be tested before operation.

Apart from improvement for the work presented in this thesis, the Soliton model assumes that the nerve membrane goes through a phase transition from a fluid phase to a gel phase, and subsequently goes back to the fluid phase. We have been trying to detect this phase transition during a nerve impulse with two-photon excitation fluorescence microscopy with the nerve membrane labeled by phase sensitive markers. It will be rather meaningful if this kind of measurement would lead to positive results. In general, there is still a long way for the Soliton model to be widely accepted, which calls for more work to be done in the future.

Bibliography

[1] F.E.A. Martini. *Anatomy and Physiology 2007 Ed.* Rex Bookstore, Inc., 2007.

[2] Harvey Lodish, Arnold Berk, Chris A. Kaiser, Monty Krieger, and Matthew Scott. *Molecular Cell Biology. 6th edition.* W. H. Freeman, 6th edition edition, 2008.

[3] E. R. Kandel, J. H. Schwartz, T. M. Jessell, S. A. Siegelbaum, and A. J. Hudspeth. *Principles of Neural Science, Fifth Edition.* McGraw-Hill Education, 2012.

[4] A. F. Huxley and R. Stämpfli. Evidence for saltatory conduction in peripheral myelinated nerve fibres. *J. Physiol.*, 108:315–339, 1949.

[5] Ke Xu and Susumu Terakawa. *Myelinated fibers and saltatory conduction in the shrimp.* Springer Japan, 1 edition, 2013.

[6] R. Lipowsky and E. Sackmann, editors. *Structure and Dynamics of Membranes*, volume 1A. 1st edition, June 1995.

[7] B. Tenchov R. Koynova. Transitions between lamellar and non-lamellar phases in membrane lipids and their physiological roles. *OA Biochemistry*, 1(1):9, April 2013.

[8] T. Gulik-Krzywicki E. Rivas F. Reiss-Husson V. Luzzati, A. Tardieu. Structure of the cubic phases of lipid-water systems. *Nature*, 220:485–488, November 1968.

[9] T. Heimburg. *Thermal biophysics of membranes.* WILEY-VCH, July 2007.

[10] D. M. Small M. J. Janiak and G. Graham Shipley. Temperature and compositional dependence of the structure of hydrated dimyristoyl lecithin. *J. Biol. Chem.*, 254(13):6068–6078, July 1979.

[11] D. M. Small M. J. Janiak and G. Graham Shipley. Nature of the thermal pretransition of synthetic phospholipids: Dimyristoyl- and dipalmitoyllecithin. *Biochemistry*, 15(21):4575–4580, 1976.

[12] R. Winter J. Eisenblätter. Pressure effects on the structure and phase behavior of dmpc-gramicidin lipid bilayers: a synchrotron saxs and ^{2}h-nmr spectroscopy study. *Biophys. J.*, 90(3):956–966, February 2006.

[13] N. Murooka S. Kitagawa, N Yokochi. ph-dependence of phase transition of the lipid bilayer of liposomes of stratum corneum lipids. *Int J Pharm*, 126(1-2):49–56, December 1995.

[14] J. Schacht M. G. Ganesan, N. D. Weiner. Effects of calcium and neomycin on phase behavior of phospholipid bilayers. *J Pharm Sci Pharmacol.*, 72(12):1465–1467, 1983.

[15] H. Sasse-Middelhoff K. GræsbØll and T. Heimburg. The thermodynamics of general and local anesthesia. *Biophys. J.Journal*, 106:2143–2156, May 2014.

[16] S. J. Singer and Garth L. Nicolson. The fluid mosaic model of the structure of cell membranes. *Science*, 175(4023):720–731, 1972.

[17] O. G. Mouritsen. Mattress model of lipid-protein interactions in membranes. *Biophys. J*, 46:141–153, August 1984.

[18] D. Johnston and S. M. Wu. *Foundations of Cellular Neurophysiology.* The MIT Press, 1994.

[19] D. E. Goldman. Potential, impedance, and rectification in membranes. *J. Gen. Physiol.*, 27(1):37–60, September 1943.

[20] A. L. Hodgkin and B. Katz. The effect of sodium ions on the electrical activity of the giant axon of the squid. *J. Physiol.*, 108:37–77, 1949.

[21] A. L. Hodgkin, A. F. Huxley, and B. Katz. Measurement of current-voltage relations in the membrane of the giant axon of *Loligo*. *J. Physiol.*, 116:424–448, 1952.

[22] A. L. Hodgkin and A. F. Huxley. Currents carried by sodium and potassium ions through the membrane of the giant axon of *Loligo*. *J. Physiol.*, 116:449–472, 1952.

[23] A. L. Hodgkin and A. F. Huxley. The components of membrane conductance in the giant axon of *Loligo*. *J. Physiol.*, 116:473–496, 1952.

[24] A. L. Hodgkin and A. F. Huxley. The dual effect of membrane of potential on sodium conductance in the giant axon of *Loligo*. *J. Physiol.*, 116:497–506, 1952.

[25] A. L. Hodgkin and A. F. Huxley. A quantitative description of membrane current and its application to conduction and excitation in nerve. *J. Physiol.*, 117:500–544, 1952.

[26] D. A. Doyle, J. M. Cabral, R. A. Pfuetzner, A. Kuo, J. M. Gulbis, S. L. Cohen, B. T. Chait, and R. MacKinnon. The structure of the potassium channel: molecular basis of k^+ conduction and selectivity. *Science*, 280(5360):69–77, 1998.

[27] D. Noble. Applications of hodgkin-huxley equations to excitable tissues. *Physiol. Rev.*, 46(1):1–50, 1966.

[28] F. J. Julian and D. E. Goldman. The effects of mechanical stimulation on some electrical properties of axons. *J Gen Physiol*, 46:297–313, 1962.

[29] D. A. Poulos and R. A. Lende. Response of trigeminal ganglion neurons to thermal stimulation of oral-facial regions. i. steady-state response. *J. Neurophysiol.*, 33(4):508–517, 1970.

[30] D. A. Poulos and R. A. Lende. Response of trigeminal ganglion neurons to thermal stimulation of oral-facial regions. ii. temperature change response. *J Neurophysiol.*, 33(4):518–526, 1970.

[31] M. A. Nokes R. P. Michelson B. C. Hill, E. D. Schubert. Laser interferometer measurement of changes in crayfish axon diameter concurrent with action potential. *Science*, 196:426–428, April 1977.

[32] K. Iwasa, I. Tasaki, and R. C. Gibbons. Swelling of nerve fibers associated with action potentials. *Science*, 210:338–339, 1980.

[33] I. Tasaki and K. Iwasa. Shortening of nerve fibers associated with propagated nerve impulse. *Biochem Biophys Res Commun*, 94(2):716–720, 1980.

[34] I. Tasaki, K. Kusano, and P. M. Byrne. Rapid mechanical and thermal changes in the garfish olfactory nerve associated with a propagated impulse. *Biophys. J.*, 55:1033–1040, 1989.

[35] A. Gonzalez-Perez, L. D. Mosgaard, Budvytyte R, E. Villagran-Vargas, A. D. Jackson, and T. Heimburg. Solitary electromechanical pulses in lobster neurons. *Biophys. Chem.*, 216:51–59, 2016.

[36] I. Tasaki, A. Watanabe, R. Sandlin, and L. Carnay. Changes in fluorescence, turbidity, and birefringence associated with nerve excitation. *Proc Natl Acad Sci*, 61:883–888, 1968.

[37] Bertil Hille L. B. Cohen, R. D. Keynes. Light scattering and birefringence changes during nerve activity. *Nature*, 218:438–441, 1968.

[38] L. B. Cohen and R. D. Keynes. Changes in light scattering associated with the action potential in crab nerves. *J. Physiol.*, 212:259–275, 1971.

[39] B. Hille L. B. Cohen and R. D. Keynes. Changes in axon birefringence during the action potential. *J. Physiol.*, 211:495–515, 1970.

[40] W. N. Ross, Salzberg B. M, L. B. Cohen, and H. V. Davila. A large change in dye absorption during the action potential. *Biophys. J.*, 14:983–986, 1974.

[41] A. Watanabe. Change in optical activity of a lobster nerve associated with excitation. *J. Physiol.*, 389:223–253, 1987.

[42] H. D. Rolleston. On the conditions of temperature in nerves (1) during activity, (2) during the process of dying. *J Physiol.*, 11(3):208–225, 1890.

[43] A. V. Hill and W. Hartree. The four phases of heat-production of muscle. *J Physiol.*, 54(1-2):84–128, 1920.

[44] A. V. Hill. The absence of temperature changes during the transmission of a nervous impulse. *J Physiol.*, 43(6):433–440, 1912.

[45] A. V. Hill. The heat-production and recovery of crustacean nerve. *Proc R Soc of Lon B Biol Sci.*, 105(736):153–176, 1929.

[46] B. C. Abbott, A. V. Hill, and J. V. Howarth. The positive and negative heat production associated with a nerve impulse. *Proc R Soc Lond B Biol Sci*, 148(931):149–187, 1958.

[47] J. V. Howarth, R. D. Keynes, J. M. Ritchie, and A. von Muralt. The heat production associated with the passage of a single impulse in pike olfactory nerve fibres. *J. Physiol.*, 249:349–368, 1975.

[48] I. Tasaki and K. Iwasa. Temperature changes associated with nerve excitation: detection by using polyvinylidene fluoride film. *Biochem Biophys Res Commun*, 101(1):172–176, 1981.

[49] I. Tasaki and P. M. Byrne. Heat production associated with a propagated impulse in bullfrog myelinated nerve fibers. *Jpn. J. Physiol.*, 42:805–813, 1992.

[50] D. Papahadjopoulos, K. Jacobson, NIR S, and T. ISAC. Phase transitions in phospholipid vesicles fluorescence polarization and permeability measurements concerning the effect of temperature and cholesterol. *Biochim Biophys. Acta.*, 311:330–348, 1973.

[51] E. Neher. Single-channel currents recorded from membrane of denervated frog muscle fibres. *Nature*, 260:799–802, 1976.

[52] T. Heimburg A. Blicher. Voltage-gated lipid ion channels. *PLOS ONE*, 8(6):e65707, June 2013.

[53] V. F. Antonov, V. V. Petrov, A. A. Molnar, D. A. Predvoditelev, and A. S. Ivanov. The apperance of single-ion channels in unmodified lipid bilayer membranes at the phase transition temperature. *Nature*, 283:585–586, 1980.

[54] V. F. Antonov, A. A. Anosov, V. P. Norik, and E. Y. Smirnova. Soft perforation of planar bilayer lipid membranes of dipalmitoylphosphatidylcholine at the temperature of the phase transition from the liquid crystalline to the get state. *Eur. Biophys. J.*, 34:155–162, 2005.

[55] A. Blicher, K. Wodzinska, M. Fidorra, M. Winterhalter, and T. Heimburg. The temperature dependence of lipid membrane permeability, its quantized nature, and the influence of anesthetics. *Biophys. J.*, 96:4581–4591, 2009.

[56] D. C. Devor and R. A. Frizzell. Modulation of k^+ channels by arachidonic acid in t84 cells. ii. activation of a ca^{2+}-independent k^+ channel. *Am J Physiol Cell Physiol*, 274(1):C149–C160, January 1998.

[57] T. Heimburg and A. D. Jackson. On soliton propagation in biomembranes and nerves. *PNAS*, 102(28):9790–9795, 2005.

[58] Tea Mužić. The effect of anesthetics on phase transitions in biological membranes. Master thesis, University of Copenhagen, May 2016.

[59] Søren Blok Madsen. Thermodynamics of nerves. Master thesis, University of Copenhagen, November 2011.

[60] J. R. Hazel. Influence of thermal acclimation on membrane lipid composition of rainbow trout liver. *Am. J. Physiol.*, 236(1):R91–101, 1979.

[61] S. V. Avery, D. Lloyd, and J. L. Harwood. Temperature-dependent changes in plasma-membrane lipid order and the phagocytotic activity of the amoeba acanthamoeba castellanii are closely correlated. *Biochem J.*, 312(Pt 3):811–816, 1995.

[62] T. Heimburg. Mechanical aspects of membrane thermodynamics. estimation of the mechanical properties of lipid membranes close to the chain melting transition from calorimetry. *Biochim. Biophys. Acta.*, 1415(1):147–162, 1998.

[63] R. Dimova, B. Pouligny, and C. Dietrich. Pretransitional effects in dimyristoylphosphatidylcholine vesicle membranes: optical dynamometry study. *Biophys. J.*, 79(1):340–356, 2000.

[64] H. Ebel, P. Grabitz, and T. Heimburg. Enthalpy and volume changes in lipid membranes. ithe proportionality of heat and volume changes in the lipid melting transition and its implication for the elastic constants. *J. Phys. Chem. B.*, 105(30):7353–7360, 2001.

[65] H. Meyer. Zur theorie der alkoholnarkose: Erste mittheilung. welche eigenschaft der anästhetica bedingt ihre narkotische wirkung? *Archiv für Experimentelle Pathologie und Pharmakologie*, 42(2-4):109–118, 1899.

[66] Springer Netherlands. *Studies of Narcosis.* Jena, Gustav Fishcer, 1991.

[67] L. L. Firestone, A. S. Janoff, and K. W. Miller. Lipid-dependent differential effects of stereoisomers of anesthetic alcohols. *Biochim. Biophys. Acta*, 898(1):90–96, 1987.

[68] P. D. Evans, E. A. Kravitz, B. R. Talamo, and B. G. Wallace. The association of octopamine with specific neurones along lobster nerve trunks. *J. Physiol.*, 262:51–70, 1976.

[69] A. Gonzalez-Perez, R. Budvytyte, L. D. Mosgaard, S. Nissen, and T. Heimburg. Penetration of action potentials during collision in the median and lateral giant axons of invertebrates. *Phys. Rev. X*, 4:031047, 2014.

[70] K. Jensen, R. Budvytyte, R. A. Thomas, T. Wang, A. M. Fuchs, M. V. Balabas, G. Vasilakis, L. D. Mosgaard, H. C. Stærkind, J. H. Müller, T. Heimburg, S. Olesen, and E. S. Polzik. Non-invasive detection of animal nerve impulses with an atomic magnetometer operating near quantum limited sensitivity. *Sci. Rep.*, 6:29638, 2016.

[71] National research council, guide for the care and use of laboratory animals, the national academies collection: Reports funded by national institutes of health, eighth ed.,2011.

[72] http://emed.ku.dk/dokumenter/animal_ethics_policy.pdf. University of copenhagen animal ethics policy, accessed may 2016.

[73] www.aaalac.org, acessed may 2016.

[74] J. M. Tobias and S. H. Bryant. An isolated giant axon preparation from the lobster nerve cord. *J. Cell. Comp. Phsiol.*, 46(2):163–182, 1955.

[75] I. Tasaki. Collision of two nerve impulses in the nerve fibre. *Biochim. Biophys. Acta.*, 3:494–497, 1949.

[76] R. W. Berg, M. T. Stauning, J. B. Sørensen, and H. Jahnsen. Comment on "penetration of action potentials during collision in the median and lateral giant axons of invertebrates". *Phys. Rev. X*, 2017.

[77] G. E. Johnson. Giant nerve fibers in crustaceans with special reference to cambarus and palaemonetes. *J. Comp. Neurol.*, 36(4):323–373, 1924.

[78] B. C. Abbott, J. V. Howarth, and J. M. Ritchie. The initial heat production associated with the nerve impulse in crustacean and mammalian non-myelinated nerve fibres. *J. Physiol.*, 178:368–383, 1965.

[79] J. V. Howarth, R. D. Keynes, and J. M. Ritchie. The origin of the initial heat associated with a single impulse in mammalian non-myelinated nerve fibres. *J. Physiol.*, 194:745–793, 1968.

[80] J. M. Ritchie. Energetic aspects of nerve conduction: the relationships between heat production, electrical activity and metabolism. *Prog. Biophys. Mol. Biol.*, 26:147–187, 1973.

[81] R. W. Straub J. M. Ritchie. The movement of potassium ions during electrical activity, and the kinetics of the recovery process, in the non-myelinated fibres of the garfish olfactory nerve. *J. Physiol.*, 249(2):327–348, 1975.

[82] R. D. Keynes and J. M. Ritchie. The movements of labelled ions in mammalian non-myelinated nerve fibres. *J. Physiol.*, 179(2):333–367, 1965.

[83] T. S. Briggs and W. C. Rauscher. An oscillating iodine clock. *J. Chem. Educ.*, 50(7):496, 1972.

[84] B. Schaarschmidt and I. Lamprecht. Simultaneous measurements of heat production and optical density in oscillating reactions. *Thermochim Acta*, 105:205–213, 1986.

[85] T. Heimburg. Linear nonequilibrium thermodynamics of periodic processes and chemical oscillations. *arXiv:1608.06093*, 2016.

[86] A. Einstein. Theory of opalescence of homogenous liquids and liquid mixtures near critical conditions. *Ann. Phys.*, 33(16):1275–1298, 1910.

[87] T. Heimburg. *Biophysics of biological non-equilibrium systems, course handout.* 2016.

[88] L. Onsager. Reciprocal relations in irreversible processes. i. *Phys. Rev.*, 37:405–426, 1931.

[89] L. Onsager. Reciprocal relations in irreversible processes. ii. *Phys. Rev.*, 38:2265–2279, 1931.

[90] S. D. Furrow and R. M. Noyes. The oscillatory briggs-rauscher reaction. 1. examination of subsystems. *J. Am. Chem. Soc.*, 104:38–42, 1982.

[91] S. D. Furrow and R. M. Noyes. The oscillatory briggs-rauscher reaction. 2. effects of substitutions and additions. *J. Am. Chem. Soc.*, 104:42–45, 1982.

[92] R. M. Noyes and S. D. Furrow. The oscillatory briggs-rauscher reaction. 3. a skeleton mechanism for oscillations. *J. Am. Chem. Soc.*, 104:45–48, 1982.

[93] F. D'alba. A study of the oscillation briggs-raushcer reaction by electrochemical methodology. *Bioelectroche. Bioenerg.*, 11:435–447, 1983.

[94] F. J. Sigworth and E. Neher. Single na^+ channel currents ovserved in cultured rat muscle cells. *Nature*, 287:447–449, 1980.

[95] P. Seeman. The membrane expansion theory of anesthesia: Direct evidence using ethanol and a high-precision density meter. *Experientia*, 30(7):759–760, 1974.

[96] P. Seeman. The membrane actions of anesthetics and tranquilizers. *Pharmacol. Rev.*, 24(4):583–655, 1972.

[97] Stanley F. Malamed. *Handbook of local anesthesia, 6th edition.* Elsevier Health Sciences, 2012.

[98] J. M. Ritchie. Mechanism of action of local anaesthetic agents and biotoxins. *Br J Anaesth.*, 47:191–198, 1975.

[99] A. Scholz. Mechanisms of (local) anaesthetics on voltage-gated sodium and other ion channels. *Br J Anaesth.*, 89(1):52–61, 2002.

[100] W. J. McBride, Freeman A, R, JR. L. T. Graham, and M. H. Aprison. Content of amino acides in axons from the cns of the lobster. *J. Neurobiol.*, 6(3):321–328, 1975.

[101] R. F. Bowerman and J. L. Larimer. Command fibers in the circumoesophageal connectives of crayfish. *J. Exp. Biol.*, 60:95–117, 1974.

[102] E. B. Wright and J. P. Reuben. A comparative study of some excitability properties of the giant axons of the ventral nerve cord of the lobster, including the recovery of excitability following an impulse. *J. Cell. Physiol.*, 51(1):13–28, 1958.

[103] A. Avdeef, K. J. box, J. E. A. Comer, C. Hibbert, and K. Y. Tam. ph-metric logp10. determination of liposomal membrane-water partition coefficients of ionizable drugs. *Pharm. Res.*, 15:209–215, 1998.

[104] H. Matsuki, M. Yamanaka, H. kamaya, S. Kaneshina, and I. Ueda. Dissociation equilibrium between uncharged and charged local anesthetic lidocaine in a surface-adsorbed film. *Colloid Polym. Sci.*, 283:512–520, 2005.

[105] C. Högberg and A. P. Lyubartsev. Effect of local anesthetic lidocaine on electrostatic properties of a lipid bilayer. *Biophys. J.*, 94:525–531, 2008.

[106] N. Kladt, U. Hanslik, and H. Heinzel. Teaching basic neurophysiology using intact earthworms. *J Undergrad Neurosci Educ*, 9(1):A20–A35, 2010.

[107] M. Moldovan, K. H. W. Lange, N. J. Aachmann-Andersen, T. W. Kjær, N. V. Olsen, and C. Krarup. Transient impairment of the axolemma following regional anaesthesia by lidocaine in humans. *J. Physiol.*, 592(13):2735–2750, 2014.

[108] Kaare Græsbøll. Influence of anesthetics on the nerve membrane and the nerve pulse. Master's thesis, University of Copenhagen, 2008.

[109] A. L. Hodgkin. A note on conduction velocity. *J Physiol.*, 125:221–224, 1954.

[110] R. J. Pumphrey and J. Z. Young. The rates of conduction of nerve fibres of various diameters in cephalopods. *J. Exp. Biol.*, 15:453–466, 1938.

[111] C. K. Govind and F. Lang. Growth of lobster giant axons: correlation between conduction velocity and axon diameter. *J. Comp. Neurol.*, 170(4):421–433, 1976.

[112] M. Ikeda and Y. Oka. The relationship between nerve conduction velocity and fiber morphology during peripheral nerve regeneration. *Brain Behav.*, 2(4):382–390, 2012.

[113] J. B. Hursh. Conduction velocity and diameter of nerve fibers. *Am. J. Physiol.*, 127:131–139, 1939.

[114] H. S. Gasser and H. Grundfest. Axon diameters in relation to the spike dimensions and the conduction velocity in mammalian a fibers. *Am. J. Physiol.*, 127:393–414, 1939.

[115] I. A. Boyd and K. U. Kalu. Scaling factor relating conduction velocity and diameter for myelinated afferent nerve fibres in the cat hind limb. *J. Physiol.*, 289:277–297, 1979.

[116] E. R. Arbuthnott, I. A. Boyd, and K. U. Kalu. Ultrastructural dimensions of myelinated peripheral nerve fibres in the cat and their relation to conduction velocity. *J. Physiol.*, 308:125–157, 1980.

[117] T. H. Bullock, M. J. Cohen, and D. Faulstick. Effect of stretch on conduction in single nerve fibers. *Biol. Bull., Woods Hole*, 99:320, 1950.

[118] L. Goldman. The effects of stretch on impulse propagation in the median giant fiber of *Lumbricus*. *J. Cell. Physiol.*, 62(1):105–112, 1963.

[119] L. Goldman. The effect of stretch on the conduction velocity of single nerve fibers in *Aplysia*. *J. Cll. Comp. Physiol.*, 57:185–191, 1961.

[120] B. Mulloney. Structure of the giant fibers of earthworms. *Science*, 168:994–996, 1970.

[121] A. R. Martin. The effect of change in length on conduction velocity in muscle. *J Physiol.*, 125:215–220, 1954.

[122] J. P. Wikswo Jr., J. P. Barach, and J. A. Freeman. Magnetic field of a nerve impulse: First measurements. *Science*, 208(4439):53–55, 1980.

[123] J. P. Barach, J. A. Freeman, and JR. J. P. Wikswo. Experiments on the magnetic field of nerve action potentials. *J. Appl. Phys.*, 51(8):4532–4538, 1980.

[124] B. J. Roth and JR. J. P. Wikswo. The magnetic field of a single axon, a comparison of theory and experiment. *Biophys. J.*, 48:93–109, 1985.

[125] B. J. Roth and JR. J. P. Wikswo. The electrical potential and the magnetic field of an axon in a nerve bundle. *Math Biosci*, 76:37–57, 1985.

[126] R. S. Wijesinghe. Magnetic measurements of peripheral nerve function using a neuromagnetic current probe. *Exp. Biol. Med.*, 235:159–169, 2010.

[127] J. F. Barry, M. J. Turner, J. M. Schloss, D. R. Glenn, Y. Song, M. D. Lukin, H. Park, and R. L. Walsworth. Optical magnetic detection of single-neuron action potentials using quantum defects in diamond. *PNAS*, 113(49):14133–14138, 2016.

[128] H. Shen. *Spin squeezing and entanglement with room temperature atoms for quantum sensing and communication.* PhD thesis, University of Copenhagen, Blegdamsvej 17, 2100 Copenhagen, 2014.

[129] D. Budker and M. Romalis. Optical magnetometry. *Nat Phys*, 3:227–234, 2007.

[130] https://www.medicine.mcgill.ca/physio/vlab/Other_exps/CAP/prep.htm. The McGill Physiology Virtual Lab, April 2017.

Appendices

A Heat Capacity and Compressibility

In the following, the derivation of eq. A.1

$$c_p = \frac{\langle H^2 \rangle - \langle H \rangle^2}{RT^2} \qquad \kappa_T^A = \frac{\langle A^2 \rangle - \langle A \rangle^2}{\langle A \rangle \cdot RT} \tag{A.1}$$

will be demonstrated.

Firstly the ensemble averages of a quantity A is defined as

$$\langle A \rangle \equiv \frac{\sum_i A_i \cdot e^{-H_i/RT}}{Q} \tag{A.2}$$

where i represents all possible states and Q is the partition function given by $Q \equiv \sum_i e^{-H_i/RT}$ with H being enthalpy and R is the gas constant.

$$\begin{aligned} c_p &\equiv \left(\frac{d\langle H \rangle}{dT} \right)_p \\ &= \left(\frac{d}{dT} \left(\frac{\sum_i H_i \cdot e^{-H_i/RT}}{Q} \right) \right)_p \\ &= \frac{Q \cdot \sum_i \frac{d}{dT}(H_i e^{-H_i/RT}) - \sum_j H_j e^{-H_j/RT} \frac{d}{dT} Q}{Q^2} \\ &= \frac{\sum_i \frac{H_i^2}{RT^2} e^{-H_i/RT}}{Q} - \frac{\sum_i H_i e^{-H_i/RT}}{Q} \frac{\sum_j \frac{H_j}{RT^2} e^{-H_j/RT}}{Q} \\ &= \frac{\langle H^2 \rangle - \langle H \rangle^2}{RT^2} \end{aligned} \tag{A.3}$$

Similar derivation can be applied for isothermal area compressibility κ_T^A.

$$\begin{aligned} \kappa_T^A \equiv \kappa_T^A &= \frac{1}{\langle A \rangle} \left(\frac{d\langle A \rangle}{d\Pi} \right)_T ; \quad \langle A \rangle = \frac{\sum_i A_i exp(-H_i/RT)}{\sum_i exp(-H_i/RT)} \\ &= -\frac{1}{\langle A \rangle} \left(\frac{d}{dT} \frac{\sum_i A_i \cdot e^{-H_i/RT}}{Q} \right)_T \\ &= \frac{\langle A^2 \rangle - \langle A \rangle^2}{\langle A \rangle RT} \end{aligned} \tag{A.4}$$

B Dispersion in Soliton Model

We prove below that the dispersion term we added is appropriate for low-amplitude periodic solutions. For low-amplitude sound, the sound velocity c is not much affected by density,

$$\frac{\partial^2}{\partial t^2}\Delta\rho^A = c_0^2\frac{\partial^2}{\partial x^2}\Delta\rho^A - h\frac{\partial^4\Delta\rho^A}{\partial x^4} \tag{B.1}$$

Low-amplitude periodic solutions take the form of $\Delta\rho^A = \rho_0^A sin(\omega t - kx)$, thus we obtain

$$\omega^2 = c_0^2k^2 + hk^4 \tag{B.2}$$

$$v^2 = \frac{\omega^2}{k^2} = c_0^2 + hk^2 \approx c_0^2 + \frac{h\omega^2}{c_0^2} \tag{B.3}$$

Eq. B.3 takes the same form as Eq. 2.32 with $h_0 = h/c_0^2$. The dispersion constant acts as the second order term of the Taylor expansion coefficient of the frequency dependency of sound velocity when $\omega = 0$. v and c_0 are assumed close to each other above, and thus $\omega/v \approx \omega/c_0$. The sound velocity is larger when frequency is larger, which is consistent with experimental results. It means that the dispersion term added to the equation is meaningful.

C Temperature Measurement of BR reaction with Stirring and Thermal Insulation

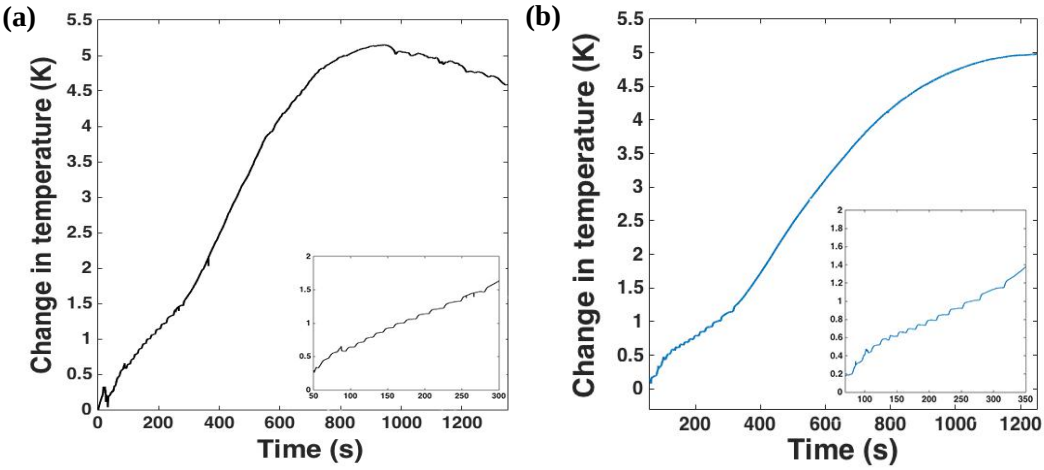

Figure C.1: Temperature measurement during the Briggs-Rauscher reaction. (a) without magnetic stirring. (b) with magnetic stirring.

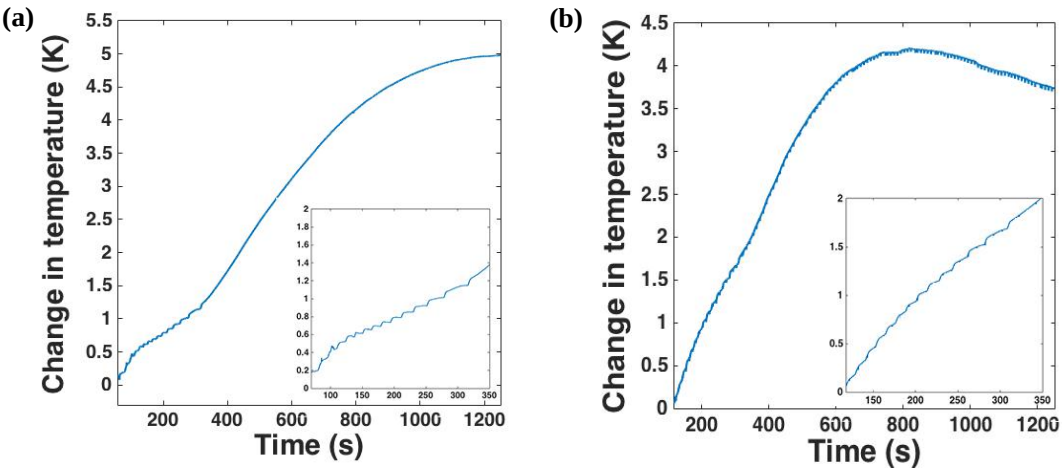

Figure C.2: Temperature measurment during the Briggs-Rauscher reaction. (a) with thermal insulation (b) without thermal insulation. The noise in (b) was from filming of the reaction process by a cellphone.

D Bidirectional Propagation

When stimulation is applied in the middle of an axon, there may generate two nerve impulses propagating in opposite directions. Experiments were conducted to measure the conduction velocity of the two action potentials simultaneously. The stimulation electrodes were placed in the middle of a nerve, and the recording electrodes were placed on the two sides of the nerve with identical distances relative to the stimulation electrodes. The electrode configuration is schematically shown in Fig. D.1.

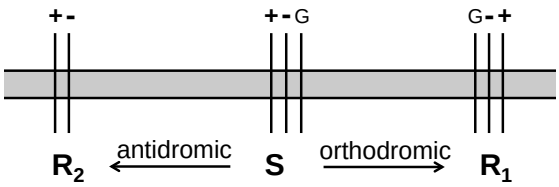

Figure D.1: Schematic illustration of the electrode configuration in the simultaneous measurement of action potentials propagating in opposite directions. S represents the stimulation electrodes, with '+' as the positive electrode, '-' as the negative electrode. Stimulation is given as the voltage between these two electrodes. G represents the ground electrodes for the stimulation and recording. R_1 and R_2 represent the recording electrodes, which is placed at identical distances relative to the stimulation electrodes (ground electrodes don not count). Recording is taken as the voltage difference between two recording electrodes.

Such measurements were done on bundles from lobster legs (bundle of axons) and thoracic ventral cord of lobsters (with ganglia). Results are shown below:

Bundles From Lobster Legs

Three axon bundles can be extracted from lobster legs. We will call them big bundle, medium bundle and small bundle here, according to their relative size. A bundle with a bigger size contain more axons inside. For each nerve sample, the conduction velocity is calculated as the distance between the stimulation electrodes and the recording electrodes divided by the latency between the starting of stimulation and the time corresponding to the peak of the fastest action potential. The calculated conduction velocity is then normalized with the maximum value as 1. Plots are made with the data after the conduction velocity reaches the maximum value.

It can be seen from the average values in Fig. D.2 that both the conduction velocities from orthodromic and antidromic action potential display a slight decrease. However, the error bars are rather large, so that it is somehow difficult to draw definite conclusions from these data. And it may be not appropriate to do an average with different nerves as each individual sample displays unique electrical properties such as the stimulation threshold, and the rate at which the conduction velocity changes.

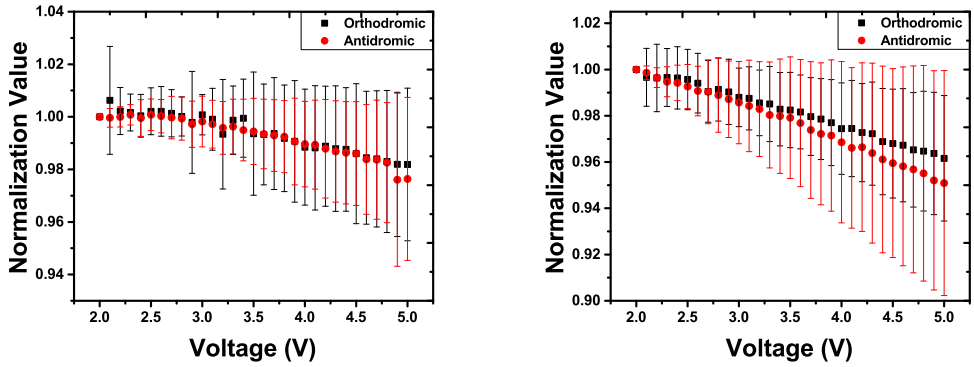

(a) (b)

Figure D.2: The normalized conduction velocity as a function of stimulation voltage. (a) data from the big bundle of lobster legs; (b) data from the medium bundle of loster legs. The signal recorded by the electrodes close to the side of claw is called orthodrmic action potential (orthodromic in the figure), and the signal recorded by the electrodes close to the side of ventral cord is called antidromic action potential (antidromic in the figure).

Thoracic Ventral Cord of Lobster

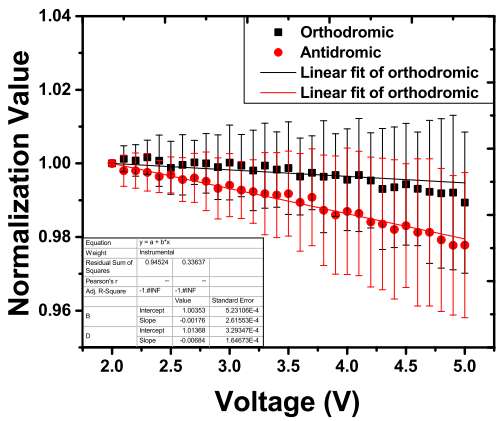

Figure D.3: The normalized conduction velocity as a function of stimulation voltage. The black dots are from orthodromic action potentials, while the red dots are from antidromic action potentials. A linear fit is done for both data for the average values. One finds a bigger slope for the antidromic conduction velocity. There are five segments in the thoracic ventral cord of losters. If we count the first ganglia apart from the brain as zero, then the stimulation electrodes are placed between the second and third ganglia, and the two pairs of recording electrodes are placed between the first and second ganglia, the third and the fourth ganglia, respectively.

Similar results were obtained from thoracic ventral cord of lobsters. Whereas, by focusing on the average values, one can see that the orthodromic conduction

velocity is quite stable with increasing stimulation voltages, while the antidromic conduction velocity decrease with increasing stimulation voltages. This may be related to the presence of ganglia, provided that the data is meaningful for comparison. As the error bars are large, definite conclusions are rather difficult to reach.

Reply to "Comment on 'Penetration of Action Potentials During Collision in the Median and Lateral Giant Axons of Invertebrates'"

Tian Wang, Alfredo Gonzalez-Perez, Rima Budvytyte, Andrew D. Jackson, and Thomas Heimburg*
The Niels Bohr Institute, University of Copenhagen,
Blegdamsvej 17, 2100 Copenhagen, Denmark

(Dated: March 20, 2017)

Berg et al. did not reproduce our results but worked on different preparations and, in one central experiment, used a significantly different electrode configuration. To clarify the situation, we have repeated their experiment on the walking leg of the lobster using apparatus that can produce both electrode configurations. With the configuration used by Berg et al., the signal of the nerve pulse disappears when forced to pass through the region strongly perturbed by the second stimulus. In our original collision setup, pulses do not travel through perturbed regions, and pulses pass through each other without annihilation as previously reported. These results demonstrate that we handle the preparations correctly. Further, they call for a reinterpretation of the so-called collision block experiment performed by Berg et al. Most likely, their results merely indicate inhibition of the nerve pulse by a strong stimulus and not annihilation upon collision as claimed.

In our article from 2014 [1] (referred to as GP2014 henceforth) we showed that pulses in earthworm axons and in the abdominal ventral cord of a lobster can pass through each other. We have since reproduced these results in lobster connectives when individual axons were cut [2]. No ganglia were present in the latter preparation. To our knowledge, the only previous work investigating this effect was that of Tasaki [3] who reported penetration of action potentials in motor nerves from toads. These results are important since predictions using the soliton theory for nerve pulses [4] differ from those of the Hodgkin-Huxley model [5]. The Comment by Berg et al. [6] (referred to as Berg2017 henceforth) questions both our experiments and their interpretation. The statement in our original paper (GP2014) was: "*We can falsify the general belief that annihilation must always occur because of the presence of a refractory period.*" We did not state that action potentials always pass through each other. In their comment Berg2017 used either different preparations or different electrode configurations. Since neither case represents a repetition of our experiments, there is no basis for them to challenge our conclusion. For instance, they used living earth worm rather than isolated axons. Further, they used the walking leg of lobster rather than ventral cords, and they used a different electrode arrangement that leads to a different experimental result. Consequently, our conclusion has not been shown to be incorrect. We show here that pulses may pass through each other even in their setup. Our focus in GP2014 was on the difference between dissipative Hodgkin-Huxley action potentials and non-dissipative solitary waves. We reply only to statements by Berg2017 that are related to our paper.

We shall respond to the points by Berg2017 in the order of appearance in their comment. Additionally, we provide several new experiments that support our original point.

1. Berg2017 report that colliding pulses traveling in opposite directions in their experimental configuration annihilate in intact earthworms. This does not contradict GP2014 which studied extracted nerves and not intact animals. The experiment by Berg2017 may well be correct, but it does not provide sufficient grounds to question the validity of ours.

2. The authors state that the action potential in earthworm is of an all-or-none nature. This assertion may be true but was neither challenged nor even addressed in our article. Further, Berg2017 claim that the pulse amplitudes must be the same in both directions. However, in contrast to their assumption they do not measure amplitudes. Both Berg2017 and GP2014 measure the difference in voltage between two closely spaced electrodes, which effectively corresponds to the spatial derivative of the amplitude. This derivative is zero at the maximum of the voltage pulse. The amplitude itself (i.e., the integral of the signal) is expected to be constant only for the HH model and only for the case of isotropic channel densities. In experiments with isolated nerves the signal also depends on the quality of the contact between nerve and electrodes and is subject to additional variations. This has no effect on the propagation phenomenon itself. The criticism of Berg2017 is not justified.

3. The authors state that velocities must be the same in both directions. This point is not relevant for the message of our 2014 paper. Determination of the velocities there was intended to show that the velocity of individual pulses and of pulses after collision are the same within experimental error, which is true independent of any technical concerns raised by Berg2107. The statement by Berg2017 is also incorrect. In both the HH-model and the soliton theory, pulse velocity depends among other factors on the diameter of the axon which changes over the length of the earthworm or neurons. It is also incorrect that the reported pulse velocity in earthworm axons

* theimbu@nbi.ku.dk; http://membranes.nbi.ku.dk

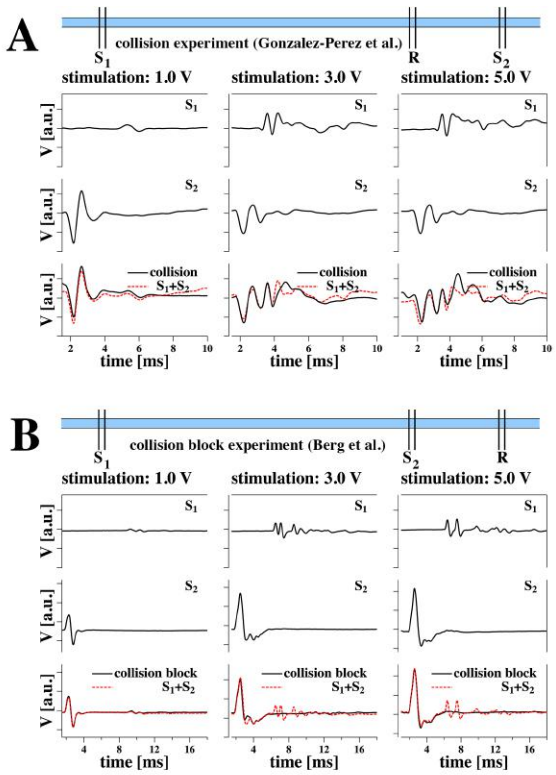

FIG. 1. **A.** The recording electrodes are between stimulation sites S_1 and S_2. Shown are the signals from S_1 only (top row), S_2 only (middle row) and the collision experiment (bottom row) at three different stimulation voltages. At all voltages the sum of the individual signals from S_1 and S_2 and the signal after simultaneous stimulation are very similar or identical. This implies that the pulses have passed through each other. **B.** The experiment by Berg2017 (recording site at the distal end of the nerve after stimulation sites S_1 and S_2) shows a different outcome. While the sum of the individual signals is identical to the post-collision pulse for a stimulation of 1 V, the signal from S_1 is increasingly inhibited for higher voltages.

is "agreed" to be 20 m/s. In fact, it ranges from 3m/s to 30 m/s dependent on the nature and extension of the axon. Our data are in full agreement with the relevant literature on earthworm axons as described in the Supplementary Information [7].

4. Berg2017 argue that compound action potentials in the walking leg of lobster (and in the sciatic nerve of frog) annihilate. Unfortunately, their electrode configuration differs significantly from ours. We show below that this leads to a different outcome of the experiment and most likely to a misinterpretation of their result. Since the authors did not reproduce our experiment, we decided to reproduce theirs and confirm ours at the same time. The electrode configuration of the experiment performed by Berg2017 on the nerve bundles from walking legs is shown in Fig. 1B. Signals arising from the stimulation by electrodes S_1 and S_2 are recorded at one end by the recording electrodes R. Thus, in this configuration only orthodromic pulses are measured. The assumption is that two pulses moving in opposite direction are generated at S_2. In order to arrive at the recording site R, the signal from S_1 must pass both the region of pulse collision and the perturbed region at stimulation site S_2. The collision of pulses and their possible annihilation is not measured directly but inferred from the absence of the signal from S_1 in the recording. Using the nomenclature of Berg2017, we call this experiment the 'collision block experiment'. In contrast, our electrode configuration measures the collision directly. In the following we call this the 'collision experiment'. The recorded pulses do not pass through a stimulated or a perturbed region (Fig. 1A). The simple interchange of R and S_2 is sufficient to switch from one electrode configuration to the other. **Berg2017 did not perform or report this simple control experiment.** Panel A shows the recordings using the configuration from GP2014; Panel B shows the recording on the same nerve following the switching of the electrodes to the configuration of Berg2017. It is apparent that the signal originating from S_1 disappears at high stimulation voltages in the configuration used by Berg2017, while pulses both from S_1 and S_2 remain in the recordings using the configuration of GP2014. At low voltage and without exception, signals from both S_1 and S_2 could be seen at the recording site in Berg's electrode configuration in all experiments on many nerves. Since we can reproduce the results of Berg2017 while simultaneously confirming our own results, we have shown that (i) we treat our nerves correctly and (ii) the collision experiment and the collision block experiment do not measure the same phenomenon. We believe that the strongly perturbed region at stimulation site S_2 of the collision block experiment (Panel B) does not permit propagation of a pulse from S_1 even if orthodromic and antidromic pulses do pass through each other prior to the arrival of the signal from S_1 at S_2. In the Supplementary Information [7] we repeat this experiment using two pairs of recording electrodes so that both experiments are performed simultaneously (Fig. S1). This experiment confirms the findings shown in Fig. 1.

5. As a consequence of **4.**, the final statement by Berg2017 ("annihilation has been reported in dozens, probably hundreds, of publications over the course of more than 65 years.") is possibly not correct. As shown here, the so-called collision-block experiment probably measures something else. This does not mean that these experiments are not correct - it just means that one may have to interpret them differently. The respective literature should therefore be revisited. As shown here, it is possible that the collision-block experiment (described in GP2014 and Berg2017) rather indicates the inhibition of nerves at the site of a very strong stimulus without addressing the question of annihilation.

Conclusion. We have shown for the lobster walking leg that both the collision block experiment of Berg2017 [6] and our collision experiment can be reproduced in the same nerve. Since collision cannot simultaneously lead to

annihilation and to penetration, our results suggest that Berg2017 have measured inhibition of the nerve at the stimulation site and not annihilation. Since we reproduce their result we further demonstrate that we handle the nerve correctly.

The experiments performed by Berg2017 [6] were not identical repeats of our original experiments. Therefore, their results do not invalidate ours.

Acknowledgments. This work was supported by the Villum Foundation (VKR 022130).

[1] A. Gonzalez-Perez, R. Budvytyte, L. D. Mosgaard, S. Nissen, and T. Heimburg, "Penetration of action potentials during collision in the median and lateral giant axons of invertebrates," Phys. Rev. X **4**, 031047 (2014).

[2] A. Gonzalez-Perez, L. D. Mosgaard, R. Budvytyte, E. Villagran Vargas, A. D. Jackson, and T. Heimburg, "Solitary electromechanical pulses in lobster neurons," Biophys. Chem. **216**, 51–59 (2016).

[3] I. Tasaki, "Collision of two nerve impulses in the nerve fiber," Biochim. Biophys. Acta **3**, 494–497 (1949).

[4] T. Heimburg and A. D. Jackson, "On soliton propagation in biomembranes and nerves," Proc. Natl. Acad. Sci. USA **102**, 9790–9795 (2005).

[5] A. L. Hodgkin and A. F. Huxley, "A quantitative description of membrane current and its application to conduction and excitation in nerve," J. Physiol. London **117**, 500–544 (1952).

[6] R. W. Berg, M. T. Stauning, J. B. Sørensen, and H. Jahnsen, "Comment on 'penetration of action potentials during collision in the median and lateral giant axons of invertebrates'," Phys. Rev. X (2017).

[7] T. Wang, A. Gonzalez-Perez, R. Budvytyte, A. D. Jackson, and T. Heimburg, "Reply to "comment on 'penetration of action potentials during collision in the median and lateral giant axons of invertebrates' " - Supplementary Information," Phys. Rev. X (2017).

Reply to "Comment on 'Penetration of Action Potentials During Collision in the Median and Lateral Giant Axons of Invertebrates'"

- Supplementary Information -

Tian Wang, Alfredo Gonzalez-Perez, Rima Budvytyte, Andrew D. Jackson, and Thomas Heimburg*
The Niels Bohr Institute, University of Copenhagen,
Blegdamsvej 17, 2100 Copenhagen, Denmark

(Dated: March 20, 2017)

FURTHER EXPERIMENTS ON THE COLLISION OF NERVE PULSES IN THE WALKING LEG OF THE LOBSTER

We repeated the experiment shown in Fig. 1 with a slightly different electrode configuration. Instead of switching stimulation electrodes S_2 and recording electrodes R as in Fig. (1), we use two pairs of recording electrodes, R_1 and R_2 as shown in Fig. S1A. Stimulation takes place at S_1 and S_2. Recording at R_1 corresponds to the collision experiment performed by GP2014 [1]. Recording at R_2 corresponds to the collision block experiment by Berg2017 [2]. The data for both experiments are obtained simultaneously at both pairs of recording electrodes. Fig. S1B shows the result of the collision experiment. Upon increasing the stimulation voltage, more and more neurons are activated. Nevertheless, after simultaneous stimulation at S_1 and S_2 the sum of the individual signals (S_1+S_2) is practically identical with the recording after simultaneous stimulation for all voltages. No indication of annihilation can be seen. In contrast, the recording at R_2 shows that at higher voltages the signals from S_1 gradually disappear (Fig. S1C). The signals originating from S_1 have a significantly smaller amplitude than those recorded at R_1. This is a consequence of the larger distance of R_2 from the stimulation site and the different velocities of the pulses in the different neurons. However, none of our experiments show any indication of annihilation at low stimulation voltages in the collision block experiment (as already stated in our reply [3]). This could indicate that we never succeed in stimulating the same neurons at S_1 and S_2 or that the disappearance of signals from S_1 at higher voltages is not due to annihilation. Since, simultaneously, no annihilation was observed at recording electrode R_1, it seems more likely that stimulation with high voltage at site S_2 perturbs the membranes to a degree that renders pulse propagation impossible. In the experiment in Fig. S1B no pulse is required to travel through a highly perturbed region. It is clear from Figs. 1 and S1 that measurements on the same pair of pulses can yield dramatically different results depending on the placement of the recording electrodes. This emphasizes the need for caution in tacitly assuming that differences in experiment design are irrelevant.

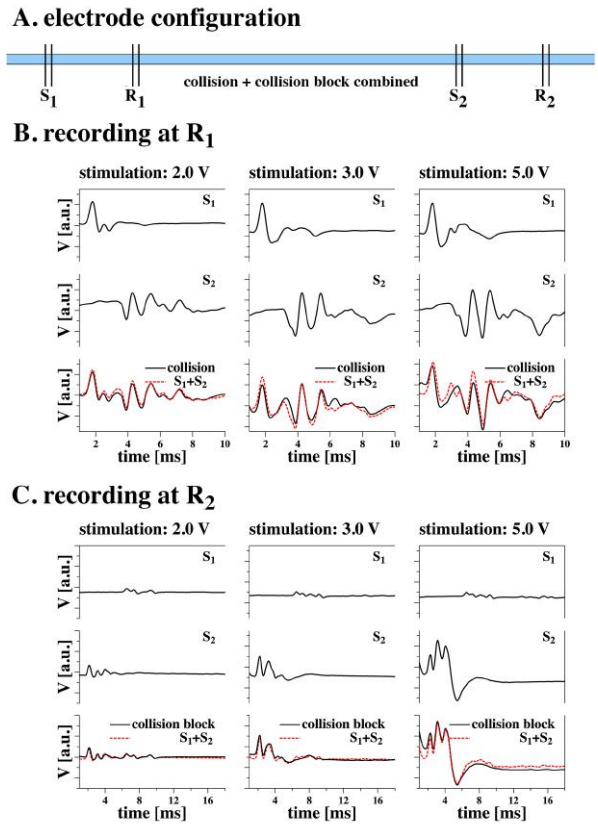

FIG. S1. **A.** Electrode configuration for simultaneous recording of the collision (as in GP2014) and the collision block experiment (as in Berg2017). B: Collision experiment showing penetration of pulses arising from S_1 and S_2 at all voltages. C. Collision block experiment as in Berg2017 showing penetration at low voltage and the absence of some pulses originating from S_1 at high voltage.

We also performed collision experiments with nerves from the ventral cord of lobster tails in a glass capillary where the nerves are always embedded in an electrolyte environment (data will be shown elsewhere). These measurements confirmed our results on the other nerves.

* theimbu@nbi.ku.dk; http://membranes.nbi.ku.dk

This is additional evidence that the criticism made by Berg2017 in their supplement that our results are a consequence of non-physiological conditions is incorrect. For completeness, it should be noted that at high stimulation voltage one can sometimes see single peaks either appearing or disappearing in some collision experiment traces. This might be due to being close to the threshold of single neurons. This does not affect the finding that collision and collision block experiments lead to largely different results. Finally, it is strange that in our experiments we can always stimulate all neurons separately by increasing voltage, both in worm and lobster nerves. This is not seen in the experiments shown by Berg2017.

PULSE VELOCITIES

Berg2017 [2] dedicates considerable space to a discussion of pulse amplitudes and absolute pulse velocities in earthworm axons. These issues are of no relevance for our 2014 article [1]. Nevertheless, we feel that it is useful to comment some of the statements made in Berg2017, which are not generally valid.

1. The authors state that velocities in both directions must be the same. This is incorrect [4]. Both in the HH-model and the soliton theory the velocity depends on the diameter of the axon which changes over the length of the earthworm. Pulses coming from different ends of a neuron travel through regions of different average diameter if the recording electrode is placed between the stimulation sites.
2. The assignment of a velocity to a nerve pulse is ambiguous because it is determined by arbitrarily choosing a reference point in the signal and relating it to the distance between the electrodes. It is difficult to compare the velocities if the shapes of the pulses are not identical.
3. Berg2017 claim that "The results show that the velocity is the same in both directions (within the accuracy of the measurement), and markedly higher (approx. 20m/s) than reported by Gonzalez-Perez et al. (2-8 m/s). A velocity of 20 m/s is in agreement with the literature". It is incorrect that the value of Berg2017 is the general finding in the literature. The velocity of the median giant axon of the earthworm ventral cord can actually vary from 6 to 30 m/s and the velocity of the lateral giant axon of the earthworm from 2 to 10 m/s. In the experiments by GP2014 the velocity of median giant axon was 6-10 m/s in 30 different preparations, and 3-7 m/s in the lateral giant axon. These numbers are consistent with [5].
4. There is no theoretical need for action potentials to maintain their shape, neither in the Hodgkin-Huxley model (where it depends on radius and channel distribution) nor in the Soliton model (where it also depends on the radius due to changing energy densities). The claim that pulses traveling in opposite directions must have the same shape, velocity and amplitude is therefore unjustified. In fact, there are numerous reports showing that orthodromic pulses propagate faster than antidromic pulses, e.g. [4, 6, 7].
5. In addition, both the experimental temperature and the acclimation temperature of the animal influence the velocity in the axons. Lagerspetz et al. [5] found velocities ranging between 6 and 32 m/s in the median giant axon of worms and 3-10 m/s in the lateral giant axon. Kladt et al. (2010) report velocities of 6-14 m/s in the median giant axon and 4-7 m/s depending on temperature (between 2°C and 25°C) in the intact earthworm [8]. In any event, precise determination of the conduction velocity of the median and lateral giant fibers of the intact earthworm (as used by Berg2017) is not possible. The reason is anatomical. These axons are not perfectly straight but are rather bent along the principal axis. Thus, earthworms can stretch two or three times their length without damaging their ventral cords [9]. Any attempt to determine the conduction velocity in the intact earthworm will result only in an apparent velocity. It is shown in [9] that the apparent conduction velocity of earthworm nerves can change from 8 to 20 m/s upon stretching. This is especially relevant when the intact earthworm moves.

Thus, contrary to the claims of the authors of Berg2017, there is clear evidence in the literature that orthodromic and antidromic pulses can have different shapes and velocities. The findings in GP2014 are completely consistent with results reported in the literature.

[1] A. Gonzalez-Perez, R. Budvytyte, L. D. Mosgaard, S. Nissen, and T. Heimburg, "Penetration of action potentials during collision in the median and lateral giant axons of invertebrates," Phys. Rev. X **4**, 031047 (2014).

[2] R. W. Berg, M. T. Stauning, J. B. Sørensen, and H. Jahnsen, "Comment on 'penetration of action potentials during collision in the median and lateral giant axons of invertebrates'," Phys. Rev. X (2017).

[3] T. Wang, A. Gonzalez-Perez, R. Budvytyte, A. D. Jackson, and T. Heimburg, "Reply to "comment on 'penetration of action potentials during collision in the median and lateral giant axons of invertebrates' "," Phys. Rev. X (2017).

[4] J. S. Coombs, D. R. Curtis, and J. C. Eccles, "The interpretation of spike potentials of motoneurones." J. Physiol. London **139**, 1469–7793 (1957).

[5] K. Y. H. Lagerspetz and A. Talo, "Temperature acclimation of the functional parameters of the giant nerve fibres

in *Lumbricus terrestris* L. I. conduction velocity and the duration of the rising and falling phase of action potential." J. Exp. Biol. **47**, 471–480 (1967).

[6] J. C. Eccles, *The physiology of nerve cells.* (Johns Hopkins Press, Baltimore, 1957).

[7] M. G. F. Fuortes, K. Frank, and M. C. Becker, "Steps in the production of motoneuron spikes," J. Gen. Physiol. **40**, 735–752 (1957).

[8] N. Kladt, U. Hanslik, and H.-G. Heinzel, "Teaching basic neurophysiology using intact earthworms." J. Undergrad. Neurosci. Educ. **9**, A20–35 (2010).

[9] L. Goldman, "The effects of stretch on cable and spike parameters of single nerve fibres; some implications for the theory of impulse." J. Physiol. London **175**, 425–444 (1964).

SCIENTIFIC REPORTS

OPEN

Non-invasive detection of animal nerve impulses with an atomic magnetometer operating near quantum limited sensitivity

Received: 06 April 2016
Accepted: 22 June 2016
Published: 15 July 2016

Kasper Jensen[1], Rima Budvytyte[1], Rodrigo A. Thomas[1], Tian Wang[1], Annette M. Fuchs[2], Mikhail V. Balabas[1,3], Georgios Vasilakis[1], Lars D. Mosgaard[1], Hans C. Stærkind[1], Jörg H. Müller[1], Thomas Heimburg[1], Søren-Peter Olesen[2] & Eugene S. Polzik[1]

Magnetic fields generated by human and animal organs, such as the heart, brain and nervous system carry information useful for biological and medical purposes. These magnetic fields are most commonly detected using cryogenically-cooled superconducting magnetometers. Here we present the first detection of action potentials from an animal nerve using an optical atomic magnetometer. Using an optimal design we are able to achieve the sensitivity dominated by the quantum shot noise of light and quantum projection noise of atomic spins. Such sensitivity allows us to measure the nerve impulse with a miniature room-temperature sensor which is a critical advantage for biomedical applications. Positioning the sensor at a distance of a few millimeters from the nerve, corresponding to the distance between the skin and nerves in biological studies, we detect the magnetic field generated by an action potential of a frog sciatic nerve. From the magnetic field measurements we determine the activity of the nerve and the temporal shape of the nerve impulse. This work opens new ways towards implementing optical magnetometers as practical devices for medical diagnostics.

The magnetic field generated around a signaling nerve fiber is of key interest both from a basic scientific and a clinical point of view. The transmembrane potentials have been extensively measured with electrophysiological techniques. Magnetic field measurements are insensitive to the transmembrane currents as the fields from the opposite currents in and out of the membrane cancel. Instead, magnetic field measurements allow for a true measurement of the axon's axial net current, which is the depolarizing wavefront driving the action potential. Magnetic field recordings also allow for non-invasive measurements of the conduction velocity of peripheral nerves[1] which is necessary for diagnostics of multiple sclerosis, myotonia and intoxication in patients.

The magnetic field of a nerve impulse was first measured by Wikswo *et al.*[2] using a combination of a superconducting SQUID magnetometer and a toroidal pick-up coil through which the nerve had to be pulled. This method is not compatible with *in vivo* diagnostics and yields the magnetic field values which are much higher than that in an animal because the return currents in the surrounding tissue are not measured. Here we are able to detect the nerve impulse with the sensor placed beside the nerve, several millimeters away, the setting compatible with *in vivo* studies. Detection of nerve impulses with a magnetometer based on Nitrogen-Vacancy centers in diamond has recently been reported[3]. Such magnetometers seem promising for magnetic field microscopy applications where the magnetometer can be placed at micrometer distance or closer to the biological object.

Sensitivity of atomic magnetometers[4] improves with the number of atoms sensing the field, which for vapor magnetometers is defined by volume and temperature. For example, femtoTesla sensitivity has been achieved with magnetometers operating at a temperature of several hundred of °C in the so-called SERF regime[5] used also for medical applications[6–8]. Similarly high sensitivity has been achieved at room temperature using much fewer atoms by means of quantum state engineering[9] leading to operation beyond standard quantum limits of

[1]Niels Bohr Institute, University of Copenhagen, Blegdamsvej 17, 2100 Copenhagen, Denmark. [2]Department of Biomedical Sciences, Faculty of Health and Medical Sciences, University of Copenhagen, Blegdamsvej 3, 2200 Copenhagen N, Denmark. [3]Department of Physics, St Petersburg State University, Universitetskii pr. 28, 198504 Staryi Peterhof, Russia. Correspondence and requests for materials should be addressed to E.S.P. (email: polzik@nbi.dk)

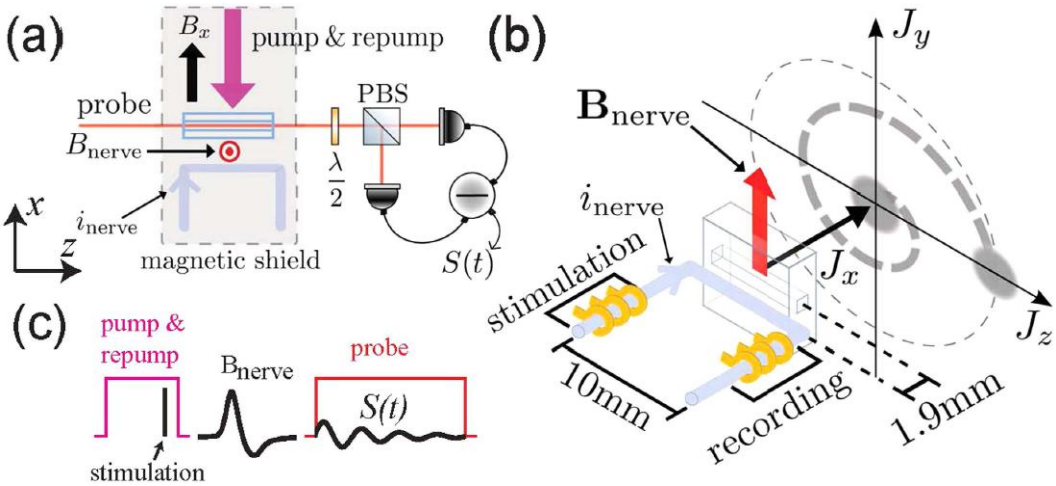

Figure 1. (**a**) Schematic of the experimental setup. Probe light propagates along the z axis. Half-wave plate $\lambda/2$, polarizing beam splitter (PBS) and differential photodetection are components of polarization detector. (**b**) The magnetometer principle. The amplitude of the collective atomic spin precession in z, y plane is proportional to B_{nerve}. Spin projection J_z is measured by probe light with the sensitivity limited by the quantum projection spin noise (fuzzy circle). The magnetic field from the nerve is circumferal. The average field detected by the magnetometer points in the y-direction. (**c**) The measurement sequence for the pulsed magnetometer mode.

sensitivity. Room temperature operation allows to place the sensor in contact with the skin or potentially inside the human body. The close proximity of the sensor to the source of magnetic field is a big advantage as the magnetic field rapidly decreases with the distance from the source. Room-temperature cesium magnetometer has been used for medical applications[10], however, it operated far above quantum limits of sensitivity.

Results

Here we use the approach of ref. 9 for nerve impulse measurements. The sensitive element of the magnetometer is cesium atomic vapour. Cesium has a high vapor pressure such that high sensitivity can be reached at room- or human body temperature. The magnetic moment (spin) of atoms $\mathbf{J} = (J_x, J_y, J_z)$ is prepared by optical pumping in the x-direction, along the direction of a bias field B_x [see Fig. 1(a)]. The magnetic field of the nerve B_{nerve} will create a transverse spin component $\mathbf{J}_\perp = (J_y, J_z)$ which afterwards will rotate in the y-z plane at the Larmor frequency $\Omega = B_x/\gamma$ [see Fig. 1(b)], where $\gamma = 2.20 \cdot 10^{10}$ rad/(s·T) is the cesium gyromagnetic ratio. The J_z spin component is detected optically by measuring the polarization rotation of the probe light. The magnetic field from the nerve is detected in two modalities, a continuous mode where the magnetic field as a function of time $B(t)$ is detected, and a pulsed mode where the Fourier component $|B(\Omega)|$ is detected. In the continuous mode the pump and probe light is continuously on. In the pulsed mode [see Fig. 1(c)], a pulse of pump light is followed by the pulse of magnetic field, and finally the spins are detected with a pulse of probe light.

Optical magnetometers are fundamentally limited by quantum noise consisting of the spin-projection noise (PN) shown as the fuzzy circle in Fig. 1(b), quantum shot noise of the probe light and quantum back action of the probe on the spin[9]. For an optimal measurement these noise sources add up to the standard quantum limit (SQL)[11]. This limit has been reached for magnetic fields oscillating at hundreds of kHz[9]. Here we approach the SQL for the magnetic field measurement of nerve impulses whose frequency is much lower using the techniques described in the Supplementary Information. For continuous measurements, the SQL magnetic field uncertainty ΔB_{SQL} normalized by the total measurement time T_{tot} yields the sensitivity $\Delta B_{\text{SQL}}\sqrt{T_{\text{tot}}} \approx 1.5/(\gamma\sqrt{T_2 J_x/2})$ in units of $\text{T}/\sqrt{\text{Hz}}$. T_2 is the spin coherence time and $J_x = 4N_A$ is the total atomic spin for N_A cesium atoms. At room temperature of 22 °C, the cesium atomic density is $3.1 \times 10^{16}\,\text{m}^{-3}$ which is the highest of all elements appropriate for atomic magnetometry. The pulsed measurement has the SQL magnetic field uncertainty of $\Delta|B_{\text{SQL}}(\Omega)| \approx 1.5/(\gamma\sqrt{2J_x})$ if the magnetic pulse duration $\tau \ll T_2$ (see Supplementary Information).

A long spin-coherence time T_2 is crucial for a high sensitivity. In this work we utilize a vapor cell with the inside surface coated with alkane[12,13]. The coating protects atomic spin states from decoherence over many thousands of wall collisions and provides $T_2^{\text{dark}} = 27$ ms which is longer than a typical nerve impulse duration $\tau \approx 2$ ms, as required for the ultimate sensitivity. The cesium vapor is contained in a 1.0 mm × 1.0 mm × 7.7 mm channel inside a rectangular glass chip of dimensions 2.3 mm × 8.4 mm × 7.7 mm. This small rectangular vapor cell allows us to have atoms at an average distance of a few mm from the nerve, which is close to a typical distance for many medical applications.

A frog sciatic nerve contains a few nerve bundles each with several thousand axons inside (see Methods section). The nerve is placed inside a plastic chamber where it can be kept alive in a saline solution for more than 5 hours. The nerve is electrically stimulated from one end with a pair of gold electrodes [see Fig. 1(b)]. The stimulus triggers an action potential (a nerve impulse) propagating along the nerve. As a reference measurement we perform an electrical recording of the impulse with another pair of electrodes. Figure 2(a) shows the electrically recorded signals for different stimulation voltages. Figure 2(b) shows the frequency spectra of the nerve signals

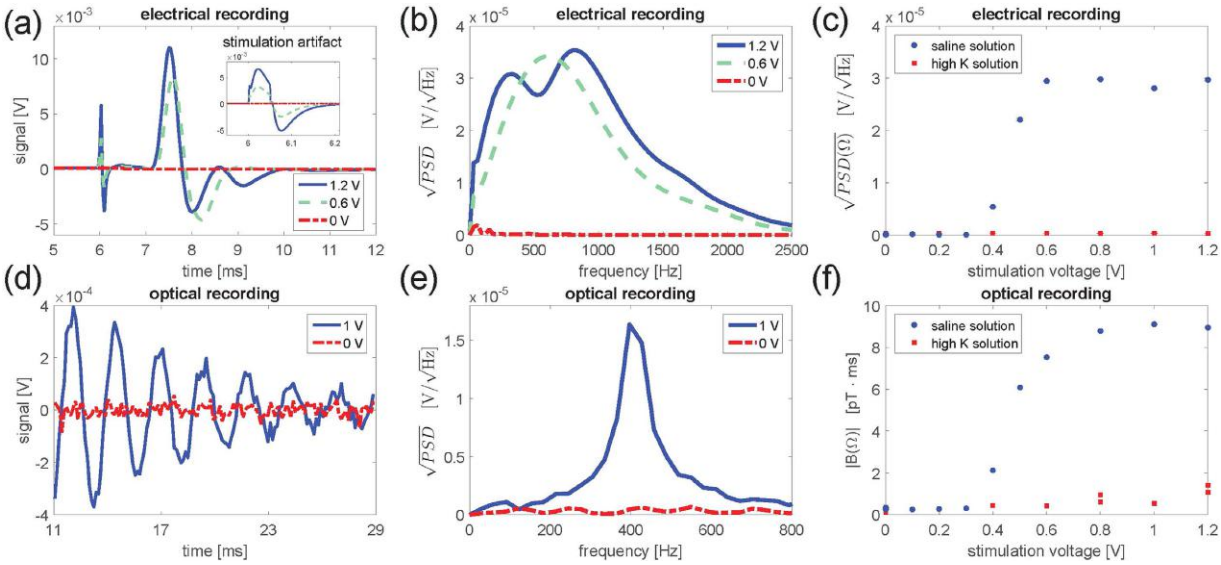

Figure 2. Electrical and optical measurements of the nerve impulse for different stimulation voltages. The optical measurements were done in the pulsed mode using 1000 averages. The figures show the signals in time, the square-root of the power spectral density *PSD* and the 400 Hz frequency component. The plotted electrical signals are after 10 times amplification. The uncertainties on the data points in (**c**) are to small to be visible in the figure. The uncertainties on the points in (**f**) can be estimated from the points without stimulation (0 V) which were measured 9 times and resulted in a 0.25(10) pT·ms signal. By dividing the nerve signal (9.1 pT·ms) by the noise floor obtained without stimulation (0.25 pT·ms) we find the signal to noise ratio, $SNR \approx 37$.

and Fig. 2(c) shows the amplitude of the 400 Hz Fourier component. The nerve is stimulated at $t = 6.0$ ms. The signature of the nerve signal is its non-linear behavior with stimulation voltage, with a firing threshold at around 0.4 V. For voltages above the threshold a nerve impulse is measured with the recording electrodes within the time interval $t = 7.0 - 10.0$ ms. We also observe a stimulation artifact at $t = 6.0$ ms [see inset in Fig. 2(a)] which is proportional to the stimulation voltage.

In parallel to the reference electrical recording the nerve signal is detected optically using the pulsed magnetometer mode. The magnetometer is positioned near the middle part of the nerve separated only by a thin microscope cover slip. As the nerve is bent in a U-shape, we mainly detect the field from the 10 mm section of the nerve closest to the magnetometer [see Fig. 1(b)]. The axial ionic current in this 10 mm section can be considered constant, as the action potential has a duration ≈3 ms, the velocity ≈30 m/s, and therefore an extent ≈9 cm ≫ 10 mm. The circumferal magnetic field $\mathbf{B}_{\mathrm{nerve}}$ from the nerve is on average transverse to the initial spin direction J_x and will therefore create a transverse spin component [see Fig. 1(b)]. Figure 2(d) shows the magnetometer signal, Fig. 2(e) shows the spectrum and Fig. 2(f) shows the magnetic field Fourier component at the Larmor frequency of 400 Hz. A clear threshold for the nerve firing is observed confirming that the magnetometer is capable of detecting the nerve impulse. From calibration measurements (see Methods section) we determine the Fourier component of the magnetic field from the nerve as $|B_{\mathrm{nerve}}(\Omega)| = 9.1$ pT·ms. From Fig. 2(f) we infer that the nerve impulse can be detected optically with a signal to noise ratio $SNR \approx 37$ using 1000 averages. As the *SNR* scales as $1/\sqrt{N_{\mathrm{avg}}}$ we find the $SNR \approx 1.2$ for a single shot, i.e., it should be possible to detect a nerve impulse in a single shot.

As a control experiment, we make the nerve inexcitable[14] by replacing the saline solution in the plastic chamber with a solution with high potassium concentration. As expected, we clearly observe from both electrical [Fig. 2(c)] and optical [Fig. 2(f)] measurements that the nerve signal is blocked by this solution. Note that the stimulation artifact which was observed in the electrical recording (inset to Fig. 2(a)) should be small in the optical measurements, as the stimulation occurs during the optical pumping [see Fig. 1(c)] where the response to magnetic fields is strongly damped. When the nerve is inexitable, we do see such a small stimulation artifact (squares in Fig. 2(f)) for the higher stimulation voltages.

The high spatial resolution of our magnetometer (the channel containing the cesium atoms is 1.0 mm across) and the good signal to noise ratio allows us to characterize how the magnetic field decays with distance from the nerve. The results are shown in Fig. 3 and one sees that we can detect the nerve impulse more than 5 mm away. The actual distance dependence may be complicated as the frog sciatic nerve contains 1000's of axons organized in several bundles (see Supplementary Fig. 1). However, we expect a power law dependence $B(x) \propto 1/(x + x_0)^n$ with n between 1–3. $n = 1$ corresponds to the magnetic field from an infinitely long wire and $n = 3$ corresponds to the field from a magnetic dipole. x_0 is the position of the nerve relative to our estimate of 1.9(5) mm based on the size of the vapor cell and dimensions of the nerve. Fitting the data to a power law dependence yields $x_0 = 0.2(8)$ mm and $n = 1.5(4)$ which are within the expected ranges.

The magnetometer can also be operated in the continuous mode which allows for determination of the temporal shape of the magnetic field generated by the nerve, $B_{\mathrm{nerve}}(t)$. The magnetometer response was optimized by matching its frequency response (a Lorentzian centered at the Larmor frequency with a full width at half

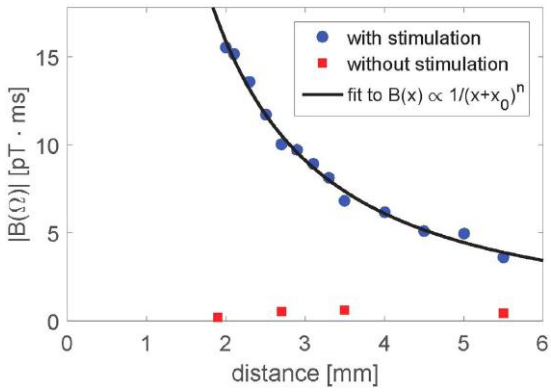

Figure 3. Magnetic field fourier component as a function of distance (using 1000 averages per point). The closest distance from the center of the magnetometer to the center of the nerve was estimated to be 1.9 mm. Circles: Nerve magnetic field, squares: magnetometer noise floor, line: fit to a power-law dependence, fit parameters $n = 1.5(4)$, $x_0 = 0.2(8)$ mm. The uncertainties on the fit parameters are the 68% confidence bounds.

maximum $1/(\pi T_2)$) with the spectrum of the nerve impulse (see Fig. 2(b)). The bandwidth $1/(\pi T_2) = 860$ Hz was set by choosing suitable power levels for the pump, repump and probe lasers. Figure 4(a,b) show the electrical and optical signals respectively as a function of time for different stimulation voltages. In both electrical and optical measurements we observe two features (A and B). Feature A is due to the stimulation as it starts at the time of stimulation and increases linearly with the stimulation voltage. Feature B is due to the nerve signal, as it last for several ms and only appears above the threshold for the nerve firing (here 0.8 V or greater). Figure 4(c) shows a comparision of the electrical signal for 0.8 V stimulation and the detected magnetic field $B(t)$ as calculated by deconvolving the optical signal with the magnetometer response [see Methods]. The temporal profiles of the electrical signal and the magnetic field look very similar; both show the action potential and a stimulation artifact. From the bottom plate of Fig 4(c) we conclude that the nerve magnetic field has a 24 pT peak-to-peak amplitude (measured at an average distance of 1.9 mm) and that the nerve conduction velocity is 34(8) m/s (see Supplementary Information). The effective axial ionic current is estimated to be 0.23 μA (see Supplementary Information) which is consistent with earlier measurements[15].

From the data we find the single shot experimental uncertainty $\Delta|B_{\mathrm{exp}}(\Omega)| = 7.7$ pT·ms for the pulsed mode and a sensitivity of 230 fT/$\sqrt{\mathrm{Hz}}$ in the continuous mode (see Methods section). The standard quantum limit for the magnetic field uncertainty is in the pulsed mode $\Delta|\boldsymbol{B}_{\mathrm{SQL}}(\Omega)| = 1.6$ pT·ms. In this mode the light is off during the nerve impulse duration $\tau \approx 2$ ms which satisfies $\tau \ll T_2^{\mathrm{dark}}$. In the continuous mode, where the $T_2 = 0.37$ ms matches the nerve impulse bandwidth, the SQL for the sensitivity is 160 fT/$\sqrt{\mathrm{Hz}}$. As the experimental sensitivity is close to the SQL, quantum noise (projection noise, shot noise, back-action noise) is a considerable fraction of the total noise. Some uncompensated low frequency classical noise of the probe light and of the atomic spin also contributed to the total noise, in particular for the pulsed measurements.

Discussion

Projection noise dominated sensitivity can be reached by relatively straightforward steps, such as using multipass vapor cells[16], by modest heating (increasing the temperature from room-temperature 22 °C to the human body temperature 37 °C will increase the sensitivity by a factor of two[17]) or by employing a low finesse optical cavity[11]. Gradiometry with two cells with oppositely oriented spins allows for generation of nonclassical entangled states leading to sensitivity beyond the PN limit[9] as well as provides additional compensation of the ambient magnetic fields and classical fluctuations of the atomic spins.

In conclusion, we have performed non-invasive detection of nerve impulses from the frog sciatic nerve by measuring the magnetic field generated by the nerve with a room-temperature sensor with near quantum limited sensitivity. A mm-sized sensor which is sensitive enough to detect sub-picoTesla fields at a distance of a few millimeters from biological objects makes the magnetometer perfect for medical diagnostics. We envision that practical, low-cost, and room-temperature atomic magnetometers could be an alternative to the current technology based on cryogenically-cooled SQUID magnetometers which are widely used for magnetoencephalography (MEG) and neuroscience studies[18,19]. Promising applications of atomic magnetometers include MEG[20], detection of epilepsy[8], detection of the synaptic responses in the retina, and cardiography of fetuses[6].

Methods

Nerve preparation. This study was conducted in accordance with the University of Copenhagen Animal Ethics Policy[21] and the frogs used were handled by the animal facility at the Department of Experimental Medicine at the University of Copenhagen which is accredited by the Association for Assessment and Accreditation of Laboratory Animal Care International (AAALAC)[22]. The experiments presented here with the frog sciatic nerve do not require a license.

Sciatic nerves were isolated from green frogs (Rana Esculenta). The frogs were decapitated and the sciatic nerves were isolated from spine and down to the knee. The nerves are 7–8 cm long with a diameter of 1.3 mm

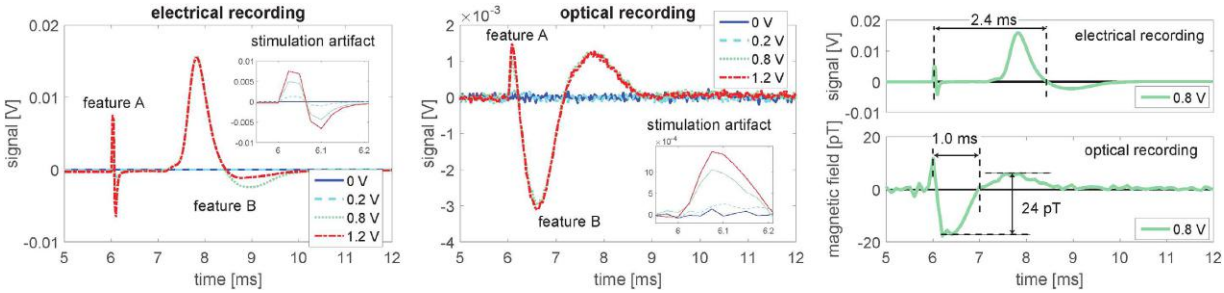

Figure 4. Electrical and optical measurements of the nerve impulse for different stimulation voltages. The magnetometer was operated in the continuous mode and the signals were averaged 5000 times. (**a**) Electrical and (**b**) optical measurements. (**c**) Electrical signal for 0.8 V stimulation and magnetic field calculated by deconvolution. For these specific measurements the Larmor frequency was 510 Hz and the coherence time 0.37 ms.

in the proximal end and slightly thinner in the distal end. In the proximal end there is one bundle that divides twice so distally it is composed of three bundles. Supplementary Fig. 1 shows an electron micrograph of the nerve where it is seen that the nerve bundles contain a few thousand of axons.

Throughout the dissection and the course of the experiments, the frog sciatic nerves were kept moist in cold Ringers solution (also called saline solution) of 115 mM NaCl, 2.5 mM KCl, 1.8 mM $CaCl_2$, 1.08 mM $Na_2HPO_4 \cdot 2H_2O$, 0.43 mM $NaH_2PO_4 \cdot H_2O$, adjusted to pH 7.1[23]. Ringers solution approximates the ionic composition of the extracellular fluids of the frog. A high potassium concentration Ringers solution, in which all NaCl was replaced by KCl with final K^+ concentration being 117mM and Na^+ 0 mM and Cl^- concentration remaining constant, was used to make nerves inexcitable[14].

Nerve chamber and electrical recording. The nerves are kept in a 3D-printed plastic chamber during the experiments. The chamber is a 47 × 18 mm block of 8.5 mm height that contains a longitudinal U-shaped channel with a diameter of 2 mm in which the nerve is placed. The channel allows maintenance of a saturated water-vapor atmosphere in order to keep the nerve moist. The front part of the chamber is placed close to magnetometer and it is covered by a microscope glass cover slip of 0.13 mm thickness.

The chamber has 6 circular gold electrodes on each side. The electrodes have an outer diameter of 6 mm with the hole inside of 1.5 mm, which fits into the channel. On each side, the distance between electrodes is 5 mm.

The nerve was externally stimulated in the proximal end by applying a short 50 μs square voltage pulse between two spatially separated electrodes surrounding the nerve. The nerve signal was measured in the distal end as a potential difference between a pair of two electrodes. The electrical signal was amplified 10 times and filtered (using a 3 kHz low pass and a 10 Hz high pass filter) and recorded simultaneously with the magnetic field recordings.

Operation of the magnetometer. The magnetometer is based on optical read-out of spin-polarized atomic vapour. The cesium atoms are prepared by an optical pumping with a pulse of circular polarized light such that the total spin vector $\mathbf{J} = (J_x, J_y, J_z)$ points in the x-direction, which is also the direction of a bias field B_x [see Fig. 1(a)]. Any magnetic field perpendicular to x-direction (such as the magnetic field from the nerve) will create a transverse spin component $\mathbf{J}_\perp$ which afterwards will precess around the bias magnetic field at the Larmor frequency $\Omega = B_x/\gamma$ [see Fig. 1(b)], where $\gamma = 2.20 \cdot 10^{10}$ rad/(s·T) is the cesium gyromagnetic ratio. The transverse spin component is detected optically by measuring the polarization rotation of linearly polarized probe light passing through the vapor cell using a balanced polarimeter. The magnetic field from a nerve can be detected in two modalities, a pulsed or a continuous one. In the continuous mode the pump and probe light is continuously on. In this case, the magnetometer signal $S(t)$ is proportional to the convolution of the magnetic field with the magnetometer response function $S(t) \propto \int_{t'=0}^{t} \{e^{-\Gamma(t-t')} \cos[\Omega(t-t')]\} B_y(t')dt'$, where we assumed the transverse field is along the y-direction. The relaxation rate $\Gamma = 1/T_2$, which is the inverse of the spin-coherence time T_2, increases linearly with laser power and is in the limit of low power denoted $\Gamma_{\mathrm{dark}} = 1/T_2^{\mathrm{dark}}$. In the pulsed mode [see Fig. 1(c)], a pulse of pump light first initializes the atomic spins along the x-direction, then the pulse of magnetic field creates a transverse spin component, and finally the spins are detected with a pulse of probe light. In this case, the magnetometer signal is a free induction decay $S(t) = A \sin(\Omega t + \theta) e^{-\Gamma t}$, where θ is a phase and the amplitude A is proportional to the Fourier component of the magnetic field at the Larmor frequency: $|B(\Omega)| = \left|\int_0^\tau B_y(t) e^{-i\Omega t} dt\right|$, where τ is the duration of the magnetic field pulse. For both pulsed and continuous modes, the proportionality constant can be found by applying a known calibration magnetic field.

Calibration of the pulsed magnetometer. The magnetometer is calibrated by applying a known magnetic field. This calibration field is produced by a coil positioned inside the magnetic shield; the field points in the y-direction and has the temporal shape of a single sinusoidal oscillation $B_{\mathrm{cal}}(t) = B_{\mathrm{cal}} \sin(\Omega_{\mathrm{cal}} t)$ with amplitude $B_{\mathrm{cal}} = 2$ nT, frequency $\Omega_{\mathrm{cal}} = 2\pi \cdot 400$Hz and Fourier component $|B_{\mathrm{cal}}(\Omega_{\mathrm{cal}})| = \pi B_{\mathrm{cal}}/\Omega_{\mathrm{cal}} = 2.5$ nT·ms.

In the pulsed mode, the calibration field is applied in between the pump and probe pulses. The recorded magnetometer signal (the free induction decay) is shown in Supplementary Fig. 2(a). The spectrum (calculated as the square-root of the power spectral density $\sqrt{PSD}$) is peaked at the Larmor frequency of the atoms $\Omega = 2\pi \cdot 400\,\mathrm{Hz}$ [Supplementary Fig. 2(b)]. The peak amplitude is proportional to the magnetic field Fourier component: $\sqrt{PSD(\Omega)} \propto |B(\Omega)|$. The proportionality constant can be calculated from the data in Supplementary Fig. 2(b) and the known Fourier component of the calibration field. With this calibration we can calculate the Fourier component $|B_{\mathrm{nerve}}(\Omega)|$ of the nerve magnetic field [see Fig. 2(f)] from the measured peak values $\sqrt{PSD(\Omega)}$ [see Fig. 2(e)].

Supplementary Fig. 2(a,b) also show the magnetometer signal without the applied calibration field. The signal was averaged 1000 times before recorded. The noise at the Larmor frequency is 10200 times smaller than the signal obtained with the calibration field, i.e., the calibration field is detected with a $SNR = 10200$ corresponding to a minimal detectable magnetic field Fourier component $2.5\,\mathrm{nT{\cdot}ms}/10200 = 0.25\,\mathrm{pT{\cdot}ms}$ using 1000 averages. The single shot minimal detectable Fourier component is then 7.7 pT·ms.

Calibration of the continuous magnetometer. In the continuous mode, the lasers are on during the applied calibration field. In this case the magnetometer signal is proportional to the convolution of the magnetic field with the magnetometer response function. Supplementary Fig. 2(c) top shows the detected signal together with a fit to the function $S(t) \propto \int_{t'=0}^{t} \{e^{-\Gamma(t-t')} \cos[\Omega(t-t')]\} B_y(t')\,dt'$ from which we can determine the Larmor frequency and the coherence time. Using the fitted parameters we can perform numerical deconvolution and by scaling with the amplitude of the calibration field we can obtain the magnetic field as a function of time $B_y(t)$ [Supplementary Fig. 2(c) bottom]. We see that the deconvolution procedure works well as the deconvolved signal resembles a single sinusoidal oscillation.

Supplementary Fig. 2(d) shows the calculated noise spectrum of the deconvoluted signal. It also shows the noise spectrum when the calibration field was off. In this case the noise at the Larmor frequency is $23\,\mathrm{fT}/\sqrt{\mathrm{Hz}}$ when 100 averages are used. The single shot magnetic field sensitivity is then $230\,\mathrm{fT}/\sqrt{\mathrm{Hz}}$.

References

1. Wijesinghe, R. S., Gielen, F. L. H. & Wikswo, J. P. A model for compound action potentials and currents in a nerve bundle III: A comparison of the conduction velocity distributions calculated from compound action currents and potentials. *Ann. Biomed. Eng.* **19,** 97–121 (1991).
2. Wikswo, J. P., Barach, J. P. & Freeman, J. A. Magnetic field of a nerve impulse: first measurements. *Science* **208,** 53–55 (1980).
3. Barry, J. F. *et al.* Optical magnetic detection of single-neuron action potentials using quantum defects in diamond. arXiv:1602.01056 (2016).
4. Budker, D. & Romalis, M. Optical magnetometry. *Nat. Phys.* **3,** 227–234 (2007).
5. Kominis, I. K., Kornack, T. W., Allred, J. C. & Romalis, M. V. A subfemtotesla multichannel atomic magnetometer. *Nature* **422,** 596–599 (2003).
6. Alem, O. *et al.* Fetal magnetocardiography measurements with an array of microfabricated optically pumped magnetometers. *Phys. Med. Biol.* **60,** 4797 (2015).
7. Sander, T. H. *et al.* Magnetoencephalography with a chip-scale atomic magnetometer. *Biomed. Opt. Express* **3,** 981–990 (2012).
8. Alem, O., Benison, A. M., Barth, D. S., Kitching, J. & Knappe, S. Magnetoencephalography of epilepsy with a microfabricated atomic magnetrode. *J. Neurosci.* **34,** 14324–14327 (2014).
9. Wasilewski, W. *et al.* Quantum noise limited and entanglement-assisted magnetometry. *Phys. Rev. Lett.* **104,** 133601 (2010).
10. Bison, G. *et al.* A room temperature 19-channel magnetic field mapping device for cardiac signals. *Appl. Phys. Lett.* **95,** 173701 (2009).
11. Vasilakis, G. *et al.* Generation of a squeezed state of an oscillator by stroboscopic back-action-evading measurement. *Nat. Phys.* **11,** 389–392 (2015).
12. Balabas, M. V. *et al.* High quality anti-relaxation coating material for alkali atom vapor cells. *Opt. Express* **18,** 5825–5830 (2010).
13. Balabas, M. V., Karaulanov, T., Ledbetter, M. P. & Budker, D. Polarized alkali-metal vapor with minute-long transverse spin-relaxation time. *Phys. Rev. Lett.* **105,** 070801 (2010).
14. Krnjevic, K. Some observations on perfused frog sciatic nerves. *J. Physiol.* **123,** 338–356 (1954).
15. Wijesinghe, R. S., Gielen, F. L. H. & Wikswo, J. P. A model for compound action potentials and currents in a nerve bundle I: The forward calculation. *Ann. Biomed. Eng.* **19,** 43–72 (1991).
16. Sheng, D., Li, S., Dural, N. & Romalis, M. V. Subfemtotesla scalar atomic magnetometry using multipass cells. *Phys. Rev. Lett.* **110,** 160802 (2013).
17. Steck, D. A. Cesium D Line Data, available online at http://steck.us/alkalidata (revision 2.1.4, 23 December 2010).
18. Hämäläinen, M., Hari, R., Ilmoniemi, R. J., Knuutila, J. & Lounasmaa, O. V. Magnetoencephalography -theory, instrumentation, and applications to noninvasive studies of the working human brain. *Rev. Mod. Phys.* **65,** 413–497 (1993).
19. Riitta Hari and Riitta Salmelin. Magnetoencephalography: From SQUIDs to neuroscience: Neuroimage 20th anniversary special edition. *NeuroImage* **61,** 386–396 (2012).
20. Xia, H., Ben-Amar Baranga, A., Hoffman, D. & Romalis, M. V. Magnetoencephalography with an atomic magnetometer. *Appl. Phys. Lett.* **89,** 211104 (2006).
21. University of Copenhagen animal ethics policy. Available at: http://emed.ku.dk/dokumenter/animal_ethics_policy.pdf. (Accessed: 26th May 2016).
22. www.aaalac.org. (Accessed: 26th May 2016).
23. Katsuki, R. *et al.* Tramadol, but not its major metabolite (mono-½O-demethyl tramadol) depresses compound action potentials in frog sciatic nerves. *Br. J. Pharmacol.* **149,** 319–327 (2006).

Acknowledgements

We would like to thank Bing Chen for help during the initial stages of the experiments, and Hannelouise Kissow for taking the electron micrograph image of the nerve. This work was supported by the ERC grant INTERFACE and by the DARPA project QUASAR. K. J. was supported by the Carlsberg Foundation. R. A. T. was supported by CNPq/Brazil.

Author Contributions

K.J., R.B., R.A.T., T.W. and H.C.S. performed the experiments. A.M.F. and S.-P.O. prepared the frog nerves. M.V.B. fabricated the vapor cell. G.V. and J.H.M. contributed with expertise on magnetometry and experimental

techniques and L.D.M. contributed with expertise on the nerves' electric and magnetic responses. K.J., G.V., E.S.P. and S.-P.O. wrote the manuscript. T.H., S.-P.O. and E.S.P supervised the research. All authors discussed the results and commented on the manuscript.

Additional Information

Supplementary information accompanies this paper at http://www.nature.com/srep

Competing financial interests: The authors declare no competing financial interests.

How to cite this article: Jensen, K. *et al.* Non-invasive detection of animal nerve impulses with an atomic magnetometer operating near quantum limited sensitivity. *Sci. Rep.* **6**, 29638; doi: 10.1038/srep29638 (2016).

This work is licensed under a Creative Commons Attribution 4.0 International License. The images or other third party material in this article are included in the article's Creative Commons license, unless indicated otherwise in the credit line; if the material is not included under the Creative Commons license, users will need to obtain permission from the license holder to reproduce the material. To view a copy of this license, visit http://creativecommons.org/licenses/by/4.0/

Supplementary Information to Non-invasive detection of animal nerve impulses with an atomic magnetometer operating near quantum limited sensitivity.

Kasper Jensen,[1] Rima Budvytyte,[1] Rodrigo A. Thomas,[1] Tian Wang,[1] Annette M. Fuchs,[2] Mikhail V. Balabas,[1,3] Georgios Vasilakis,[1] Lars D. Mosgaard,[1] Hans C. Stærkind,[1] Jörg H. Müller,[1] Thomas Heimburg,[1] Søren-Peter Olesen,[2] and Eugene S. Polzik[1]

[1]*Niels Bohr Institute, University of Copenhagen, Blegdamsvej 17, 2100 Copenhagen, Denmark*

[2]*Department of Biomedical Sciences, Faculty of Health and Medical Sciences, University of Copenhagen, Blegdamsvej 3, 2200 Copenhagen N, Denmark*

[3]*Department of Physics, St Petersburg State University, Universitetskii pr. 28, 198504 Staryi Peterhof, Russia*

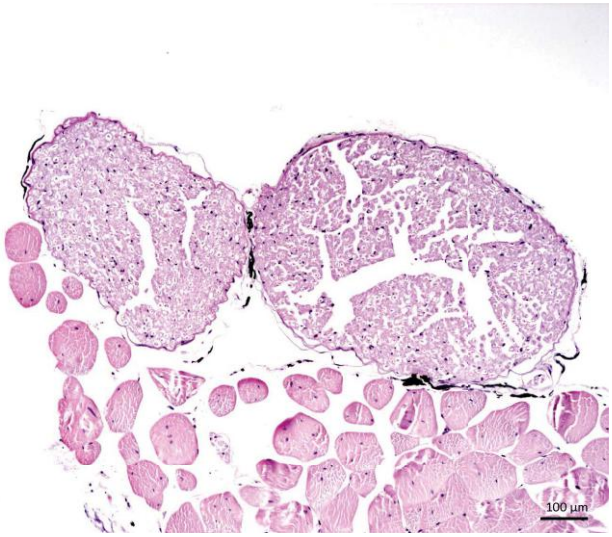

Supplementary Figure 1: Electron micrograph of a frog sciatic nerve. The micrograph shows the cross section of the frog sciatic nerve on lower femur after its first division. The two nerve bundles are surrounded by a fascia of connective tissue, and they are seen above sections of skeletal muscle. The diameters of the two nerve bundles are 0.59 and 0.44 mm and they each contain 1750 and 950 single axons with a minimal diameter of 7 μm. The individual myelinated nerve fibres have an average diameter of 16 μm.

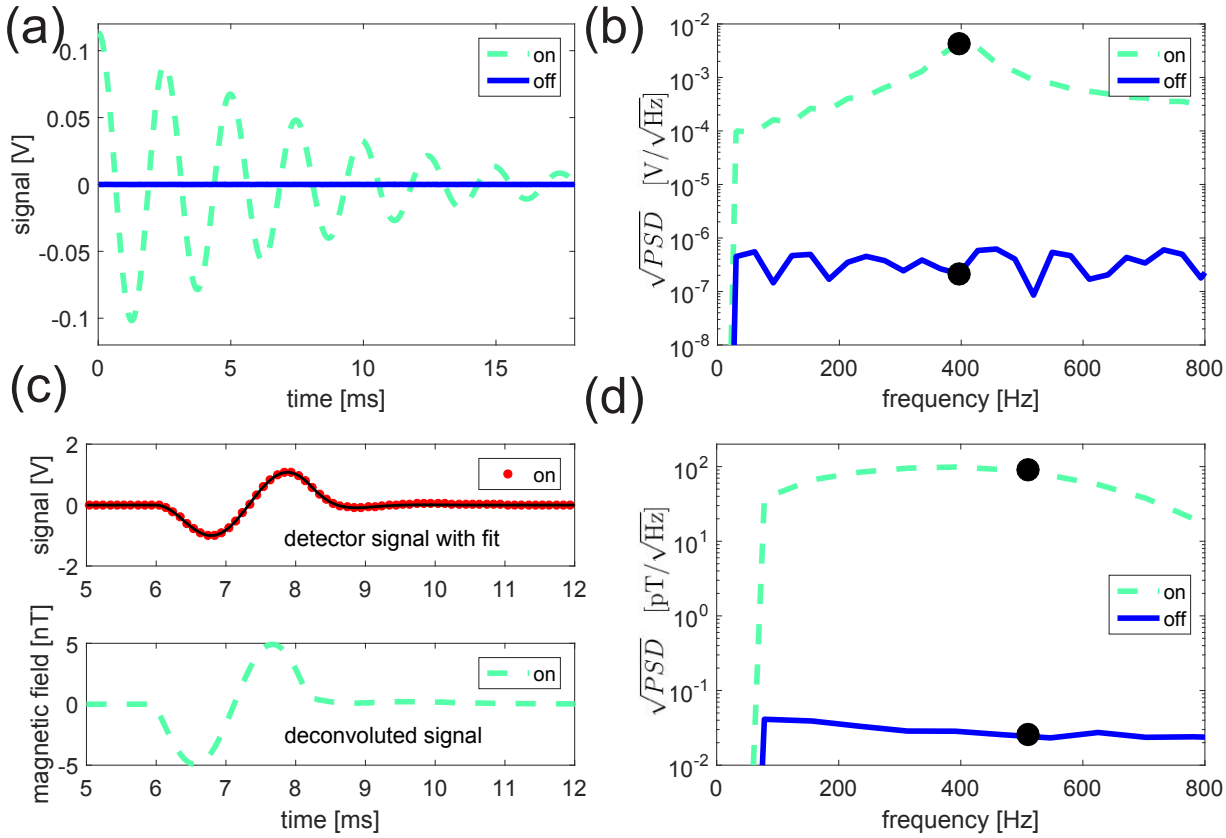

Supplementary Figure 2: Measurements with and without the calibration field. (a,b) Pulsed mode: $\Omega = 400$ Hz, $T_2^{\text{dark}} = 27$ ms. The PSD is calculated using the first 18 ms of the recorded signal. (c,d) Continuous mode: $\Omega = 510$ Hz, $T_2 = 0.37$ ms. The PSD is calculated using 7 ms of the recorded signal. The Larmor frequencies are marked in (b) and (d) with a dot.

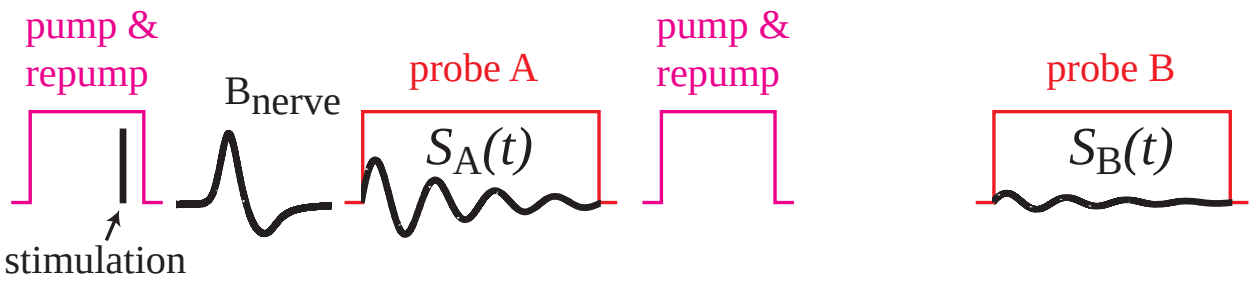

Supplementary Figure 3: Pulse sequence for measuring the nerve impulse.

MAGNETOMETER PRINCIPLE

The total spin of the atomic ensemble is defined as $\mathbf{J} = (J_x, J_y, J_z)$. Here $\mathbf{J}$ is a quantum operator, and the components have the commutation relation $[J_y, J_z] = iJ_x$. $\mathbf{J}$ is here defined as being unitless and equals the total angular momentum divided by the reduced Planck constant $\hbar$. The equations of motion for the spin vector can be derived using the Heisenberg equation of motion

$$\dot{\mathbf{J}}(t) = \frac{1}{i\hbar}\left[\mathbf{J}(t), \mathcal{H}_B\right]. \tag{1}$$

The dot denotes the time-derivative and the bracket denotes the commutator. The Hamiltonian describing the coupling between the spin and the magnetic field is

$$\mathcal{H}_B = \hbar\gamma \mathbf{B}\cdot\mathbf{J}, \tag{2}$$

where γ is the gyromagnetic ratio which for the cesium atom in the $F = 4$ ground state equals 2.2×10^{10} rad/(sec·Tesla). In vector form the equation of motion reads

$$\dot{\mathbf{J}}(t) = \gamma \mathbf{J}\times\mathbf{B}. \tag{3}$$

In the experiment, the atoms are spin-polarized in the x-direction and located in a static magnetic field B_x pointing in the x-direction. In the presence of a small time-dependent magnetic field $B_y(t)$ or $B_z(t)$ pointing in the y- or z-direction, the spin vector will acquire a transverse component $\mathbf{J}_\perp = (J_y, J_z) = |\mathbf{J}_\perp|(\cos\theta, \sin\theta)$. We will assume that J_x is large compared to J_y and J_z, and that J_x is independent of time. We now introduce spin operators J'_y and J'_z rotating at the Larmor frequency $\Omega = \gamma B_x$:

$$\begin{pmatrix} J'_y \\ J'_z \end{pmatrix} = \begin{pmatrix} \cos\Omega t & \sin\Omega t \\ -\sin\Omega t & \cos\Omega t \end{pmatrix} \begin{pmatrix} J_y \\ J_z \end{pmatrix}. \tag{4}$$

In the rotating frame, the equations of motion read

$$\dot{J}'_y(t) = \gamma J_x\left[\cos(\Omega t)\, B_z(t) - \sin(\Omega t)\, B_y(t)\right] - \Gamma J'_y(t) + \sqrt{2\Gamma}F_y(t), \tag{5}$$

$$\dot{J}'_z(t) = -\gamma J_x\left[\sin(\Omega t)\, B_z(t) + \cos(\Omega t)\, B_y(t)\right] - \Gamma J'_z(t) + \sqrt{2\Gamma}F_z(t). \tag{6}$$

The transverse spin component will eventually decay, and we have therefore added decay terms in the above equations. The decay rate is denoted by Γ and the associated decay time is $T_2 = 1/\Gamma$. We also added Langevin noise operators $F_y(t)$ and $F_z(t)$ with zero mean values and correlation functions $\langle F_y(t)F_y(t')\rangle = \mathrm{var}(F_y)\,\delta(t-t')$, $\langle F_z(t)F_z(t')\rangle = \mathrm{var}(F_z)\,\delta(t-t')$ and $\langle F_y(t)F_z(t')\rangle = 0$, where $\mathrm{var}(F_y) = \mathrm{var}(F_z) = |J_x|/2$ and $\delta(t-t')$ is the Dirac delta-function. These equations can be integrated and the solutions are

$$J'_y(t) = e^{-\Gamma t}J'_y(0) + \sqrt{2\Gamma}\int_{t'=0}^{t} e^{-\Gamma(t-t')}F_y(t')dt' + \gamma J_x\int_{t'=0}^{t} e^{-\Gamma(t-t')}\left[\cos(\Omega t')\, B_z(t') - \sin(\Omega t')\, B_y(t')\right]dt', \tag{7}$$

$$J'_z(t) = e^{-\Gamma t}J'_z(0) + \sqrt{2\Gamma}\int_{t'=0}^{t} e^{-\Gamma(t-t')}F_z(t')dt - \gamma J_x\int_{t'=0}^{t} e^{-\Gamma(t-t')}\left[\sin(\Omega t')\, B_z(t') + \cos(\Omega t')\, B_y(t')\right]dt'. \tag{8}$$

From these equations we can calculate the mean values and noise proporties of the transverse spin components as a function of time.

Free precession

Assume that the transverse spin has some mean value at $t = 0$ and that it is then left free to precess. At a later time t the transverse spin component in the rotating frame is

$$\langle \mathbf{J}'_\perp(t)\rangle = \langle \mathbf{J}_\perp(0)\rangle\, e^{-\Gamma t}. \tag{9}$$

We see that the mean value decays in time. In the lab frame the transverse spin will perform a damped oscillation.

Atomic response to a pulse of magnetic field

Consider the case where a magnetic field $B_y(t)$ is applied for a duration τ. We assume that $\tau \ll T_2$ such that any decay of the spin components can be neglegted. If initially the transverse spin component is zero $\langle \mathbf{J}_\perp(0)\rangle = 0$, we find

$$\langle \mathbf{J}'_\perp(\tau)\rangle = \gamma J_x \left(\mathrm{Im}[B_y(\Omega)], -\mathrm{Re}[B_y(\Omega)]\right) \tag{10}$$

and

$$|\langle \mathbf{J}'_\perp(\tau)\rangle| = \gamma J_x \left|B_y(\Omega)\right|. \tag{11}$$

Here we have defined the Fourier component of the magnetic field at the Larmor frequency as

$$B(\Omega) = \int_{t'=0}^{\tau} B(t') e^{-i\Omega t'}\, dt. \tag{12}$$

Similarly, if the magnetic field is applied along the z-direction instead, the transverse spin component will be

$$|\langle \mathbf{J}'_\perp(\tau)\rangle| = \gamma J_x \left|B_z(\Omega)\right|. \tag{13}$$

We see that magnetic fields in y- and z-directions have similar effects on the spins: the fields create transverse spin components with lengths proportional to the Fourier components of the magnetic fields at the Larmor frequency.

For the specific case of a sinusoidal magnetic field $B_y(t) = B_0 \sin(\Omega t)$ applied for one period of oscillation $\tau = 2\pi/\Omega$, we find $|B_y(\Omega)| = \pi B_0/\Omega$ and $|\langle \mathbf{J}'_\perp(\tau)\rangle| = \gamma J_x (\pi B_0/\Omega)$.

Projection noise limited detection

The measurement of the transverse spin component is fundamentally limited by the spin-projection noise originating from the Heisenberg uncertainty principle. This uncertainty is $\Delta\left|J_\perp\right| = \sqrt{J_x/2}$. By equating the created mean value given by Eq. (13) to the projection noise we find the uncertainty on the magnetic field Fourier component due to the projection noise:

$$\Delta\left|B_{\mathrm{PN}}(\Omega)\right| = 1/\left(\gamma\sqrt{2J_x}\right). \tag{14}$$

We can also calculate the uncertainty on the amplitude of an oscillating magnetic field due to the projection noise. For a sinusoidal magnetic field with total duration τ equal to an integral multiple of the Larmor period, the amplitude B_0 is related to the Fourier component by $|B(\Omega)| = B_0\tau/2$. From this and Eq. (14) we find the projection noise limited uncertainty on the amplitude:

$$\Delta B_{\mathrm{PN}} = 1/\left(\gamma\sqrt{J_x/2}\tau\right), \tag{15}$$

which is often called the minimal detectable field. The magnetic field sensitivity can be found by multiplying ΔB_{PN} with the square-root of the total measurement time $\sqrt{T_{\mathrm{tot}}}$ and setting $T_{\mathrm{tot}} = \tau = T_2$:

$$\Delta B_{\mathrm{PN}}\sqrt{T_{\mathrm{tot}}} \sim 1/\left(\gamma\sqrt{T_2 J_x/2}\right). \tag{16}$$

The Standard Quantum Limit

Besides the projection noise, the magnetic field measurement will be limited by the quantum shot noise of the probing light, and the back-action noise imposed by the probe on the atomic spins. The total uncertainty is

$$\Delta B_{\mathrm{tot}} = \sqrt{(\Delta B_{\mathrm{PN}})^2 + (\Delta B_{\mathrm{SN}})^2 + (\Delta B_{\mathrm{BAN}})^2}, \tag{17}$$

which can be written as[1,2]

$$\Delta B_{\mathrm{tot}} = \Delta B_{\mathrm{PN}} \cdot \sqrt{1 + 1/\kappa^2 + \kappa^2/3}, \tag{18}$$

where $\kappa = \Delta B_{\mathrm{PN}}/\Delta B_{\mathrm{SN}}$ is a dimensionless light-atom coupling constant. For small coupling strengths, the measurement noise will be dominated by the shot noise, and for large coupling strengths, the measurement noise will be dominated by the back-action noise. By minimizing the uncertainty given by Eq. (18), we find the optimal coupling strength $\kappa \approx 1.3$ and the standard quantum limit on the magnetic field measurement

$$\Delta B_{\mathrm{SQL}} \approx 1.5 \cdot \Delta B_{\mathrm{PN}}, \tag{19}$$

which is ≈ 1.5 times larger than the uncertainty due to the projection noise.

Measuring the atomic signal

The atomic spin can be measured optically. Assume that a linearly polarized pulse of light is propagating in the z-direction through the atomic ensemble. The polarization of the light will be rotated by an angle proportional to J_z due to the Faraday paramagnetic effect. The polarization of the light is described using Stokes operators $S_x(t)$, $S_y(t)$, and $S_z(t)$ which have the unit of 1/time. Here $S_x(t) = [\Phi_x(t) - \Phi_y(t)]/2$ equals one half the difference in photon flux of x- and y-polarized light. $S_y(t)$ refer to the differences of $+45°$ and $-45°$ polarized light, and $S_z(t)$ to the differences of right hand and left hand circular polarized light. Assuming that the input light before the atomic ensemble is either

x or y-polarized (such that $S_x(t)$ is a large quantity) and that the rotation angle is small, the output light after the atomic ensemble can be described by the equation

$$\begin{aligned} S_y^{\text{out}}(t) &= S_y^{\text{in}}(t) + aS_x(t)J_z(t) \\ &= S_y^{\text{in}}(t) + aS_x(t)\left[\sin(\Omega t)\, J_y'(t) + \cos(\Omega t)\, J_z'(t)\right]. \end{aligned} \tag{20}$$

The parameter a describes the coupling strength between the atoms and the light[1]. The Stokes operator $S_y^{\text{out}}(t)$ can be measured with polarization homodyning. There are several ways that one can extract information about the transverse spin components and therefore about the magnetic field from the measured signal. One can for instance measure the mean value $\left\langle S_y^{\text{out}}\right\rangle$ or the power spectral density of the signal. The power spectral density (PSD) for a function $x(t)$ is defined as

$$S_{xx}(\omega) = \frac{1}{T}\left\langle \left| \int_{t=0}^{T} x(t) e^{-i\omega t} dt \right|^2 \right\rangle = \frac{1}{T}\int_{t=0}^{T}\int_{t=0}^{T} \langle x(t)x(t')\rangle\, e^{-i\omega\left(t-t'\right)} dt dt'. \tag{21}$$

We will show below that the PSD of $\left\langle S_y^{\text{out}}(t)\right\rangle$ is proportional to the amplitude squared of the applied magnetic field.

Detection of a pulse of magnetic field

Assume that a pulse of magnetic field $B_y(t)$ of duration τ is applied from $t = -\tau$ to $t = 0$. After the pulse, the spins have acquired a non-zero transverse spin component $\langle \mathbf{J}_\perp'(0)\rangle \propto |B_y(\Omega)|$ as given by Eq. (11). At $t = 0$ the spin will continue to precess until it decays as described by Eq. (9). This spin vector can be measured using a pulse of light with duration T and starting at the time when the magnetic field pulse ends. The mean value of the measured signal is

$$\left\langle S_y^{\text{out}}(t)\right\rangle = aS_x(t)\left[\sin(\Omega t)\left\langle J_y'(0)\right\rangle + \cos(\Omega t)\left\langle J_z'(0)\right\rangle\right] e^{-\Gamma t} = aS_x(t)\left|\langle \mathbf{J}_\perp'(0)\rangle\right| \sin(\Omega t + \theta)\, e^{-\Gamma t}, \tag{22}$$

where θ is the polar angle of $\langle \mathbf{J}_\perp'(0)\rangle$. The amplitude of the transverse spin vector can be extracted from the measurement by, for instance, a fit of the experimental data to Eq. (22). Alternatively, one can calculate the PSD of the signal. For $x(t) = A\sin(\Omega t + \theta)\, e^{-\Gamma t}$ we calculate that the peak value of the PSD is

$$S_{xx}(\Omega) = |A|^2 \left[\frac{\left(1 - e^{-\Gamma T}\right)^2}{4\Gamma^2} + \epsilon(\theta, \Gamma, \Omega, T)\right], \tag{23}$$

where the second term $\epsilon(\theta, \Gamma, \Omega, T)$ is much smaller than the first term for our experimental parameters. We see that

$$S_{xx}(\Omega) \propto \left|\langle \mathbf{J}_\perp'(0)\rangle\right|^2 \propto \left|B_y(\Omega)\right|^2, \tag{24}$$

and that the Fourier component of the magnetic field at the Larmor frequency can be extracted from the peak value of the PSD.

Continuous recording of the magnetic field

We will now discuss how one can measure the magnetic field as a function of time. Assume that a magnetic field $B_y(t)$ is applied and that light is continuously monitoring the atomic spin. If $\langle \mathbf{J}_\perp(0)\rangle = 0$, then at a later time

$$\langle J_z(t)\rangle = -\gamma J_x \int_{t'=0}^{t} e^{-\Gamma(t-t')} \cos\left[\Omega\left(t-t'\right)\right] B_y(t')dt'. \tag{25}$$

The mean value of the measured signal will be

$$\left\langle S_y^{\text{out}}(t)\right\rangle = aS_x(t)\left\langle J_z(t)\right\rangle. \tag{26}$$

From this we see that the measured signal $\left\langle S_y^{\text{out}}(t)\right\rangle$ is proportional to the convolution of $B_y(t)$ with the function $\left[-\cos\left(\Omega t\right)e^{-\Gamma t}\right]$. Similarly, if the transverse magnetic field is pointing in the z-direction, the signal is proportional to the convolution of the magnetic field $B_z(t)$ with the function $\left[\sin\left(\Omega t\right)e^{-\Gamma t}\right]$. The magnetic field as a function of time can be extracted from the measured data using numerical deconvolution.

EXPERIMENTAL PROCEDURE

Three lasers denoted pump, repump and probe are used in the experiment. The pump laser is on resonance with the cesium $F = 4 \rightarrow F' = 4$ D1 transition and has the wavelength 895 nm. The repump laser is on resonance with the cesium $F = 3 \rightarrow F' = 2, 3, 4$ D2 transitions (all are within the Doppler linewidth) and has the wavelength 852 nm. These two lasers are used for optical pumping of the cesium atoms into the $F = 4, m = 4$ hyperfine sublevel and are thereby creating a high spin-polarization of the cesium vapor. The probe laser is 1.6 GHz higher in frequency than the cesium $F = 4 \rightarrow F' = 5$ D2 transition and has the wavelength 852 nm. The 1.6 GHz detuning is much larger than both the natural linewidth (5 MHz FWHM) and the Doppler linewidth (380 MHz FWHM) such that negligible absorption occurs.

The pulse sequence in Supplementary Fig. 3 is used for detection of the magnetic field from the nerve impulse B_{nerve}. The atoms are first optically pumped using pump and repump light, then the magnetic field is present, and finally the atoms are measured using probe pulse A. The optically detected signal $S_A(t)$ will be a free induction decay as seen in Supplementary Fig. 3. Due to misalignment of the pump and repump laser beams with respect to the bias field B_x (see Fig. 1 in the main text), one may observe a free induction decay $S_B(t)$ [see probe pulse B in Supplementary Fig. 3] even if there is no magnetic field. The pump/repump and probe pulses are therefore repeated and the signals from probe pulses A and B are subtracted giving the magnetometer signal $S(t) = S_A(t) - S_B(t)$. The amplitude of this magnetometer signal will be proportional to the Fourier component of the magnetic field at the Larmor frequency $|B(\Omega)|$.

CONDUCTION VELOCITY

The nerve conduction velocity can be calculated by dividing the distance from the stimulation electrodes to the recording site [34(5) mm for optical recording and 53(10) mm for electrical recording] by the time interval between the stimulus artifact and the zero-crossing of the observed nerve signal (see Fig. 4(c) in the main text). The electrical recording measures the potential difference ΔV between two external electrodes separated by 5 mm. As the extent of the action potential Φ is much larger than electrode spacing, the electrical signal is proportional to the time-derivative of the action potential $\Delta V \propto \partial\Phi/\partial t$. The zero-crossing of the electrical signal therefore corresponds to when the peak of the action potential passes the electrodes. Also, when the peak of the action potential passes the magnetometer, the magnetic field is zero, as the magnetic field $B(t) \propto \partial\Phi/\partial t$ according to a simple model for the nerve[3]. The earlier arrival of the nerve impulse for optical recording compared to electrical recording [1.0(2) ms compared to 2.4(2) ms] is consistent with the magnetometer being positioned in between the stimulating and recording electrodes. From the measurements shown in Fig. 4(c) we calculate the conduction velocity of 34(8) m/s and 22(5) m/s for optical and electrical recording. We note that stating a single number for the conduction velocity is not entirely correct as the frog sciatic nerve contains thousands of axons of varying diameter (see Fig. S1). For a single myelinated axon, the conduction velocity is proportional to the axon's diameter, which leads to a distribution of velocities within the range 10-40 m/s for axons in the frog sciatic nerve[4].

ESTIMATE OF THE AXIAL IONIC CURRENT

The detected magnetic field is created by axial ionic currents inside the nerve bundle. There is a forward current inside the axons and a return current outside the axons. The magnetic fields from the forward and return currents can cancel each other, the exact degree of cancellation depends on the anatomy of the nerve, and the geometry of the experiment, such as the size of the magnetic field sensor and the distance from the nerve to the sensor.

We can estimate the axial current in the nerve from our magnetic field measurements. We use a simple model, where we assume that the ionic current is concentrated at the center of the nerve, and that the nerve produces a magnetic field similar to that of an infinitely long conducting wire. The magnetic field from an infinitely long wire is $|B| = \mu_0 I/(2\pi r)$, where μ_0 is the magnetic permeability, I is the current, and r is the radial distance from the wire. Using $r = 1.9$ mm for the distance from the center of the nerve to the center of the vapor cell, we calculate that a current of 0.23 μA will produce a magnetic field of 24 pT.

Our estimate of 0.23 μA is smaller than the 0.4 μA which was estimated in previous work on the frog sciatic nerve[5]. This is expected as in that work, the nerve was put in a large container with saline solution and the magnetic field was measured by a coil with the nerve inside it, such that a large part of the return current could flow without being detected.

[1] K. Jensen. Quantum information, entanglement and magnetometry with macroscopic gas samples and non-classical light. PhD thesis, University of Copenhagen (2011).

[2] Vasilakis, G. et al. Generation of a squeezed state of an oscillator by stroboscopic back-action-evading measurement. *Nat. Phys.*, **11,** 389–392 (2015).

[3] Barry, J. F. et al. Optical magnetic detection of single-neuron action potentials using quantum defects in diamond. arXiv:1602.01056 (2016).

[4] Wijesinghe, R. S., Gielen, F. L. H. & Wikswo, J. P. A model for compound action potentials and currents in a nerve bundle III: A comparison of the conduction velocity distributions calculated from compound action currents and potentials. *Ann. Biomed. Eng.*, **19,** 97–121 (1991).

[5] Wijesinghe, R. S., Gielen, F. L. H., & Wikswo, J. P. A model for compound action potentials and currents in a nerve bundle I: The forward calculation. *Ann. Biomed. Eng.*, **19,** 43–72 (1991).